THE DYNAMICS OF RED BLOOD CELL UNDER THE EFFECT OF SHAPE MEMORY

A Dissertation

Presented to

the Faculty of the Department of Mathematics

University of Houston

In Partial Fulfillment

of the Requirements for the Degree

Doctor of Philosophy

By

Xiting Niu

December 2014

THE DYNAMICS OF RED BLOOD CELL

UNDER THE EFFECT OF SHAPE MEMORY

Xiting Niu

APPROVED:

Dr. Tsorng-Whay Pan, Co-Chairman

Dr. Roland Glowinski, Co-Chairman

Dr. Jiwen He

Dr. Dong Liu
Department of Mechanical Engineering
University of Houston

Dean, College of Natural Sciences and Mathematics

Acknowledgements

First and foremost, I would like to express the deepest appreciation to my advisors, Dr. Tsorng-Whay Pan and Dr. Roland Glowinski for their encouragement, guidance, and patience throughout this work. Without their persistent help this dissertation would not have been possible. Many special thanks to Dr. Pan, who made so many effort to lead me in my field of interest, listen to my ideas, and always give the best advice.

I want to thank my fellow group members Shang-Huan Chiu, Lingling Shi, Yao Yu, and Shihai Zhao, for sharing their precious ideas to improve my research, and their incredible collaborative work.

I would like to thank my committee members, Dr. Jiwen He and Dr. Dong Liu for their time to read my dissertation, and the valuable comments and suggestions.

Special thanks to Dr. Shanyu Ji, for all his kindness and nice suggestions for both Ph.D studies and daily life. I thank him for his advices on course selection and choosing my research area, also for sharing his experience as a international student in the US.

Finally, I dedicate this dissertation to my family and friends, without whom I would not have been finish this work.

THE DYNAMICS OF RED BLOOD CELL UNDER THE EFFECT OF SHAPE MEMORY

An Abstract of a Dissertation

Presented to

the Faculty of the Department of Mathematics

University of Houston

In Partial Fulfillment

of the Requirements for the Degree

Doctor of Philosophy

By

Xiting Niu

December 2014

Abstract

An one–dimensional elastic spring model is proposed to study the effect of shape memory on the motion of a red blood cell in two-dimensional flows. In simple shear flow, the shape memory effect also plays a role for having two well known motions: tumbling and swinging. The intermittent behavior of the cell with a nonuniform natural state has been obtained in a narrow range of the capillary number and has been studied thoroughly. The critical value of the swelling ratio for having the intermittent behavior has been estimated. In plane Poiseuille flow, the cell with the shape memory has an equilibrium shape as a slipper or parachute depending on capillary number. To ensure the tank-treading motion while in slippery shape, the upper bound of the shape memory coefficient has been suggested. Then our 1D model has been extended to 2D, which has been validated by several benchmarking tests. In three-dimensional shear flow, the critical shear rate for the cell motion transition from tumbling to swinging is consistent with the experiments. And in tube Poiseuille flow with rectangular cross section, the cell without shape memory always has a symmetric equilibrium shape while the one with shape memory can obtain a slippery shape at low flow rate. When the cell with shape memory passes through a very narrow channel, it becomes a cup-shape first and then recovers its biconcave shape with a rotation of its orientation. Such rotation is due to the tank–treading motion of the membrane caused by the shape memory.

Contents

List of Figures

List of Tables

Chapter 1

Introduction

1.1 Motivation

An adult human has around $2 - 3 \times 10^{13}$ red blood cells (erythrocytes), which make up about 44% of the volume of whole blood. This volume percentage of red blood cells to total volume is called hematocrit (HCT), also known as packed cell volume (PCV) or erythrocyte volume fraction (EVF). Other blood cells, like white blood cells (leukocytes) and platelets (thrombocytes), only take less than 1% of blood volume. The remaining 55% volume are composed of blood plasma, it is mostly water (up to 95% by volume), and contains dissolved proteins, glucose, clotting factors, electrolytes, hormones, and carbon dioxide. The human blood, as shown in Figure 1.1, is a suspension of blood cells within the blood plasma. It is in charge of delivering necessary substances such as nutrients and oxygen to cells, and transporting metabolic waste away from them through blood vessels. Among all these functions, the red blood cell plays an essential role in carrying oxygen from the lungs to the body tissues and carbon dioxide from tissues to lungs.

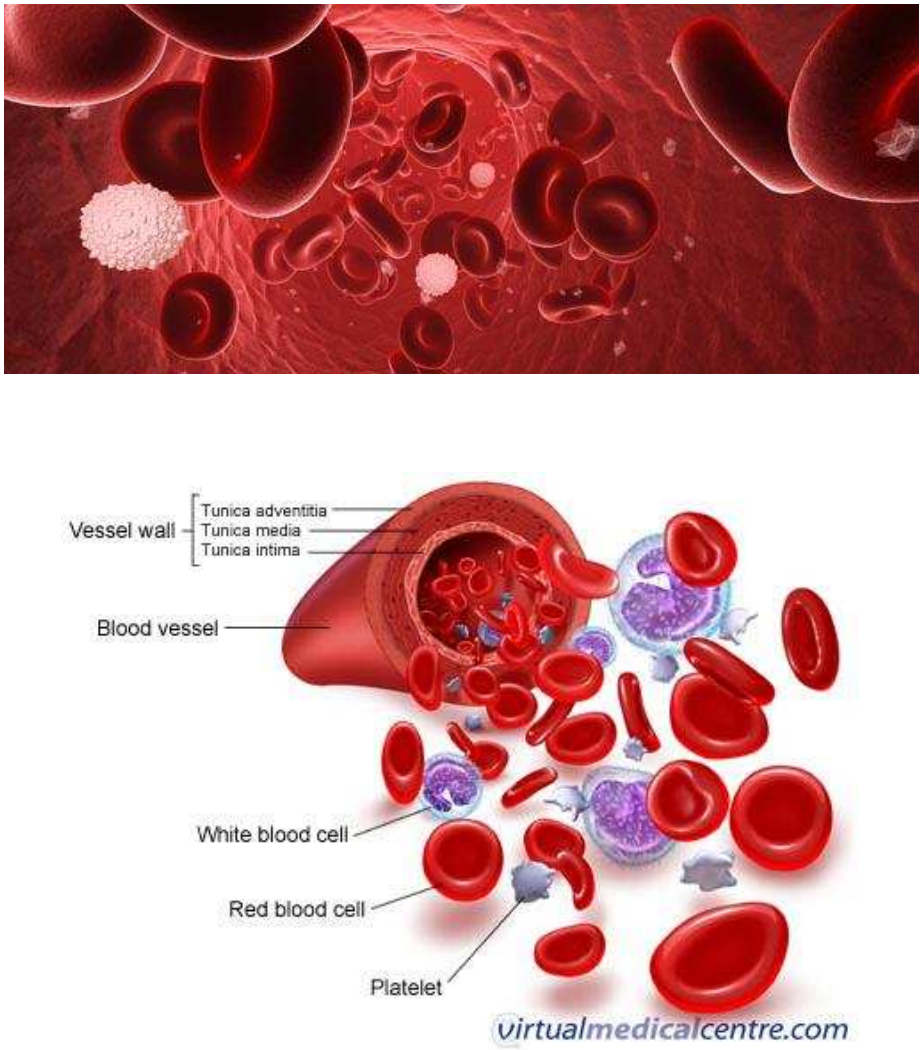

Figure 1.1: Diagrams of human blood flowing through blood vessels (top) and classification of three categories of blood cells (bottom) [39].

A typical red blood cell has a biconcave disk shape, with average diameter $7.82\mu m$, thickness $2.58\mu m$, surface area $135\mu m^2$ and volume $94\mu m^3$[19]. Because of the excess area, a healthy red blood cell is highly deformable. The cell membrane consists of two layers: 1), the phospholipid bilayer with glycocalyx attached on the surface and 2), the cytoskeleton structure, which is a network of proteins fastened to the bilayer. The bilayer provides the cell with bending elasticity, and the skeleton structure provides with shear elasticity. In addition, the thin bilayer has a strong resistance against surface area change.

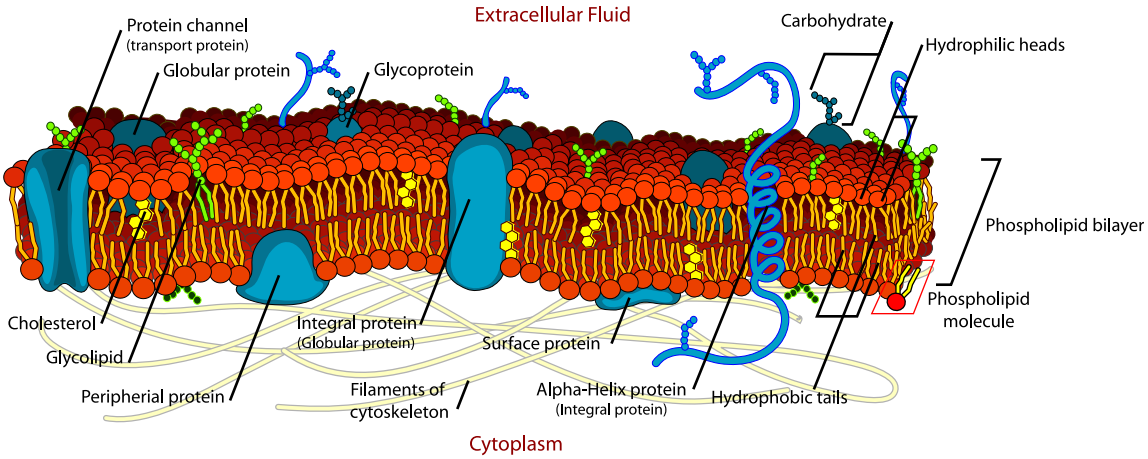

Figure 1.2: Structure diagram of red blood cell membrane [26], it is mainly composed of the phospholipid bilayer and the cytoskeleton structure.

The biconcave rest shape of a red blood cell can be deformed when external forces are acting on the cell, but will be recovered when the cell is released. Moreover, it is reported to have a shape memory effect [22] in the sense that, not only the biconcave shape is recovered, but also the whole configuration of the membrane. To be more precise, the rim is always formed by the same part of the membrane, and dimple always dimple in stress free state. Due to the shape–memory effect, the red cell may exhibit three types of motion

in shear flow: With low shear rate (or high viscosity ratio between the inner and outer fluid), the cell behaves more like a rigid body, and undergoes an unsteady tumbling motion (TB, also referred to as flipping) where the cell major axis rotates about mass center; with high shear rate (or low viscosity ratio), cell becomes more fluid like, it may take a steady tank-treading motion (TT), where cell have a equilibrium shape and inclination angle, with cell membrane rotates around the inner cytoplasm like the motion of tank wheel bands; in moderate shear rate (or moderate viscosity ratio), cell performs a swinging motion (SW) which a transition between the previous two, where the inclination angle undergoes oscillation about the flow direction and the membrane tank-treads. The steady tank-treading motion can be viewed as an extreme case of the swinging that the oscillation of inclination angle is so small that can be neglected. In Poiseuille flow, cell may perform tank-treading motion with an asymmetric slippery shape with moderate Reynolds number, and show an equilibrium symmetric parachute shape if Reynolds number is high enough [54]. A suspension of red blood cells in small capillary may have some rouleaux form at low flow speed [35, 59] and are destructed when increase the shear rate. If initially suspended randomly, cells are know to migrate to the center of the capillary [55] and a cell-free layer will be formed, the size of cell-free layer depends on the capillary size and hematocrit, etc.

The interaction between the red blood cell and the external fluid is yet far from fully understood, even in simple shear flow, recent studies suggests in addition to the typical aforementioned three motions, cell may also have in-plane intermittency [57], and out-plane rolling, or spinning motions [17]. On the other hand, the understanding of full dynamics of cell motion in flow is very important, especially in cell separation and in diagnosing those diseases where cell rheology has been changed, such as sickle cell disease, thalassemia, malaria, etc. Therefore, the red blood cell dynamics is attracting more and more interest of researchers through experimental, theoretical, and numerical approaches.

Simplified systems of RBC have been often adopted as an alternative in most studies based on the fact that they are easily fabricated in the laboratory, with their size, shape, and mechanical properties may vary [38]. They all represent several aspects of RBC properties but not all. For example, vesicles are made of a pure phospholipid bilayer, which ensures the membrane area to be inextensible, but the absence of skeleton structure takes away the shear elasticity; while capsules are quasi-spherical shells made of polymers, which is usually extensible, but they have shear elasticity. In some studies inextensible capsules are also been used to model the RBC behaviors in various flows[51].

Starting with Keller and Skalak [30], several models and numerical methods have been developed to study the reological properties of vesicles, capsules, and red blood cells. The continuum models are usually following the Skalak, Mooney-Rivlin and neo-Hookean laws, with or without bending resistance [30, 18, 51, 3, 57]. On the other hand, spring network models are also very popular in numerical simulations [60, 20, 62]. Recently, some multi-scale modeling [20, 46] has been introduced to gather as much cell mechanical properties as possible, and are expected to gain more delicate results with fairly increasing amount of computational load. There are also various flow solvers which can treat the flow-structure interactions, for example, the Immersed boundary methods based on finite element methods [32, 53], lattice-Boltzmann methods [58, 29], finite difference methods [16], particle methods such as Dissipative particle dynamics [20] and Smoothed Particle Hydrodynamics [60], the Boundary integral equation methods [64, 52], etc.

Keller and Skalak (KS) [30] theoretically analyzed the motion of a membrane with a fixed ellipsoidal shape in simple shear flow. They found that the transition from tank treading mode to tumbling mode depends on the viscosity ratio of the internal fluid and external fluid and is independent of shear rate. The viscosity–ratio–dependent transition

has also been studied and explained in [27, 28, 37, 4]. Noguchi and Gompper [40, 41, 42] have studied the dynamics of vesicles in simple shear flow using mesoscale simulations of dynamically triangulated surfaces. Vesicles are found to transit from steady tank–treading to unsteady tumbling motion, or swinging with increasing membrane viscosity. In [42], they have developed a model based on the classical framework of Keller and Skalak [30] for the membrane to theoretically explain the vesicle motion. Using their model, they predicted the swinging motion and studied the dependency of transition between tumbling and swinging on the shear rate, the viscosity ratio of the membrane and the internal fluid, and the reduced volume [42]. However, they did not mention the shape memory property of red blood cells discovered by Fischer [22]. The experimental evidence of the existence of swinging motion is obtained by Abkarian *et al.* [1]. They also observed the intermediate motions during the transition from swinging to tumbling (respectively, tumbling to swinging) by reducing (respectively, increasing) the flow shear rate. A simplified model with a fixed elliptical shape for cell membrane is studied to theoretically support their observations. In [57], Skotheim and Secomb introduced an elastic energy in terms of the phase angle of the tank–treading rotation in addition to the KS theory. They observed tumbling, tank–treading with swinging, and the intermittent behavior between these two states and analyzed the influence of the viscosity ratio, membrane elasticity, shape, and the shear rate on the motion of a capsule of either prolate or oblate shape. The both simplified models considered in [57, 1] take into account the membrane shear elasticity for the effect of the shape memory. Tsubota *et al.* [60] used an elastic spring model fully coupled with fluid flow to study cell motion dependency on the natural state of membrane in two–dimensional shear flow. The so–called natural state, defined as the reference shape of membrane in zero–stress state in [60], automatically determines the shape memory property of the cell. When being at uniform natural state (i.e., all reference angles are set to be the same), the cell appears

to tank–tread with an inclination angle unchanged and independent of the preset value of reference angles. But when a biconcave resting shape is assumed as the natural state (called non–uniform state), the cell is observed to perform tumbling, swinging, and tank–treading motions. In [60], Tsubota *et al.* also predicted the intermittency between swinging and tumbling would occur in very narrow range of parameter space, but they did not obtain such intermittent behavior because, we believe, the swelling ratio of their cell is not small enough. In [66], Vlahovska *et al.* used perturbation approach to study the motion of an almost–spherical capsule in shear flow at the Stokes regime. Their reduced models are more general and have no restriction of the fixed shape on the capsule when comparing with the one in [57]. Without the shape–memory effect, Vlahovska *et al.* obtained the intermittency when having deformation only in the shear plane and that the intermittent behavior disappears in Stokes flow for an almost spherical capsule (not a capsule of biconcave shape) that can deform in the vorticity direction. They concluded that the intermittency is an artifact of the shape preservation. In [62], the transition between tumbling and tank–treading motions has been considered while studying the model of the RBC membrane fully coupled with the Stokes flow. Tsubota *et al.* obtained no intermittency dynamics around the transition between tumbling and tank–treading motions for the cases of the viscosity ratio, λ, of the internal RBC fluid and the suspending fluid between 0.1 and 0.3, which is quite low when comparing with the values used in [57, 66]. In [20], Fedosov *et al.* used a two–dimensional spring network with the shape memory effect in the bending energy term to model red blood cell membrane. They obtained the intermittent behavior in shear flow for the cases of the viscosity ratio λ greater than or equal to 1, but did not study further about the intermittent behavior.

In this dissertation, we first propose a two-dimensional modified model for red blood cell membrane based on the one developed by Tsubota *et al.* [60], and analyze the cell

motion in simple shear flow via direct numerical simulation, especially the intermittent behavior. In [57], Skotheim and Secomb restricted the capsule or cell to stay in the shear plane with the fixed shape and obtained the intermittent behavior by studying the in–plane inclination angle and phase angle with the shape memory energy defined by the phase angle, which is actually a two–dimensional model. We want to relax the restriction of the non–deformability (i.e., the fixed shape) and consider a full model for the fluid and cell interaction in two–dimensional shear flow, which is closely related to the study of the inclination angle and phase angle in the shear plane as in [57]. Furthermore, we have taken into account the effect of shape memory similar to the one used in [57] with a parameter α, which is the weight of shape memory in total bending energy. Then we have studied the dependency of the cell motion on the capillary number $C_a = \mu\dot{\gamma}R_0^3/B$, where μ, $\dot{\gamma}$, R_0, and B stand for the fluid viscosity, the shear rate of fluid flow based on the gradient of the velocity at the wall, the effective radius of the cell and the bending modulus, respectively. Also, we have tested the effect of coefficient α and found that as this parameter decreases, the critical capillary number at transition from tumbling to swinging decreases almost linearly, and the range for having the intermittent state becomes narrow. To explain the linearly of the critical capillary numbers with respect to α, we have defined the weighted–bending–capillary number Ca_B^α, which is similar to the bending capillary number in [60], but taking the effect of shape memory α into account and found that transition occurs around the same range of Ca_B^α. Also the swelling ratio of the cell does have its effect to the intermittent behavior as indicated in the figures presented in [57]. We have obtained that for the cell of swelling ratio greater than 0.6, it is almost impossible to capture the intermittent behavior with viscosity ratio equal to 1, since the range of the capillary number for such behavior is about zero if it exists. Our result is consistent with the results obtained by Tsubota *et al.* in [60] since the cell used in their simulations has

the swelling ratio of 0.7. When suspending a cell in Poiseuille flow in a wider channel, the cell with non-uniform natural state ($\alpha = 1$) swings several times first. Then the cell migrates away from the centerline of the channel. This result suggests that cell with a strong effect of shape memory has a similar behavior as a neutrally buoyant rigid particle. In a narrow channel, cell behavior is much more complicated, it can change to slippery shape or parachute shape depending on the Capillary number, and the cell tank–treads when in slippery shape if α is low, but gets to an equilibrium shape if α is large.

Next we extend the model into three dimensions, based on the model suggested by Tsubota *et al.* in [61]. Consider the reference shape as a biconcave shape given by shrinking about 36% volume of a cell from sphere shape. We have discussed how to obtain the initial shape of the cell, and the resulting shape has been used as the shape of memory. We have validated first the model and numerical methods by comparing several aspects with experimental results or other simulation results. Then we have modeled the cell in shear flow with very small shear rates, and instead of tank–treading motion which usually happen in moderate and high shear rates, the cell performs tumbling motion, with its biconcave shape almost unchanged. When cell is tumbling, the membrane particle which was in the dimple cannot go back to dimple during tumbling, although it goes back and forth in some range. We have also observed that the cell with different coarse–grained levels shows similar behavior when tumbling, but the transition between tumbling and tank–treading decreases as cell membrane mesh is finer. The intermittency has not been observed in 3D simulations because the increment in shear rate we have tested is $5s^{-1}$, and as suggested in the 2D results, intermittency occurs in an extremely narrow range of shear rates. Also, we have suspended the cell into tube Poiseuille flow, cell changes to either a parachute shape or a 2D parachute for all choices of Capillary number if the channel height is the same as the channel width, and may show some asymmetric shapes when the height is not equal to the

width. We have discussed the dependency of cell equilibrium shapes on the channel height, the Capillary number (determined by the pressure gradient), and the coefficient α. Due to our setting of the channel, the x direction of the channel also has its effects on the cell behavior, and hence the cell motions departs from the 2D results which can only represent the 3D slit Poiseuille flow results (see, e.g., [56]) very well. Furthermore, we have consider the flow through a micro-channel with blockage and recorded the cell behavior after it comes out from the narrower part. Consistent with the experimental observation, the cell with nonuniform natural state first changes to a cup-shape very quickly, and then turns to a biconcave shape with a rotation in cell orientation during a long period of time. The cell with uniform natural state also changes to cup-shape first; but afterwards, it recovers to a biconcave disk shape without any rotation, and the marked dimple membrane particle does not tank–tread back to dimple.

1.2 Dissertation outline

Now we outline the composition of this dissertation:

In Chapter 2, we discuss the models and numerical methods used in this dissertation. The fluid inside and outside cell membrane is described by Navier-Stokes equation, and the cell membrane in both 2D and 3D are approximated by spring networks. The cell-fluid interaction is treated by the Immersed boundary method. For irregular domain, we adopt the Fictitious domain method. The coupled problem is solve by operator splitting scheme with forward Euler in time. The solution of each resulting operator, as well as the finite element approach/Euler's method will be also discussed.

In Chapter 3, we have validated our proposed 2D model and methods by two parts:

(i) the tank–treading motion of cell with uniform natural state at different swelling ratios in shear flow, and (ii) the go-and-stop experiments to illustrate that only cells with nonuniform natural state can have the "dimple back to dimple" behavior. Then we present numerical results of cell motion in shear flow, including the discussion of all three types of cell motion and especially the swinging motion. Next we provide the detail description of the intermittent behavior and the effect of the natural state on the intermittency. And finally we focus the results of cell motions in Poiseuille flow.

In Chapter 4, we consider three-dimensional cases. Similarly, first, we validate the model and methods by three parts: (i) the stretching test, (ii) cell tank–treading in shear flow, and (iii) the go-and-stop experiments. Then we study the cell tumbling motion in shear flow with very low shear rates. Next we consider the cell moving in tube Poiseuille flow, and study the effect of several aspects on the cell equilibrium shapes. And, at last, the cell behavior in a micro-channel with blockage has been studied.

Chapter 2

Models and numerical methods

2.1 Two dimensional model

A cell with a non-spherical rest shape is suspended in a domain Ω filled with a fluid which is incompressible and Newtonian as in Figure 2.1. The inclination angle and phase angle are defined as in Figure 2.1b and 2.1d. respectively. For some $T > 0$, the governing equations for the fluid–cell system are the Navier–Stokes equations

$$\rho\left(\frac{\partial \mathbf{u}}{\partial t} + \mathbf{u}\cdot\nabla\mathbf{u}\right) = -\nabla p + \mu\triangle\mathbf{u} + \mathbf{f},\ \text{in } \Omega\times(0,T), \tag{2.1}$$

$$\nabla\cdot\mathbf{u} = 0,\ \text{in } \Omega\times(0,T). \tag{2.2}$$

with the following boundary and initial conditions:

$$\mathbf{u} = \mathbf{u}_{max} \text{ on the top and } -\mathbf{u}_{max} \text{ on the bottom of } \Omega \tag{2.3}$$

$$\mathbf{u} \text{ is periodic in the } x \text{ direction,} \tag{2.4}$$

$$\mathbf{u}(\mathbf{x},0) = \mathbf{u}_0(\mathbf{x}),\ \text{in } \Omega \tag{2.5}$$

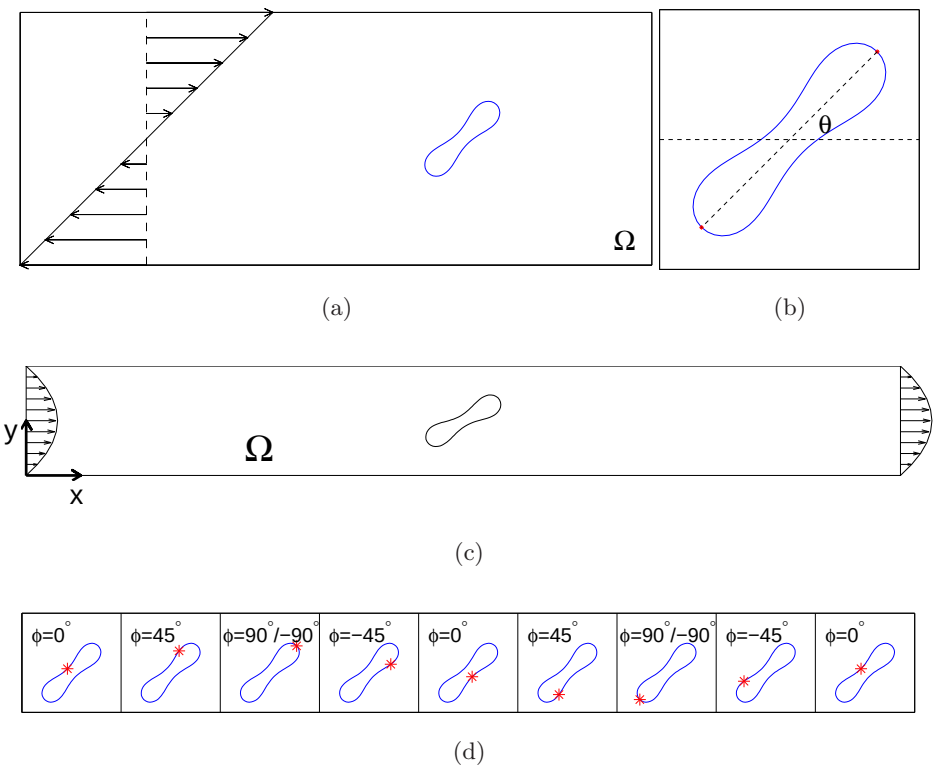

Figure 2.1: Schematic diagram of (a) a single red blood cell in shear flow with the computational domain Ω, (b) the inclination angle θ, (c) a single red blood cell in Poiseuille flow with the computational domain Ω, and (d) the phase angle ϕ.

where $\mathbf{u}$ and p are the fluid velocity and pressure, respectively, ρ is the fluid density, and μ is the fluid viscosity, which is assumed to be constant for the entire fluid. In (2.1), $\mathbf{f}$ is a body force which is the sum of $\mathbf{f}_p$ and $\mathbf{f}_B$ where $\mathbf{f}_B$ accounts for the force acting on the fluid/cell interface. The boundary condition in (2.3) is $\mathbf{u}_{max} = (U, 0)^t$ for simple shear flow. In (2.5), $\mathbf{u}_0(\mathbf{x})$ is the initial fluid velocity. For the cases of shear flow, $\mathbf{f}_p$ is set to be zero. For the case of Poiseuille flow, U is zero and f_p is the pressure gradient.

An elastic spring model used in [60] is considered to describe the deformable behavior

and elasticity of RBC. Based on this model, the cell membrane can be viewed as membrane particles connecting with the neighboring membrane particles by springs, as shown in Figure 2.2. Energy stores in the spring due to the change of the length l of the spring

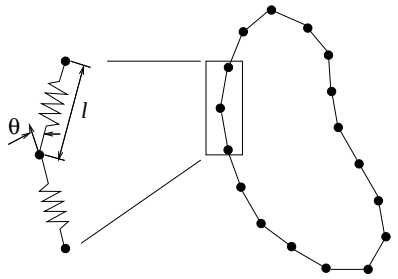

Figure 2.2: The elastic spring model of the 2D cell membrane.

with respect to its reference length l_0 and the change in angle θ between two neighboring springs. The total energy per unit thickness of the cell membrane, $E = E_l + E_b$, is the sum of the one for stretch and compression and the one for the bending which, in particular, are

$$E_l = \frac{k_l}{2}\sum_{i=1}^{N}(\frac{l_i - l_0}{l_0})^2, \quad E_b = \frac{k_b}{2}\sum_{i=1}^{N}\tan^2(\frac{\theta_i - \theta_i^0}{2}). \tag{2.6}$$

In equation (2.6), N is the total number of the spring elements, and k_l and k_b are spring constants for changes in length and bending angle, respectively. The set of reference angles $\{\theta_i^0\}_{i=1}^N$ corresponds to a preset natural state, where $\theta_i^0 = constant$ for all i corresponds to a uniform natural state, and otherwise a nonuniform natural state, which will give the model a shape memory property. The term E_b defined in (2.6) plays a role like the elastic energy introduced by Skotheim and Secomb in [57]. But our simulations show, which will be stated in next sections, a fully non–uniform biconcave natural state takes away too much freedom from membrane particles, and will destroy some nice properties of the cell with less non–uniformity. We believe that the cell has some effect of shape memory (which

comes from non–uniformity) as well as some kind of freedom to let membrane particles tank–tread (which behaves like the membrane particles are uniform). Unlike Tsubota *et al.* [60] who scale the reference angles as $\{\delta\theta_i^0\}_{i=1}^N$, which changes the memory of cell shape, we choose to keep the reference angles as a biconcave shape and study the the effect of shape memory. We modify the bending energy per unit thickness as a weighted sum of ones from both uniform and nonuniform natural states:

$$E_b = \frac{k_b}{2}\left((1-\alpha)\sum_{i=1}^{N}\tan^2\left(\frac{\theta_i}{2}\right) + \alpha\sum_{i=1}^{N}\tan^2\left(\frac{\theta_i-\theta_i^0}{2}\right)\right). \tag{2.7}$$

Here, α indicates the effect of shape memory, called shape memory coefficient.

To obtain the initial shape which also serves as the reference, we preset the cell with an uniform natural state (i.e., $\alpha = 1$, $\theta_i^0 = 0$ for i =1, ..., N), the cell is assumed to be a circle of radius $R_0 = 2.8$ μm initially. The circle is discretized into $N = 76$ membrane particles so that 76 springs are formed by connecting the neighboring particles. The shape change is stimulated by reducing the total area of the circle through a penalty function

$$\Gamma_s = \frac{k_s}{2}(\frac{s-s_e}{s_e})^2 \tag{2.8}$$

where s and s_e are the time dependent area of the cell and the specified area of the cell, respectively, and the total energy per unit thickness is modified as $E + \Gamma_s$. Based on the principle of virtual work the force per unit thickness acting on the ith membrane particle now is

$$\mathbf{F}_i = -\frac{\partial(E+\Gamma_s)}{\partial\mathbf{r}_i} \tag{2.9}$$

where $\mathbf{r}_i$ is the position of the ith membrane particle. When the area is reduced, each RBC membrane particle moves on the basis of the following equation of motion:

$$m\ddot{\mathbf{r}}_i + \gamma\dot{\mathbf{r}}_i = \mathbf{F}_i \tag{2.10}$$

Here, $\dot{()}$ denotes time differentiation, m and γ represent the membrane particle mass and the membrane viscosity of the RBC, respectively. The position $\mathbf{r}_i$ of the ith membrane particle is obtained by discretizing (2.10) via a second order finite difference method.

In equations (2.7) and (2.8), k_l, k_b, and k_s represent energies [N m] per unit thickness, and thus the units of k_l, k_b, and k_s are Newton [N]. In this paper, we only consider the capillary number instead of shear rate, because it is the key number to determine the behavior of a cell in two–dimensional flow. The value of the swelling ratio of a cell is $s^* = s_e/(\pi R_0^2)$. The values of parameters for modeling cell membrane are as follows: The spring constant is $k_l = 5 \times 10^{-8}$ N, the penalty coefficient is $k_s = 10^{-5}$ N, and the bending constant is $k_b = 5 \times 10^{-10}$ N. The cell is suspended in a fluid which has a density $\rho = 1.00$ g/cm^3 and a dynamical viscosity $\mu = 0.012$ g/(cm s). The viscosity ratio which describes the viscosity contrast of the inner and outer fluid of the cell membrane is fixed at 1.0.

2.2 Three–dimensional model

In 3D, we consider the computational domain as a tube as drawn in Figure 2.3. For shear flow the governing equation is (2.1)-(2.2) with the following boundary and initial conditions:

$$\mathbf{u} = \mathbf{g} \text{ on the top and the bottom of } \Omega, \tag{2.11}$$

$$\mathbf{u} \text{ is periodic in the } x \text{ and } z \text{ directions,} \tag{2.12}$$

$$\mathbf{u}(\mathbf{x}, 0) = \mathbf{u}_0(\mathbf{x}), \text{ in } \Omega. \tag{2.13}$$

where $\mathbf{g} = \mathbf{u}_{max}$ on the top of Ω and $-\mathbf{u}_{max}$ on the bottom of Ω . Since our boundary condition is periodic in x and z direction also, this give an insight how cell behaves when channel is infinitely long and wide, so that only height of channel affects cell motions. For

Poiseuille flow, we adopt the following boundary condition:

$$\mathbf{u} \text{ is periodic in the } z \text{ directions,} \tag{2.14}$$

$$\mathbf{u} = \mathbf{0} \text{ elsewhere on } \partial\Omega, \tag{2.15}$$

$$\mathbf{u}(\mathbf{x}, 0) = \mathbf{u}_0(\mathbf{x}), \text{ in } \Omega. \tag{2.16}$$

With the same idea of the previous section where 2D case is considered, in 3D, the cell membrane surface is composed of triangles whose three edges are elastic springs.

Following Tsubota et. al. in [61], and to assure the effect of shape memory, we have considered the natural states in terms of spring lengths and angles between surfaces, where the stretching and bending energies are defined as

$$E_l = \frac{k_l}{2}\left(\sum_{i=1}^{N_s}(l_i - l_i^S)^2 + \alpha\sum_{i=1}^{N_s}(l_i - l_i^0)^2\right) \tag{2.17}$$

$$E_b = \frac{k_b N_s}{2\sum_{i=1}^{N_s} l_i^S}\left(\sum_{i=1}^{N_s} l_i \tan^2\left(\frac{\theta_i}{2}\right) + \alpha\sum_{i=1}^{N_s} l_i \tan^2\left(\frac{\theta_i - \theta_i^0}{2}\right)\right). \tag{2.18}$$

In (2.17) and (2.18), N_s is the number of springs, k_l and k_b are corresponding stretching and bending constants, N_s is the number of springs, l_i and θ_i is the instant length of the ith spring and angle between the two neighbouring membrane elements whose common edge is the ith spring. l_i^S is the spring length when membrane is a sphere in stress free state, i.e. swelling ratio=1, and l_i^0, θ_i^0 are the reference spring lengths and angles. The cell shape would change from a sphere to a biconcave disk with carefully chosen parameters which will be discussed in chapter 4. Since it is impossible to cover a sphere surface by triangular elements that have all sides lengths the same, we cannot make the ideal case as in 2D that all spring length are the same, which means, the membrane particles are not identical and we have to find a weaker definition of nonuniform natural state. Similar to [61], the nonuniform natural state can be set the same as the equilibrium initial biconcave

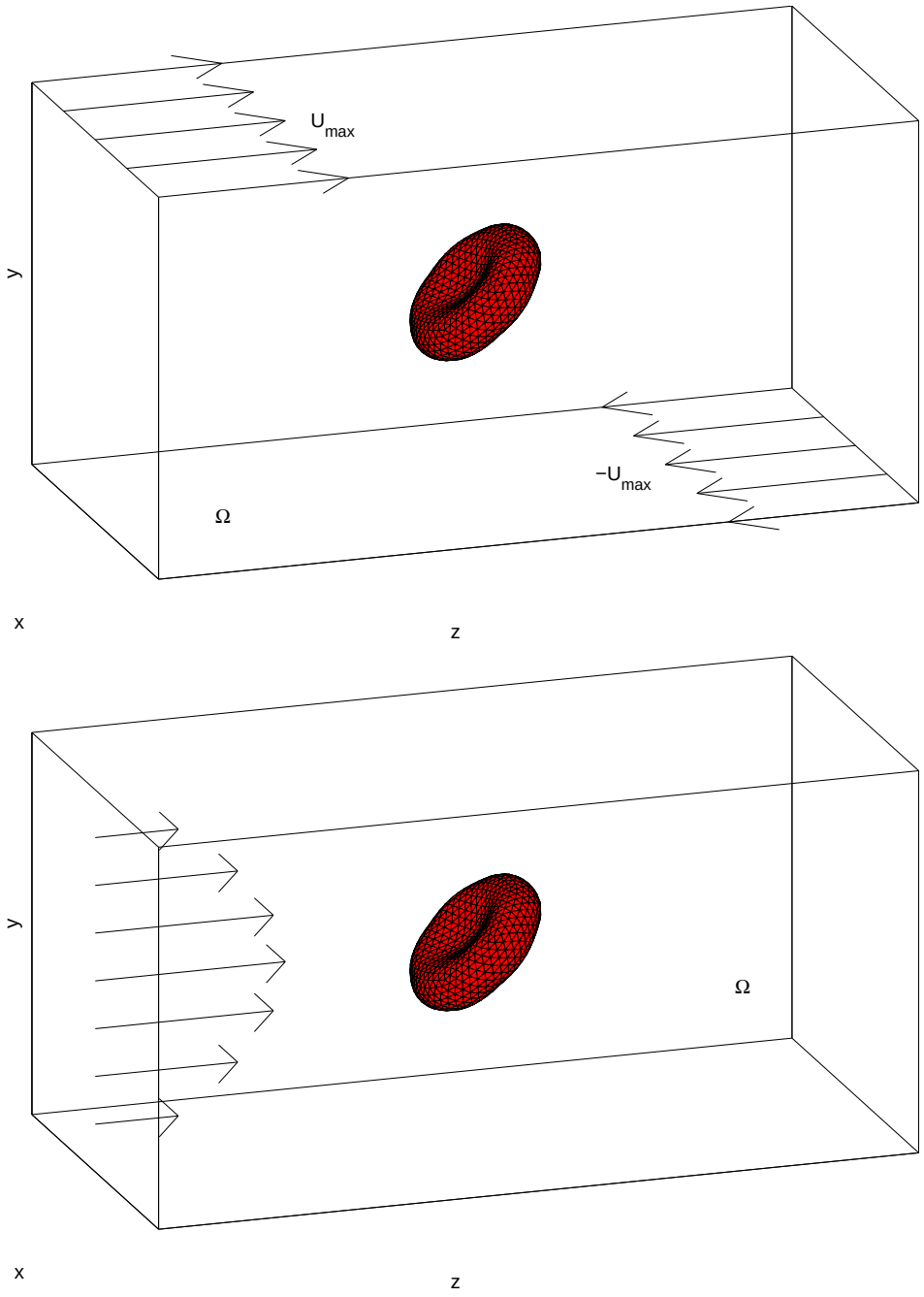

Figure 2.3: Schematic diagram of a single red blood cell with the computational domain Ω in shear flow (top) and Poiseuille flow (bottom).

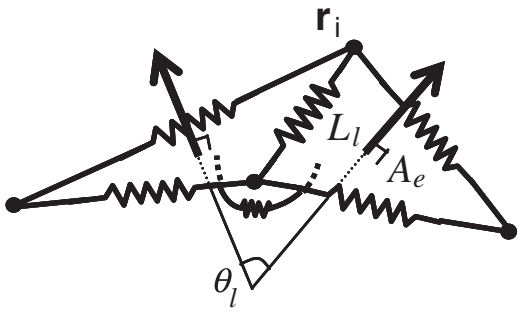

Figure 2.4: The elastic spring model for 3D red blood cell membrane.

shape, while the nonuniform natural state could be with spring lengths $\{l_i^S\}_{i=1}^{N_s}$ and angles of a flat membrane (all reference angles equal to 0 and hence not presented in (2.18). Just as the model in 2D, the number α indicates the effect of shape memory, and is called shape memory coefficient, $\alpha \geq 0$; when α takes the smallest value 0, the memory of biconcave shape would not take any effect in the energy and therefore that corresponds to the uniform natural state. With large α values, cell would have stronger effect of memory, and in our simulation the strongest case would not exceed $\alpha = 1$ (usually much smaller) because as suggested in Chapter 3, to recover cell dynamics in flows, shape memory should exist and "be small".

Considering the incompressibility of the cell membrane, the elastic energy coming from the change of local element-wise areal change, and change of global membrane surface area are given by

$$E_a = \frac{1}{2} k_a \sum_{j=1}^{N_e} \left(\frac{A_j - A_j^0}{A_j^0} \right)^2 A_j^0 \tag{2.19}$$

$$E_A = \frac{1}{2} k_A \left(\frac{\sum_{j=1}^{N_e} A_j - A^0}{A^0} \right)^2 A^0, \tag{2.20}$$

In (2.19) and (2.20), N_e is the number of triangular elements, A_j and A_j^0 are the instant and reference local areas of the jth element, A^0 is the reference global area. k_a and k_A are area expansion modulus for local triangular elements and global membrane surface, respectively. These two constants are chosen to be large compared to k_l and k_b to ensure the area incompressibility of the membrane.

To obtain the initial shape, which also serves as the reference shape of memory (recorded by means of spring lengths l_i^0 and angles between neighbouring elements θ_i^0), we preset the cell with pure uniform natural state (i.e. $\alpha = 0$), which assumes a sphere of surface area $135\mu m^2$. The sphere surface is approximated by N_e triangular elements, where the lengths of all edges are adjusted to have similar values. We adopt a penalty function Γ_V in addition the aforementioned four elastics energies, to force the cell volume reduced from a sphere to a biconcave disk with the target volume V_t (fixed to be $94\mu m^3$ in our simulation)

$$\Gamma = \frac{1}{2} k_V \left(\frac{V - V_t}{V_t} \right)^2 V_t. \tag{2.21}$$

Here V is the instant volume of cell, and k_V is the penalty coefficient, which should be large to maintain the fixed target volume of RBC. The total energy storing in cell membrane is therefore the sum of (2.17)-(2.21), and hence the force acting on each membrane particle is given by

$$\mathbf{F}_i = -\frac{\partial W}{\partial \mathbf{r}_i}, \quad \text{where } W = E_l + E_b + E_a + E_A + \Gamma_V. \tag{2.22}$$

Once the initial shape is obtained by (2.22) and (2.10), we choose this shape to be the reference shape of memory, so that the energy through (2.17) - (2.20) is also minimized for all choices of $\alpha \geq 0$, that ensured our cell preserves a biconcave shape when in stress-free state.

Here are the values we take for the cell model: The stretching constant is $k_l = 7.5 \times 10^{-6}$ [N/m], bending constant is $k_b = 60 \times 10^{-19}$ [N m], the coefficients for global and local

area conservation are $k_A = 5 \times 10^{-3}$ [N/m], $k_a = 10^{-2}$ [N/m], respectively, the penalty coefficient for volume conservation $k_V = 50$ [N/m^2]. The target volume V_t is fixed to be $94\mu m^3$, and the reference local/global area are set to be the values from sphere shape considering areal preservation. The fluid inside and outside the cell membrane is to have a density $\rho = 1.00\text{g/cm}^3$ and a dynamical viscosity $\mu = 0.012\text{g/(cm}s)$. The viscosity ratio is fixed at 1.0 in our work.

2.3 Numerical Implementation

The motion of RBC in the fluid flow is simulated by combining the immersed boundary method [47, 48, 49] and the aforementioned elastic spring models for membrane. The Navier–Stokes equations for fluid flow have been solved by using an operator splitting technique and finite element method [25, 53] with a regular triangular mesh so that the specialized fast solver, such as FISHPAK by Adams et al. [2], can be used to solve the fluid flow. The motion of RBC in a non-rectangular domain can be solve by using a fictitious domain method with distributed Lagrange multipliers (DLM/FD) [24, 43].

2.3.1 Formulation of the problem

Consider equations (2.1)-(2.2), with given initial and boundary conditions, e.g., (2.3)-(2.5) for 2D flows, or (2.11)-(2.13) for 3D shear flow and (2.14)-(2.16) for 3D Poiseuille flow. The computational domain $\Omega \subset I\!R^d$, is a rectangle in dimension d, $d = 2, 3$. The body force $\mathbf{f}$ is obtained by combining the force from the cell membrane, and will be discussed in a later subsection.

Applying the *virtual power* principle to system (2.1)-(2.2) yields the following *formulation*:

$$
\begin{aligned}
&\textit{For a.e. } t>0,\ \textit{find } \mathbf{u}(t)\in V_{\mathbf{g}},\ p(t)\in L^2_0(\Omega),\ \textit{such that}\\
&\begin{cases}
\rho\displaystyle\int_\Omega\left(\frac{\partial\mathbf{u}}{\partial t}+(\mathbf{u}\cdot\boldsymbol{\nabla})\mathbf{u}\right)\cdot\mathbf{v}\ d\mathbf{x}+\mu\int_\Omega\boldsymbol{\nabla}\mathbf{u}:\boldsymbol{\nabla}\mathbf{v}\ d\mathbf{x}-\int_\Omega p\boldsymbol{\nabla}\cdot\mathbf{v}\,d\mathbf{x}\\
\qquad\qquad=\displaystyle\int_\Omega\mathbf{f}\cdot\mathbf{v}\,d\mathbf{x},\ \forall\mathbf{v}\in V_0,
\end{cases} \qquad (2.23)\\
&\int_\Omega q\boldsymbol{\nabla}\cdot\mathbf{u}(t)\,d\mathbf{x}=0,\ \forall q\in L^2(\Omega), \qquad (2.24)\\
&\mathbf{u}(0)=\mathbf{u}_0,\ \textit{with } \boldsymbol{\nabla}\cdot\mathbf{u}_0=0 \qquad (2.25)
\end{aligned}
$$

with the *functional spaces*

$$V_{\mathbf{g}}=\{\mathbf{v}\mid\mathbf{v}\in H^1(\Omega)^d,\ \mathbf{v}\text{ satisfies the given boundary condition on }\Gamma\}, \quad (2.26)$$

$$V_0=H^1_0(\Omega)^d, \quad (2.27)$$

$$L^2_0(\Omega)=\{q\mid q\in L^2(\Omega),\ \int_\Omega q\,d\mathbf{x}=0\}. \quad (2.28)$$

2.3.2 Discretization

We use P_1-*iso*-P_2 and P_1 finite elements for the velocity field and pressure, respectively (as in [5] and [7]). More precisely with h a *space discretization step* we introduce a uniform finite–element triangulation $\mathcal{T}_h$ of $\overline{\Omega}$ and then $\mathcal{T}_{2h}$ a triangulation twice coarser (in practice we should construct $\mathcal{T}_{2h}$ first and then $\mathcal{T}_h$ by joining the midpoints of the edges of $\mathcal{T}_{2h}$, dividing thus each triangle of $\mathcal{T}_{2h}$ into 4 similar sub-triangles).

We define the following finite dimensional spaces which approximate $V_{\mathbf{g}}$, $H^1_0(\Omega)^d$, $L^2(\Omega)$,

and $L^2_0(\Omega)$, respectively:

$$V_{\mathbf{g}_h} = \{\mathbf{v}_h \mid \mathbf{v}_h \in (C^0(\overline{\Omega}))^d,\ \mathbf{v}_h|_T \in (P_1)^d,\ \forall T \in \mathcal{T}_h,$$
$$\mathbf{v}_h|_\Gamma \text{ satisfies the given boundary condition}\}, \tag{2.29}$$

$$V_{0h} = \{\mathbf{v}_h \mid \mathbf{v}_h \in (C^0(\overline{\Omega}))^d,\ \mathbf{v}_h|_T \in (P_1)^d,\ \forall T \in \mathcal{T}_h,\ \mathbf{v}_h|_\Gamma = \mathbf{0}\}, \tag{2.30}$$

$$L^2_h = \{q_h \mid q_h \in C^0(\overline{\Omega}),\ q_h|_T \in P_1,\ \forall T \in \mathcal{T}_{2h}\}, \tag{2.31}$$

$$L^2_{0h} = \{q_h \mid q_h \in L^2_h,\ \int_\Omega q_h\, d\mathbf{x} = 0\}; \tag{2.32}$$

in (2.29)-(2.32), $\mathbf{g}_h$ is an approximation of $\mathbf{g}$ verifying $\displaystyle\int_\Gamma \mathbf{g}_h \cdot \mathbf{n}\, d\Gamma = 0$ and P_1 is the space of the polynomials in dimension $d = 2$ or 3 of degree ≤ 1.

Using the above finite dimensional spaces leads to the following approximation of problem (2.23)-(2.25):

$$\begin{aligned} &For\ t > 0\ find\ \mathbf{u}_h(t) \in V_{\mathbf{g}_h},\ p_h(t) \in L^2_{0h}\ such\ that \\ &\begin{cases} \rho \displaystyle\int_\Omega \frac{\partial \mathbf{u}_h}{\partial t} \cdot \mathbf{v}\, d\mathbf{x} + \rho \int_\Omega (\mathbf{u}_h \cdot \boldsymbol{\nabla})\mathbf{u}_h \cdot \mathbf{v}\, d\mathbf{x} + \mu \int_\Omega \boldsymbol{\nabla}\mathbf{u}_h : \boldsymbol{\nabla}\mathbf{v}\, d\mathbf{x} \\ \qquad = \displaystyle\int_\Omega p_h \boldsymbol{\nabla} \cdot \mathbf{v}\, d\mathbf{x} + \int_\Omega \mathbf{f} \cdot \mathbf{v}\, d\mathbf{x},\ \forall \mathbf{v} \in V_{0h},\ on\ (0,T), \end{cases} \end{aligned} \tag{2.33}$$

$$\int_\Omega q \boldsymbol{\nabla} \cdot \mathbf{u}_h(t) dx = 0,\ \forall q \in L^2_h, \tag{2.34}$$

$$\mathbf{u}_h(0) = \mathbf{u}_{0h}; \tag{2.35}$$

in (2.35), $\mathbf{u}_{0h}$ is an approximation of $\mathbf{u}_0$ so that $\displaystyle\int_\Omega q \boldsymbol{\nabla} \cdot \mathbf{u}_{0h}\, d\mathbf{x} = 0,\ \forall q \in L^2_h$.

Following Chorin, e.g., in [9, 10], most "modern" Navier-Stokes solvers are based on operator splitting algorithms (see, e.g., refs. [33], [63], [34] (Chapter 3) and [25] (Chapters 2 and 7)) in which the incompressibility condition is obtained via either a H^1-projection Stokes solver or a L^2-projection method. This approach still applies to the initial value problem (2.33)-(2.35) which contains two numerical difficulties to each of which can be associated a specific operator, namely

(a) The incompressibility condition and the related unknown pressure,

(b) An advection term.

The operator in (a) is a *projection operator*. From an abstract point of view, problem (2.33)-(2.35) is a particular case of the following class of initial value problems

$$\frac{d\varphi}{dt} + A(\varphi, t) + B(\varphi, t) + C(\varphi, t) = f, \quad \varphi(0) = \varphi_0, \tag{2.36}$$

where the operator A is associated to incompressibility, B to advection, and C to diffusion. Among the many operator-splitting methods which can be employed to solve (2.36), we have applied the Lie's scheme [11] to obtain the simple scheme discussed below, which is only first order accurate in time, but the low–order accuracy is compensated by its modular, easy implementation, good stability, and robustness properties. After dropping some of the subscripts h and applying the backward Euler's method for time discretization, we have

$$\mathbf{u}^0 = \mathbf{u}_{0h} \; \textit{is given}; \tag{2.37}$$

for $n \geq 0$, $\mathbf{u}^n$ being known,

$$\begin{cases} \rho \displaystyle\int_\Omega \frac{\mathbf{u}^{n+1/3} - \mathbf{u}^n}{\triangle t} \cdot \mathbf{v}\, d\mathbf{x} - \int_\Omega p^{n+1/3} \boldsymbol{\nabla} \cdot \mathbf{v}\, d\mathbf{x} = 0,\ \forall \mathbf{v} \in V_{0h}, \\ \displaystyle\int_\Omega q\, \boldsymbol{\nabla} \cdot \mathbf{u}^{n+1/3}\, d\mathbf{x} = 0,\ \forall q \in L^2_h; \\ \mathbf{u}^{n+1/3} \in V_{\mathbf{g}_h},\ p^{n+1/3} \in L^2_{0h}, \end{cases} \tag{2.38}$$

$$\begin{cases} \displaystyle\int_\Omega \frac{\partial \mathbf{u}(t)}{\partial t} \cdot \mathbf{v}\, d\mathbf{x} + \int_\Omega (\mathbf{u}^{n+1/3} \cdot \boldsymbol{\nabla})\mathbf{u}(t) \cdot \mathbf{v}\, d\mathbf{x} = 0 \text{ on } (t^n, t^{n+1}),\ \forall \mathbf{v} \in V_{0h}, \\ \mathbf{u}(t^n) = \mathbf{u}^{n+1/3}, \\ \mathbf{u}(t) \in V_h \text{ on } (t^n, t^{n+1}), \end{cases} \tag{2.39}$$

$$\mathbf{u}^{n+2/3} = \mathbf{u}(t^{n+1}),$$

$$\begin{cases} \rho \displaystyle\int_\Omega \frac{\mathbf{u}^{n+1} - \mathbf{u}^{n+2/3}}{\triangle t} \cdot \mathbf{v}\, d\mathbf{x} + \mu \int_\Omega \boldsymbol{\nabla}\mathbf{u}^{n+1} : \boldsymbol{\nabla}\mathbf{v}\, d\mathbf{x} = \int_\Omega \mathbf{f} \cdot \mathbf{v}\, d\mathbf{x},\ \forall \mathbf{v} \in V_{0h}, \\ \mathbf{u}^{n+1} \in V_{\mathbf{g}_h}. \end{cases} \tag{2.40}$$

Thanks to the operator-splitting, the three subproblems in (2.38)-(2.40) are very classical problems and each one can be solved by many different available methods. This is really the key point of the operator–splitting methods.

2.3.3 The Solution of Subproblem (2.38)

The subproblem (2.38) has the following form (some h and n have been dropped):

$$\alpha \int_\Omega \mathbf{u} \cdot \mathbf{v} d\mathbf{x} - \int_\Omega p \boldsymbol{\nabla} \cdot \mathbf{v} d\mathbf{x} = \alpha \int_\Omega \mathbf{u}^* \cdot \mathbf{v} d\mathbf{x}, \forall \mathbf{v} \in V_{0h}, \tag{2.41}$$

$$\int_\Omega q \boldsymbol{\nabla} \cdot \mathbf{u}\, d\mathbf{x} = 0, \forall q \in L^2_h, \tag{2.42}$$

with $\{\mathbf{u},\ p\} \in V_{\mathbf{g}_h} \times L^2_{0h}$, where $\alpha = \rho/\triangle t$.

Problem (2.41)-(2.42) is a a degenerated discrete Stokes problem, and $\mathbf{u}$ can be interpreted as the L^2-projection of $\mathbf{u}^*$ on the subspace of $V_{\mathbf{g}_h}$ consisting of those functions

satisfying

$$\int_{\Omega} q\boldsymbol{\nabla}\cdot\mathbf{v}\,d\mathbf{x}=0,\forall q\in L_h^2. \tag{2.43}$$

The pressure p is the Lagrange multiplier associated to the linear constraint in (2.42); p is not unique unless we specify an additional relation, for example, $p\in L_{0h}^2$.

The saddle point problem (2.41)-(2.42) can be solved by a Uzawa/Preconditioned Conjugate Gradient algorithm operating in the space L_{0h}^2 in [25] (Section 21), which is as follows:

Step 0: Initialization

$$p^0\in L_{0h}^2 \text{ is given;} \tag{2.44}$$

solve the projection problem:

$$\begin{cases}\alpha\displaystyle\int_{\Omega}\mathbf{u}^0\cdot\mathbf{v}d\mathbf{x}=\alpha\int_{\Omega}\mathbf{u}^*\cdot\mathbf{v}d\mathbf{x}+\int_{\Omega}p^0\boldsymbol{\nabla}\cdot\mathbf{v}d\mathbf{x},\forall\mathbf{v}\in V_{0h},\\ \mathbf{u}^0\in V_{\mathbf{g}_h},\end{cases} \tag{2.45}$$

then

$$\begin{cases}\displaystyle\int_{\Omega}r^0qd\mathbf{x}=\int_{\Omega}q\boldsymbol{\nabla}\cdot\mathbf{u}^0d\mathbf{x},\forall q\in L_h^2,\\ r^0\in L_h^2,\end{cases} \tag{2.46}$$

and finally

$$\begin{cases}\displaystyle\int_{\Omega}\boldsymbol{\nabla}\phi^0\cdot\boldsymbol{\nabla}qd\mathbf{x}=\int_{\Omega}r^0qd\mathbf{x},\forall q\in L_h^2,\\ \phi^0\in L_{0h}^2.\end{cases} \tag{2.47}$$

Then set

$$g^0=\alpha\ \phi^0 \tag{2.48}$$

$$w^0=g^0. \tag{2.49}$$

Step 1: Descent

Then for $k \geq 0$, assuming that $\mathbf{u}^k$, p^k, r^k, g^k, w^k are known, compute $\mathbf{u}^{k+1}$, p^{k+1}, r^{k+1}, g^{k+1}, w^{k+1} as follows:

solve:

$$\begin{cases} \alpha \int_\Omega \bar{\mathbf{u}}^k \cdot \mathbf{v} d\mathbf{x} = \int_\Omega w^k \boldsymbol{\nabla} \cdot \mathbf{v} d\mathbf{x}, \forall \mathbf{v} \in V_{0h}, \\ \bar{\mathbf{u}}^k \in V_{\mathbf{g}_h}, \end{cases} \tag{2.50}$$

then

$$\begin{cases} \int_\Omega \bar{r}^k q d\mathbf{x} = \int_\Omega q \boldsymbol{\nabla} \cdot \bar{\mathbf{u}}^k d\mathbf{x}, \forall q \in L_h^2, \\ \bar{r}^k \in L_h^2, \end{cases} \tag{2.51}$$

and finally

$$\begin{cases} \int_\Omega \boldsymbol{\nabla} \bar{\phi}^k \cdot \boldsymbol{\nabla} q d\mathbf{x} = \int_\Omega \bar{r}^k q d\mathbf{x}, \forall q \in L_h^2, \\ \bar{\phi}^k \in L_{0h}^2. \end{cases} \tag{2.52}$$

Compute

$$\rho_k = \frac{\int_\Omega r^k g^k d\mathbf{x}}{\int_\Omega \bar{r}^k w^k d\mathbf{x}}, \tag{2.53}$$

and then

$$\mathbf{u}^{k+1} = \mathbf{u}^k - \rho_k \ \bar{\mathbf{u}}^k, \tag{2.54}$$

$$p^{k+1} = p^k - \rho_k \ w^k, \tag{2.55}$$

$$r^{k+1} = r^k - \rho_k \ \bar{r}^k, \tag{2.56}$$

$$g^{k+1} = g^k - \rho_k \alpha \ \bar{\phi}^k, \tag{2.57}$$

Step 2: Convergence test and new descent direction

If

$$\frac{\int_\Omega r^{k+1} g^{k+1} d\mathbf{x}}{\int_\Omega r^0 g^0 d\mathbf{x}} \leq \epsilon,$$

take $p = p^{k+1}$ and $\mathbf{u} = \mathbf{u}^{k+1}$; otherwise, compute

$$\gamma_k = \frac{\int_\Omega r^{k+1} g^{k+1} d\mathbf{x}}{\int_\Omega r^k g^k d\mathbf{x}}, \tag{2.58}$$

and set

$$w^{k+1} = g^{k+1} + \gamma_k w^k. \tag{2.59}$$

Do k=k+1 and go back to (2.50).

In above algorithm, problems (2.47) and (2.52) at preconditioned steps are classical elliptic problems and are solved by a matrix-free fast solver from FISHPAK [2]. For the problems (2.45) and (2.50), the mass matrix is a diagonal matrix so there is no need to solve any linear system.

2.3.4 The Solution of the Advection Subproblem

Solving the pure advection problem (2.39) is a more delicate issue. Clearly, problem (2.39) can be solved by a *method of characteristics* (see, e.g., refs. [23] and [50] and the references therein). We solve the advection problem by a wave-like equation method (e.g., see [14] and [25] (Section 31)). It follows from that after translation and dilation on the time axis, each component of the velocity vector $\mathbf{u}$ and the configuration stress tensor A is a solution of a transport equation of the following type:

$$\begin{cases} \dfrac{\partial \varphi}{\partial t} + (\mathbf{U} \cdot \boldsymbol{\nabla})\varphi = 0, \; in\, \Omega \times (0,1), \\ \varphi(0) = \varphi_0, \; \varphi = g \; on \; \Gamma^- \times (0,1), \end{cases} \tag{2.60}$$

The properties $\boldsymbol{\nabla} \cdot \mathbf{U} = 0$ and $\partial \mathbf{U}/\partial t = 0$ on $\Omega \times (0,1)$ imply that problem (2.60) is equivalent to the (formally) well-posed problem:

$$\begin{cases} \dfrac{\partial^2 \varphi}{\partial t^2} - \boldsymbol{\nabla} \cdot ((\mathbf{U} \cdot \boldsymbol{\nabla} \varphi)\mathbf{U}) = 0, \, in \, \Omega \times (0,1), \\ \varphi(0) = \varphi_0, \, \dfrac{\partial \varphi}{\partial t}(0) = -\mathbf{U} \cdot \boldsymbol{\nabla} \varphi_0, \\ \varphi = g \; on \; \Gamma^- \times (0,1), (\mathbf{U} \cdot \mathbf{n})(\dfrac{\partial \varphi}{\partial t} + (\mathbf{U} \cdot \boldsymbol{\nabla})\varphi) = 0 \; on \; \Gamma \backslash \Gamma^- \times (0,1). \end{cases} \tag{2.61}$$

Solving the wave-like equation (2.61) by a classical finite element/time stepping method is quite easy since a variational formulation of (2.61) is given by

$$\begin{cases} \displaystyle\int_\Omega \frac{\partial^2 \varphi}{\partial t^2} v \, d\mathbf{x} + \int_\Omega (\mathbf{U} \cdot \boldsymbol{\nabla} \varphi)(\mathbf{U} \cdot \boldsymbol{\nabla} v) \, d\mathbf{x} \\ \quad + \displaystyle\int_{\Gamma \backslash \Gamma^-} \mathbf{U} \cdot \mathbf{n} \frac{\partial \varphi}{\partial t} v d\Gamma = 0, \, \forall v \in W_0, \\ \varphi(0) = \varphi_0, \, \dfrac{\partial \varphi}{\partial t}(0) = -\mathbf{U} \cdot \boldsymbol{\nabla} \varphi_0, \\ \varphi = g \; on \; \Gamma^- \times (0,1), \end{cases} \tag{2.62}$$

with the test function space W_0 defined by

$$W_0 = \{v | \; v \in H^1(\Omega), \; v = 0 \; on \; \Gamma^-\}.$$

Let H_h^1 be a C^0- conforming finite element subspace of $H^1(\Omega)$ as discussed in, e.g., Ciarlet ([12],[13]). We define $W_{0h} = H_h^1 \cap W_0$; we suppose that $\lim_{h \to 0} W_{0h} = W_0$ in the usual element sense. Next, we define $\tau_1 > 0$ by $\tau_1 = \triangle t/Q$, where Q is a positive integer (and we discretize problem (2.62) by

$$\varphi^0 = \varphi_{0h} (\approx \varphi_0), \tag{2.63}$$

$$\begin{cases} \displaystyle\int_\Omega (\varphi^{-1} - \varphi^1) v \, d\mathbf{x} = 2\tau_1 \int_\Omega (\mathbf{U}_h \cdot \boldsymbol{\nabla} \varphi^0) v \, d\mathbf{x}, \, \forall v \in W_{0h}, \\ \varphi^{-1} - \varphi^1 \in W_{0h}, \end{cases} \tag{2.64}$$

and for $q = 0, 1, \cdots, Q-1$,

$$\begin{cases} \varphi^{q+1} \in H_h^1,\ \varphi^{q+1} = g_h \ \ on\ \Gamma^-, \\ \displaystyle\int_\Omega \frac{\varphi^{q+1} + \varphi^{q-1} - 2\varphi^q}{\tau_1^2} v\, d\mathbf{x} + \int_\Omega (\mathbf{U}_h \cdot \boldsymbol{\nabla}\varphi^q)(\mathbf{U}_h \cdot \boldsymbol{\nabla} v)\, d\mathbf{x} \\ \quad + \displaystyle\int_{\Gamma\setminus\Gamma^-} \mathbf{U}_h \cdot \mathbf{n} \left(\frac{\varphi^{q+1} - \varphi^{q-1}}{2\tau_1} \right) v d\Gamma = 0,\ \forall v \in W_{0h}, \end{cases} \tag{2.65}$$

where, $\mathbf{U}_h$ and g_h are the approximates of $\mathbf{U}$ and g respectively.

Remark 2.3.1. Scheme (2.63)-(2.65) is a centered scheme which is formally second-order accurate with respect to space and time discretizations. To be stable, scheme (2.63)-(2.65) has to verify a condition such as

$$\tau_1 \leq ch,$$

with c of order of $1/||\mathbf{U}||$. Since the advection problem is decoupled from the rest, we can choose proper time step here so that the above condition is satisfied. If one uses the trapezoidal rule to compute the first and the third integrals in (2.65), the above scheme becomes explicit, i.e., φ^{q+1} is obtained via the solution of a linear system with diagonal matrix.

2.3.5 Immersed boundary method

The immersed boundary method developed by Peskin, e.g, [47, 48, 49], is employed here because of its distinguish features in dealing with the problem of fluid flow interacting with a flexible fluid/structure interface. Over the years, it has demonstrated its CFD capability including blood flow simulations. Based on the method, the boundary of the deformable structure is discretized spatially into a set of boundary nodes.

The force located at the immersed boundary node $\mathbf{r}_i$ affects the nearby fluid mesh nodes

$\mathbf{x}$ through a discrete δ-function $D_h(\mathbf{x}-\mathbf{r}_i)$:

$$\mathbf{f}_B(\mathbf{x}) = \sum \mathbf{F}_i D_h(\mathbf{x}-\mathbf{r}_i) \quad \text{for} \quad |\mathbf{x}-\mathbf{r}_i| \le 2h, \tag{2.66}$$

where h is the uniform finite element mesh size and

$$D_h(\mathbf{x}-\mathbf{r}_i) = \sum_{j=1}^{d} \delta_h(x_j - r_{i,j}), \tag{2.67}$$

with $d = 2$ or 3, x_j is the jth component of $\mathbf{x}$ and $r_{i,j}$ is the jth component of $\mathbf{r}_i$. The 1D discrete δ-functions being defined by

$$\delta_h(z) = \begin{cases} \frac{1}{8h}\left(3 - 2|z|/h + \sqrt{1+4|z|/h - 4(|z|/h)^2}\right), & |z| \le h, \\ \frac{1}{8h}\left(5 - 2|z|/h - \sqrt{-7+12|z|/h - 4(|z|/h)^2}\right), & h \le |z| \le 2h, \\ 0, & \text{otherwise.} \end{cases} \tag{2.68}$$

The velocity of the immersed boundary node $\mathbf{r}_i$ is also affected by the surrounding fluid and therefore is enforced by summing the velocities at the nearby fluid mesh nodes $\mathbf{x}$ weighted by the same discrete δ-function:

$$\mathbf{U}(\mathbf{r}_i) = \sum h^d \mathbf{u}(\mathbf{x}) D_h(\mathbf{x}-\mathbf{r}_i) \quad \text{for} \quad |\mathbf{x}-\mathbf{r}_i| \le 2h. \tag{2.69}$$

At each time step, the position of the immersed boundary node is updated by

$$\mathbf{r}_i^{n+1} = \mathbf{r}_i^n + \Delta t \mathbf{U}(\mathbf{r}_i^n). \tag{2.70}$$

Therefore, (2.37)-(2.40) can be updated to the following:

$\mathbf{u}^0 = \mathbf{u}_{0h}$ is given; for $n \ge 0$, $\mathbf{u}^n$ being known, we compute the approximate solution via the following fractional steps:

1. Solve

$$\begin{cases} \rho\displaystyle\int_\Omega \frac{\mathbf{u}^{n+1/3}-\mathbf{u}^n}{\triangle t}\cdot\mathbf{v}\,d\mathbf{x} - \int_\Omega p^{n+1/3}\,\boldsymbol{\nabla}\cdot\mathbf{v}\,d\mathbf{x} = 0,\ \forall \mathbf{v}\in V_{0h}, \\ \displaystyle\int_\Omega q\,\boldsymbol{\nabla}\cdot\mathbf{u}^{n+1/3}\,d\mathbf{x} = 0,\ \forall q\in L_h^2; \\ \mathbf{u}^{n+1/3}\in V_{\mathbf{g}_h},\ p^{n+1/3}\in L_{0h}^2, \end{cases} \tag{2.71}$$

2. Update the position of the membrane by (2.69) and (2.70)

3. Solve

$$\begin{cases} \displaystyle\int_\Omega \frac{\partial \mathbf{u}(t)}{\partial t}\cdot\mathbf{v}\,d\mathbf{x} + \int_\Omega (\mathbf{u}^{n+1/3}\cdot\boldsymbol{\nabla})\mathbf{u}(t)\cdot\mathbf{v}\,d\mathbf{x} = 0 \text{ on } (t^n,t^{n+1}),\ \forall \mathbf{v}\in V_{0h}, \\ \mathbf{u}(t^n) = \mathbf{u}^{n+1/3}, \\ \mathbf{u}(t)\in V_h \text{ on } (t^n,t^{n+1}), \end{cases} \tag{2.72}$$

$$\mathbf{u}^{n+2/3} = \mathbf{u}(t^{n+1}),$$

4. Use the position obtained in step 2 to compute the force acting on the membrane by (2.9) for the 2D case or (2.22) for the 3D case, then obtain the force $\mathbf{f}_B$ on the fluid/cell interface by(2.66), (2.67), and (2.68). The force $\mathbf{f}$ is given by $\mathbf{f} = \mathbf{f}_p + \mathbf{f}_B$.

5. Solve

$$\begin{cases} \rho\displaystyle\int_\Omega \frac{\mathbf{u}^{n+1}-\mathbf{u}^{n+2/3}}{\triangle t}\cdot\mathbf{v}\,d\mathbf{x} + \mu\int_\Omega \boldsymbol{\nabla}\mathbf{u}^{n+1}:\boldsymbol{\nabla}\mathbf{v}\,d\mathbf{x} = \int_\Omega \mathbf{f}\cdot\mathbf{v}\,d\mathbf{x},\ \forall \mathbf{v}\in V_{0h}, \\ \mathbf{u}^{n+1}\in V_{\mathbf{g}_h}. \end{cases} \tag{2.73}$$

2.3.6 Fictitious–domain method for non-rectangular computational domains

Suppose now the computational domain is not a rectangle, then it can be viewed as $\Omega\setminus\overline{\omega}$, where Ω is a rectangular domain and $\overline{\omega}$ is the blockade. For example, for $d=3$, we consider the following domain:

The governing equations for the fluid-cell system then become

$$\rho\left(\frac{\partial \mathbf{u}}{\partial t}+\mathbf{u}\cdot\boldsymbol{\nabla}\mathbf{u}\right)=-\boldsymbol{\nabla}p+\mu\Delta\mathbf{u}+\mathbf{f}\ \text{in}\ \ \Omega\setminus\overline{\omega},\ t\in(0,T), \tag{2.74}$$

$$\boldsymbol{\nabla}\cdot\mathbf{u}=0\ \text{in}\ \ \Omega\setminus\overline{\omega},\ \ t\in(0,T), \tag{2.75}$$

with the following boundary and initial conditions:

$$\mathbf{u}\ \text{is periodic in the}\ z\ \text{direction}, \tag{2.76}$$

$$\mathbf{u}=\mathbf{0}\ \text{elsewhere on}\ \partial(\Omega\setminus\overline{\omega}), \tag{2.77}$$

$$\mathbf{u}(\mathbf{x},0)=\mathbf{u}_0(\mathbf{x}),\ \text{in}\ \Omega\setminus\overline{\omega}. \tag{2.78}$$

The distributed Lagrange multiplier/fictitious domain formulation for the flow problem (2.74)-(2.78) in a channel of constriction reads as follow:

$$\text{For}\ \ a.e.\ t>0,\ \text{find}\ \ \mathbf{u}(t)\in W_{0,P},\ p(t)\in L^2_0,\ \boldsymbol{\lambda}\in\Lambda\ \ \text{such that}$$

$$\begin{cases}\rho\displaystyle\int_\Omega\left(\frac{\partial \mathbf{u}}{\partial t}+(\mathbf{u}\cdot\boldsymbol{\nabla})\mathbf{u}\right)\cdot\mathbf{v}\ d\mathbf{x}+\mu\int_\Omega\boldsymbol{\nabla}\mathbf{u}:\boldsymbol{\nabla}\mathbf{v}\ d\mathbf{x}-\int_\Omega p\boldsymbol{\nabla}\cdot\mathbf{v}\,d\mathbf{x}\\ \qquad\qquad=\displaystyle\int_\Omega\mathbf{f}\cdot\mathbf{v}\,d\mathbf{x}+<\boldsymbol{\lambda},\mathbf{v}>,\ \forall\mathbf{v}\in W_{0,P},\end{cases} \tag{2.79}$$

$$\int_\Omega q\boldsymbol{\nabla}\cdot\mathbf{u}(t)d\mathbf{x}=0,\ \forall q\in L^2(\Omega), \tag{2.80}$$

$$<\boldsymbol{\mu},\mathbf{u}(t)>=0,\ \forall\boldsymbol{\mu}\in\Lambda, \tag{2.81}$$

$$\mathbf{u}(\mathbf{x},0)=\mathbf{u}_0(\mathbf{x}) \tag{2.82}$$

with

$$W_{0,P}=\{\mathbf{v}|\mathbf{v}\in(H^1(\Omega))^d,\ \mathbf{v}\ \text{is periodic in the}\ z\ \text{direction and}$$

$$\mathbf{v}=\mathbf{0}\ \text{elsewhere on}\ \partial\Omega\},$$

$$L^2_0=\{q|q\in L^2(\Omega),\int_\Omega q\,d\mathbf{x}=0\},$$

$$\Lambda=(H^1(\omega))^d.$$

In (2.79)-(2.82), $\boldsymbol{\lambda}$ is a *Lagrange multiplier* associated with relation (2.81) and $< \cdot, \cdot >$ is an inner product on Λ (see [44] for further information). We also use, if necessary, the notation $\phi(t)$ for the function $\mathbf{x} \to \phi(\mathbf{x}, t)$.

A finite dimensional space approximating Λ is defined as follows: let $\{\mathbf{x}_i\}_{i=1}^M$ be a set of points from $\overline{\omega}$ which cover $\overline{\omega}$ (uniformly, for example); we define then

$$\Lambda_h = \{\boldsymbol{\mu}_h | \boldsymbol{\mu}_h = \sum_{i=1}^{M} \boldsymbol{\mu}_i \delta(\mathbf{x} - \mathbf{x}_i),\ \boldsymbol{\mu}_i \in I\!R^d,\ \forall i = 1, ..., M\},$$

where $\delta(\cdot)$ is the Dirac measure at $\mathbf{x} = \mathbf{0}$. Then we shall use $< \cdot, \cdot >$ defined by

$$< \boldsymbol{\mu}_h, \mathbf{v}_h >= \sum_{i=1}^{M} \boldsymbol{\mu}_i \cdot \mathbf{v}_h(\mathbf{x}_i),\ \forall \boldsymbol{\mu}_h \in \Lambda_h,\ \mathbf{v}_h \in W_{0h}$$

where W_{0h} is the typical P_1 finite element approximation for $W_{0,P}$. A typical choice of points for defining Λ_h is to take the grid points of the velocity mesh internal to the region ω and whose distance to the boundary of ω is greater than, e.g. $h/2$, and to complete with selected points from the boundary of ω, but we exclude those points which are also on the boundary of Ω.

Then the scheme described in subsection 2.3.2 - 2.3.4 (or subsection 2.3.5) still applies here, we can use exactly the same approach except that one should added to the right hand side of equations 2.33 and 2.40 the term $< \boldsymbol{\lambda}, \mathbf{v}_h >$.

Chapter 3

Two–dimensional cell motion in flows

3.1 Validation

3.1.1 A single RBC tank–treading in the shear flow

First, we present the results on the simulation of a single RBC with uniform nature state (i.e., $\alpha = 0$ in eq. (2.7)) suspended in a linear shear flow with shear rate $\gamma = 500/\text{s}$. The dimensions of the computational domain are $100\mu\text{m} \times 7\mu\text{m}$ and $100\mu\text{m} \times 14\mu\text{m}$. The two degrees of confinement are 0.8 for the narrower domain and 0.4 for the wider domain, respectively. The grid resolution for the computational domain is 80 grid points per 10μm. The time step Δt is 1×10^{-5}ms. The initial velocity of the fluid flow is zero everywhere and the initial positions of the mass center of the cell are the center of both domains. In both wider and narrower domains, the cell performs a steady tank–treading motion with

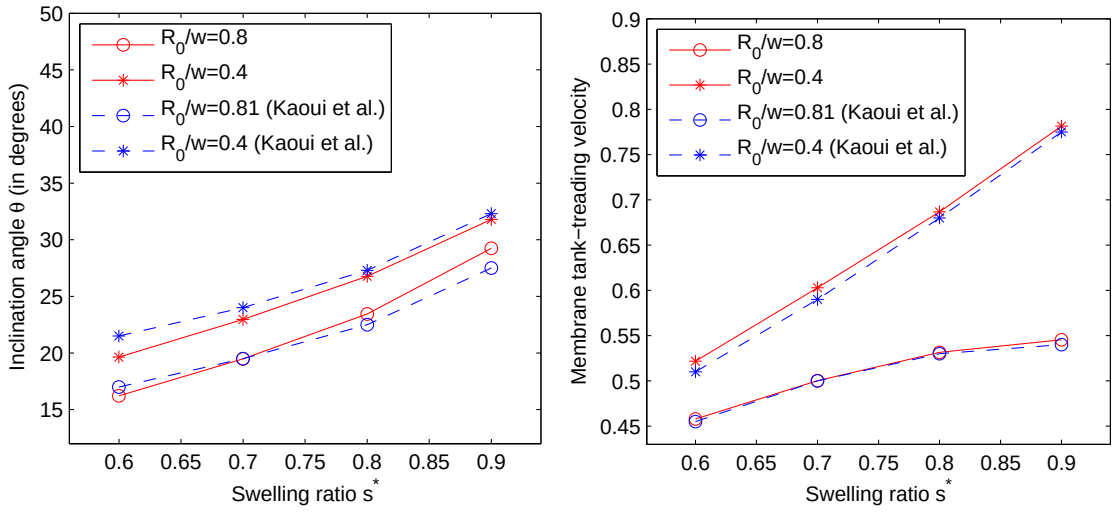

Figure 3.1: Steady inclination angle (left) and membrane tank-treading velocity (right) as a function of the cell swelling ratio for two degrees of confinement R_0/w= 0.4 and 0.8.

a fixed inclination angle depending on the swelling ratio s^* and degree of confinement. The steady inclination angles and the membrane tank–treading velocities of two different degrees of confinement for five values s^*= 0.6, 0.7, 0.8 and 0.9 are presented in Figure 3.1, which show good agreement with the results by Kaoui, Harting and Misbah [29]. The inclination angle increases monotonically for both two degrees of confinement with increasing the value of the swelling ratio s^*. For the same swelling ratio, the bigger is the degree of confinement, the smaller is the steady inclination angle. On the other side, tank–treading velocity increases almost linearly with respect to increasing of swelling ratio in the narrower channel, while in the wider domain the increasing of tank–treading velocity has slowed down until it arrives almost maximum around $s^* \sim 0.9$. The same qualitative tendency is given in [21, 30, 31, 29, 45, 4]. We also keep track of the area and the perimeter of the cell during the simulations. The variation is less than $\pm 0.1\%$ in the area and $\pm 0.5\%$ in the perimeter.

3.1.2 A go–and–stop experiment for the shape recovery

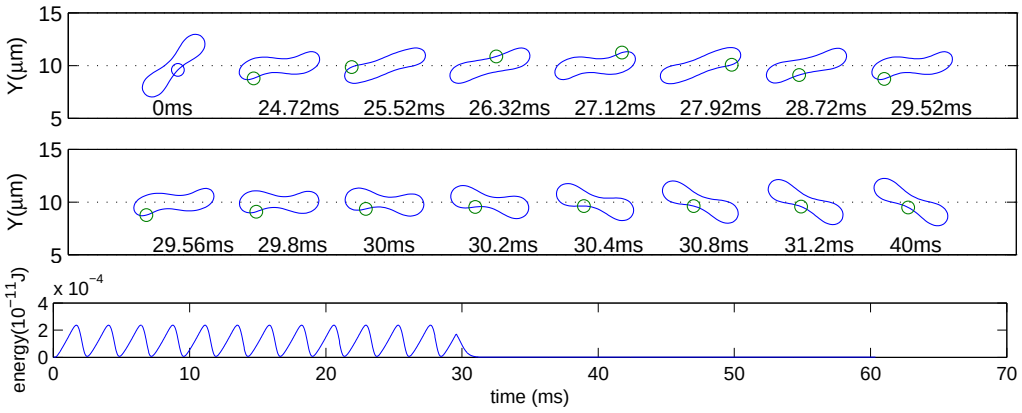

Figure 3.2: A go–and–stop experiment: the snapshots (top and middle) and history of energy (bottom) over the unit thickness of the cell in shear flow at $C_a = 6.365$. The moving walls are stopped at time 29.52 ms.

A red blood cell is said to have the shape memory if after stopping the flow, the deformed cell will go back to its initial shape with any part of the membrane regaining its original position, i.e., the rim always returns to the rim and the dimple is always back to the dimple. To show that the cell with a nonuniform natural state modeled by (2.6)–(2.9) does have the shape memory property, we have simulated several cases of the go–and–stop.

Figure 3.2 shows a cell with $\alpha = 1$ (fully non–uniform) of the swelling ratio $s^* = 0.481$ suspended in a simple shear flow at the capillary number $C_a = 6.365$ in a channel of the length 80μm and width 20μm. The top and bottom walls of the channel are driven at the same speed in opposite directions as shown in Figure 2.1a. The cell is at its reference shape at time $t = 0$ s, with a membrane particle at the dimple marked by a small "o". At the beginning, the cell performs a swinging motion and the marked position tank–treads along the membrane as in Figure 3.2 (top). We then suddenly stop the motion of two walls by

setting the boundary conditions on them equal to zero, and observe (in Figure 3.2 (middle)) that the cell first returns to the biconcave shape very quickly and then the marked position tank–treads back to its initial location on the membrane, this behavior is first observed in experiments by T. M. Fischer in [22]. The cell energy, plotted in Figure 3.2 (bottom), is minimized when the cell is at its natural state. During the swinging motion, the cell energy changes periodically with the period equal to the half of the period of oscillation due to the symmetry of the cell natural state. After stopping the motion of two walls, the cell energy returns to the one at its natural state.

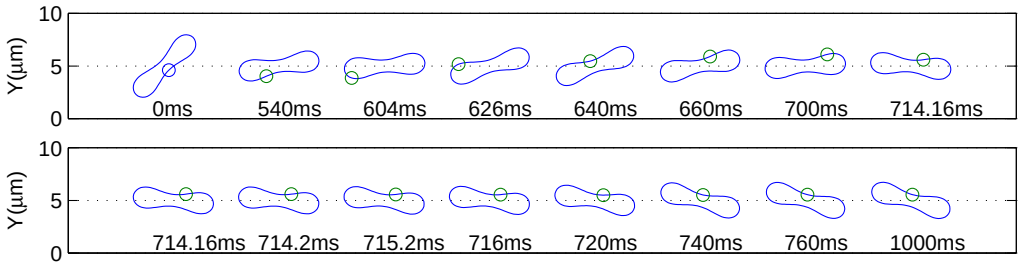

Figure 3.3: Snapshots of the cell in shear flow with $C_a = 0.182$ in narrower channel. At time $t = 714.16$ ms, the motion of two walls is stopped.

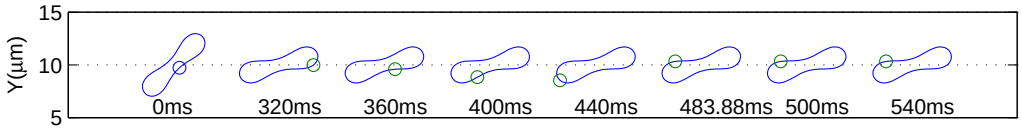

Figure 3.4: Snapshots of the cell in shear flow with $C_a = 0.091$ in a wide channel. At time $t = 483.88$ ms, the motion of two walls is stopped.

At lower α values, we get the same rim to rim, dimple to dimple behavior after the walls stopped moving, as shown in Figure 3.3 which gives an example with $\alpha = 0.05$. But when $\alpha = 0$ (Figure 3.4), the tank–treading motion stops right after the wall motion stops, the

membrane particle from dimple does not go back to the dimple. This suggests that to have the shape memory for the membrane in two–dimensional flow, we need the coefficient α to be nonzero, and with larger α value, we get stronger memory of the reference shape in the sense that membrane tank–treads back to the reference shape faster. But the intermittency has always been there for the small values of $\alpha > 0$ as discussed in Section 3.4.1.

3.2 Three types of the cell motion in shear flow

We have first considered a cell with a fully non–uniform natural state ($\alpha = 1$) suspended in shear flow at the capillary numbers $C_a = 0.455$, 9.093, and 90.934 in a channel of the length 80μm and width 20μm (called a wider channel). These three capillary numbers give rise to three typical motions of the cell, namely, (i) a tumbling motion, (ii) a swinging, and (iii) a tank–treading motion, respectively. The inclination angle θ and the phase angle ϕ defined in Figure 2.1b and Figure 2.1c, respectively, are used to described the cell motion. Since the shape of cell in shear flow is symmetric about its mass center and so is the reference angles in the bending energy E_b, we can restrict the range of both inclination and phase angles to $[-90^\circ, 90^\circ]$. If the inclination angle has the local maxima and minima within $(-90^\circ, 90^\circ)$, the cell is doing a swinging; otherwise if the inclination angle decreases monotonously to -90° then jump to 90°, it is a tumbling motion. The criteria for the phase angle are the opposite. When the local maxima and minima of the phase angle are in $(-90^\circ, 90^\circ)$, the cell has the tumbling motion. If the phase angle increases monotonously to 90° and then jumps to -90°, it means that the cell is swinging (and tank–treading).

At the capillary number $C_a = 90.934$, the cell is elongated to an elliptical shape and performs a tank–treading motion with about the same shape and inclination angle. When reducing the capillary number to 9.093, a swinging motion of the cell with the membrane

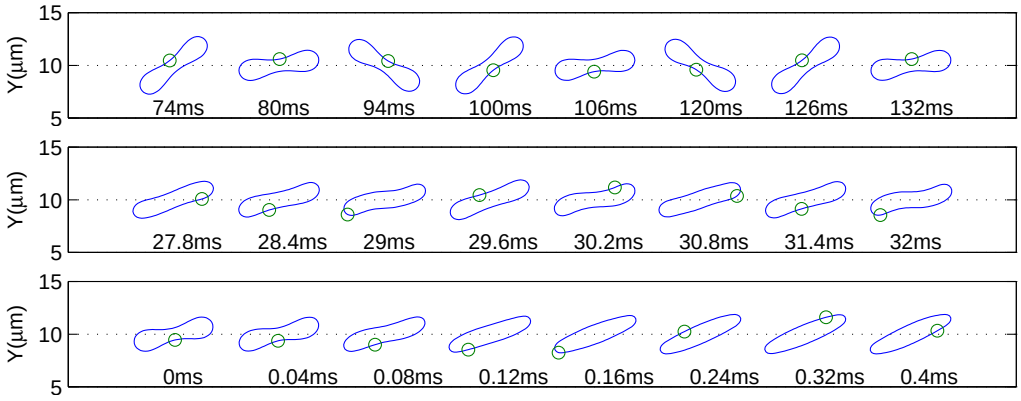

Figure 3.5: Snapshots of the cell shape and orientation at the capillary number C_a= 0.455 (top), 9.093 (middle), and 90.934 (bottom) illustrate the tumbling, swinging, and tank–treading motions, respectively.

tank–treading and the inclination angle oscillating is obtained. The shape of the cell is deformed periodically. And finally, the cell keeps tumbling periodically at the capillary number $C_a = 0.455$. These motions are illustrated by the snapshots and histories of the inclination and phase angles of the cell in Figures 3.5 and 3.6. During the tank–treading motion and swinging, the cell keeps changing its shape periodically with respect to the period of tank–treading. When tumbling at the capillary number close to the threshold for the transition to the intermittent behavior, the cell also keeps changing its shape periodically with respect to the tumbling period. Those shape deformations come from the fact that during these motions the membrane tends to reduce the difference between the current bending angle θ_i and the reference angle θ_i^0 to minimize the elastic energy. The swinging motion obtained in this paper is always coupled with the tank–treading motion. The purely tank–treading motion is actually a special case of swinging where the oscillation of inclination angle is so small and can be neglected (see Figure 3.6).

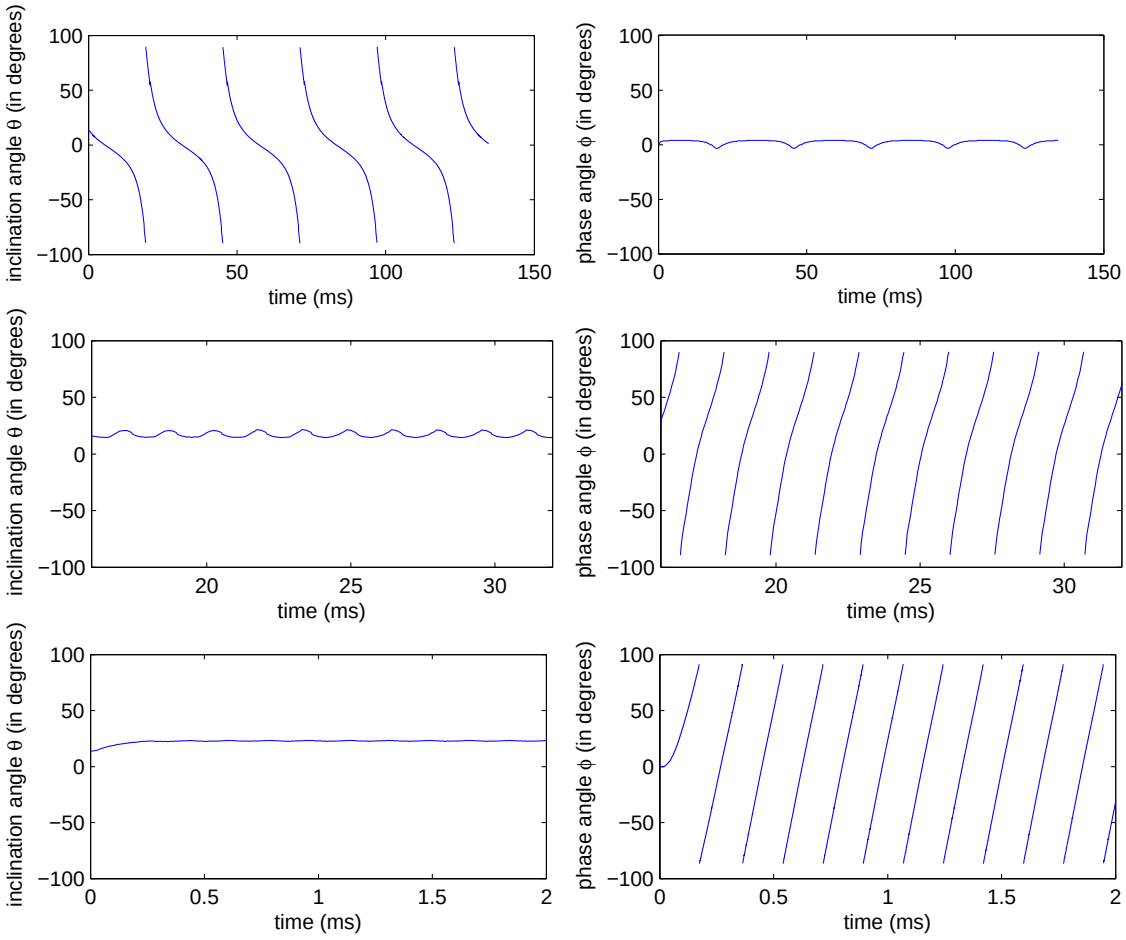

Figure 3.6: Histories of the inclination angle (left) and the phase angle (right) at the capillary number Ca= 0.455 (top), 9.093 (middle), and 90.934 (bottom) associated with the tumbling, swinging, and tank–treading motions, respectively.

To demonstrate that the effect of the bending term E_b given in equations (2.6) and (2.7) is also a key factor (besides the viscosity ratio) on the cell motion in shear flow, we have presented in Figure 3.7 that the cell of the swelling ratio $s^* = 0.481$ at different shape memory coefficient α undergoes either tank–treading motion or tumbling at a shear rate 500 s^{-1} in a channel of the length 80μm and width 10μm (called a narrow channel). As the effect of the nonuniform natural state is weaker, the cell just tank-treads; but under stronger effect, the cell does tumble as shown in Figure 3.7. We have also obtained that, for all choices of capillary numbers, the capsule with the uniform natural state undergoes tank–treading motion, which is same as in [60].

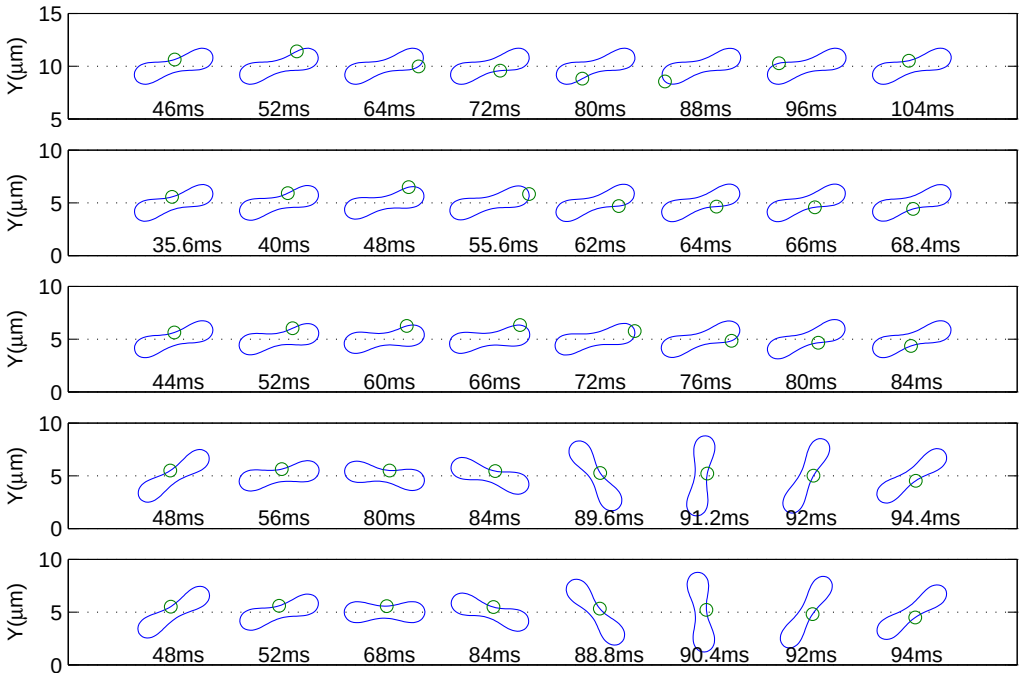

Figure 3.7: Snapshots of the capsule motion of $s^* = 0.481$ with different nonuniform natural states at α=0, 0.05, 0.1, 0.5 and 1 (from top to bottom), respectively, and C_a= 0.455. The motion is TT at α=0, 0.05 and 0.1 and tumbling at α=0.5 and 1.

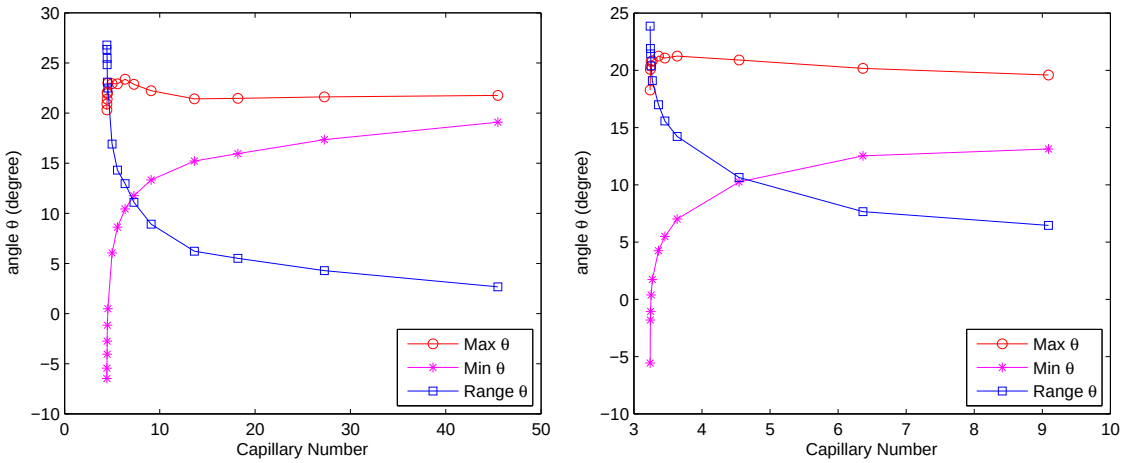

Figure 3.8: Inclination angles in wider channel (left) and narrower channel (right) with respect to capillary numbers.

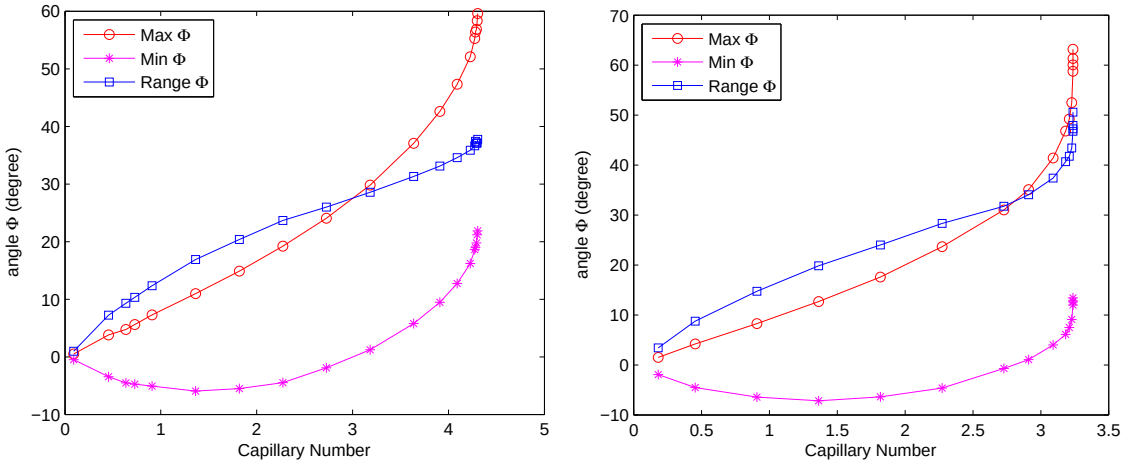

Figure 3.9: Phase angles in wider channel (left) and narrower channel (right) with respect to capillary numbers.

The inclination and phase angles do behave as expected. Figures 3.8 and 3.9, as an example, illustrate the angles with respect to the capillary numbers for the case $\alpha = 1$. While the cell swings, the range of inclination angle decreases as the capillary number is increasing. Also a larger confinement ratio results in the speeding up of the rate of decreasing. On the other hand, the range of phase angle increases with the increasing of capillary number while the cell tumbles, but it does not show much dependence on the confinement ratio.

3.3 The swinging motion

The cell deformation appears to be stronger when the effect of shape memory is strong. At lower values of α, the cell can hardly be deformed at low and moderate capillary numbers. Figures 3.10 shows the swing of the cell with different values of α. Based on the

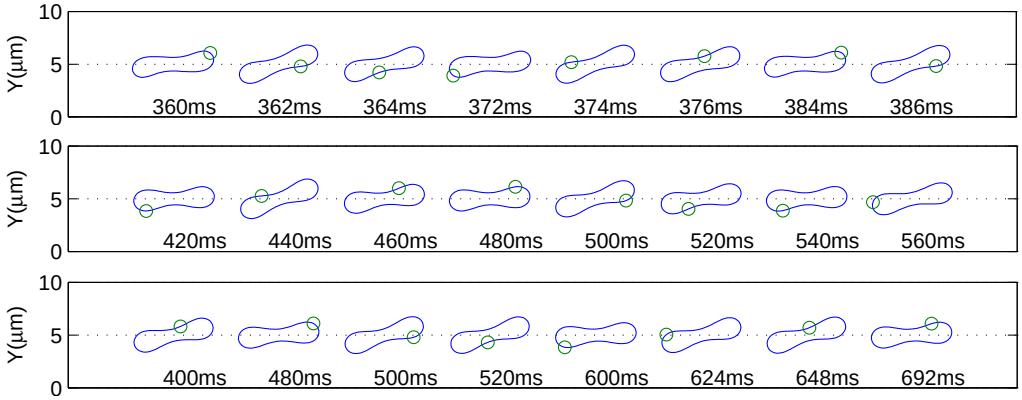

Figure 3.10: Snapshots of cell swinging motion in a narrower channel 80μm $\times$ 20μm with the following shape memory coefficients and capillary numbers: (top) $\alpha = 0.5$, $C_a = 1.818$; (middle) $\alpha = 0.1$, $C_a = 0.364$; (bottom) $\alpha = 0.05$, $C_a = 0.182$.

experimental results by Abkarian *et al.* [1], a RBC does not change its shape very much during swinging motion, which gives us a hint that the effect of shape memory should be relatively small .

Figures 3.11 and 3.12 together show a swinging motion, where cell swings upwards then downwards, and return to the same shape and inclination angle as the beginning of the cycle (but phase angle has a shift of 180 degrees). One quick observation is that swinging downwards takes much more effort than swinging upwards. The main reason is the following. When swinging upwards, the membrane just finished the jump in the phase angle ϕ, i.e., the membrane particle located the dimple has just passed through the rim and is now on the way back to the dimple; therefore the elastic force is helping the cell tank-treading along the membrane and shortens the time for dimple particle travelling from rim back to dimple. On the other hand, when the inclination angle θ is at its local maximum, the cell is about to swing downwards and the dimple particle has just passed through dimple and is tank-treading to the rim; the elastic force is working against the force from flow which makes the cell tank-treading by moving the dimple particle back and then slow down the tank-treading motion. With the classical KS model[30] which does not assume a shape memory effect, the cell is predicted to have a fixed inclination angle for a given flow rate. In [57], the analytical model proposed by Skotheim and Secomb considering the elastic energy (which corresponds to the shape memory effect) does suggest such periodic change in inclination angle.

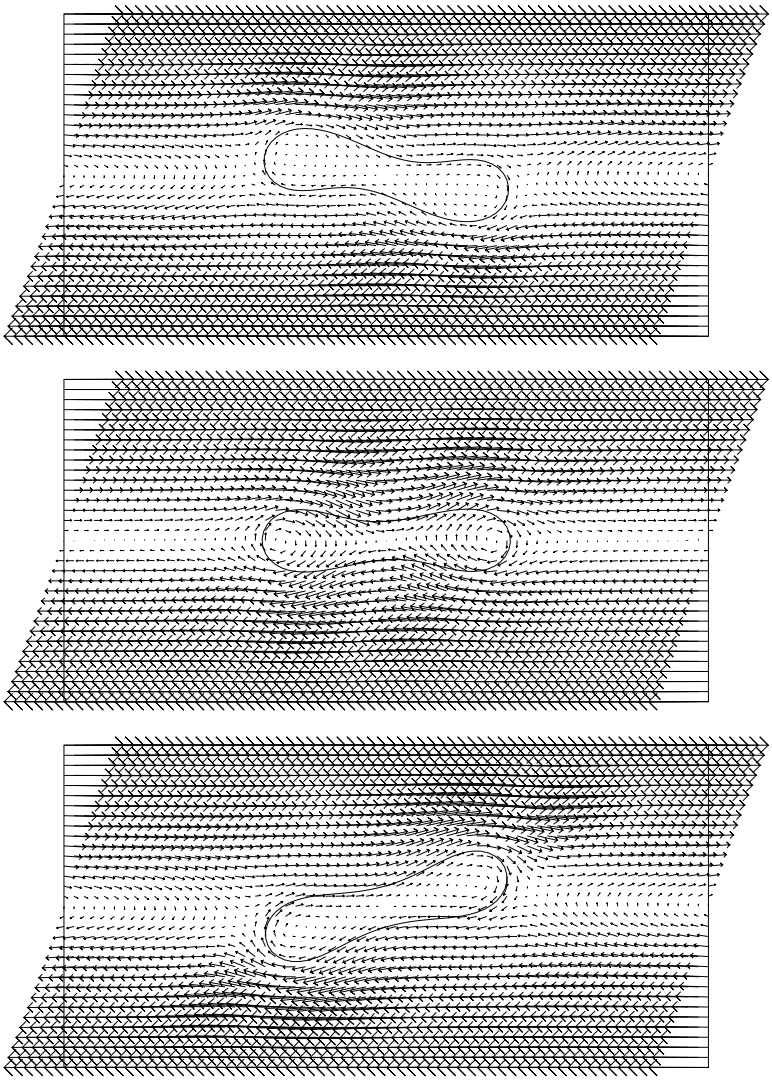

Figure 3.11: Velocity fields of cell swinging from lowest position to highest position: at time t=1.739s (top) inclination angle θ is at local min; at time t=1.752s (middle) cell is swinging upwards, θ is increasing; at time t=1.766s (bottom) cell is θ is at local max.

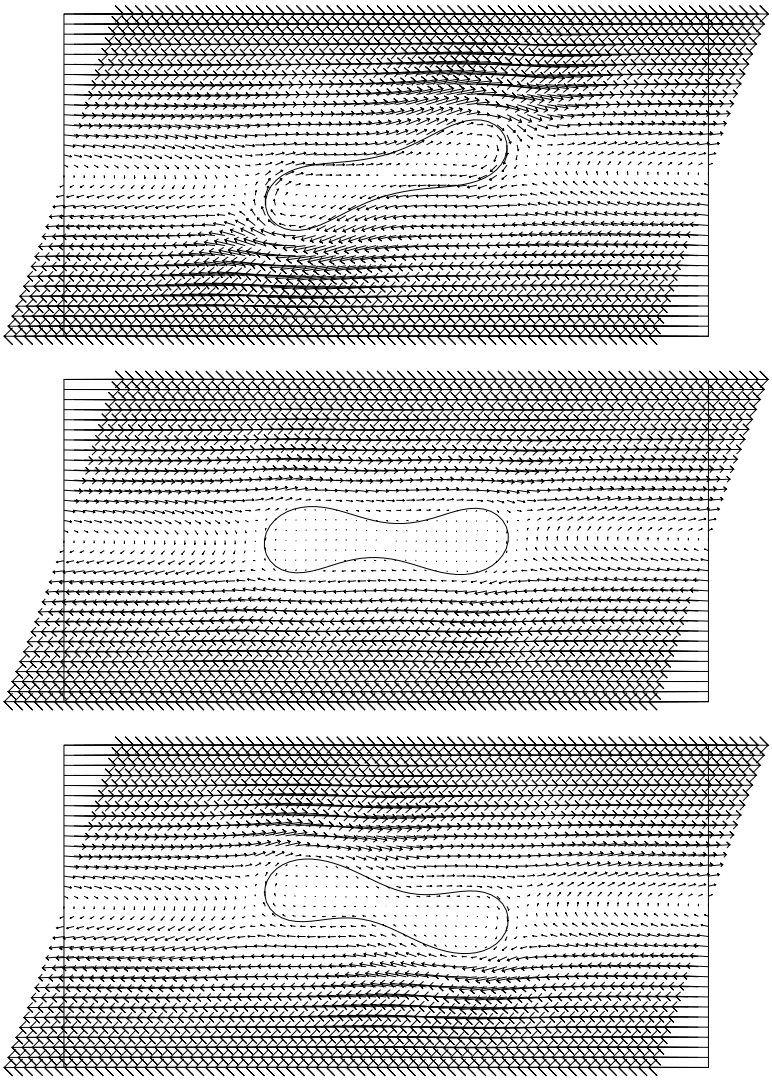

Figure 3.12: Velocity fields of cell swinging from highest position to lowest position: at time t=1.766s (top) inclination angle θ is at local max; at time t=1.850s (middle) cell is swinging downwards, θ is increasing; at time t=1.930s (bottom) cell is θ is at local min.

3.4 The intermittent behavior

When the capillary number is in the right range, the intermittent behavior of cell motion has been predicted by a reduced model proposed by Skotheim and Secomb [57]. In this section, our computational results show that the bending energy E_b in equation (2.6) proposed by Tsubota et al. [60] or the one in (2.7) does play a role like the elastic energy term introduced by Skotheim and Secomb in [57] and give rise to the intermittent behavior of the cell. Here is a typical intermittent behavior: at the capillary number $C_a = 4.410$, with $\alpha = 1$, the cell performs one tumbling and one tank–treading in each cycle in a wider channel of dimensions 80μm $\times 20\mu$m. Figure 3.13 shows the snapshots of the cell motion in one cycle as well as the histories of the inclination angle, the phase angle and the cell energy. Since the cell performs one tumbling and one tank–treading in each cycle, both angles show jumps in the middle two of Figure 3.13. The energy required for the tumbling in each cycle appears to be higher than that for the swinging, because when the cell swings, it has an elongated shape which is much closer to the original biconcave shape than those shapes when the cell tumbles.

Here we only show details for the case $\alpha = 1$, where the cell has a relatively strong memory so that the intermittency range is larger than those with the weak memory coefficients. Actually, according to our simulations shown in Section 3.4.1, the value of α only effects the critical Capillary number where intermittent behavior occurs and the range of intermittency. As shown in Figure 3.14a, the cell performs tumbling motion in a wider channel when the capillary number C_a is less than a critical value of 4.274 and swinging motion for C_a greater than 4.456. Intermittency occurs if C_a is in $(4.274, 4.456)$. The embedded sub–figure in Figure 3.14a corresponds to the contrast ratio between the number of the tumbling (TB) and the number of the swinging with tank–treading (TT) in one cycle

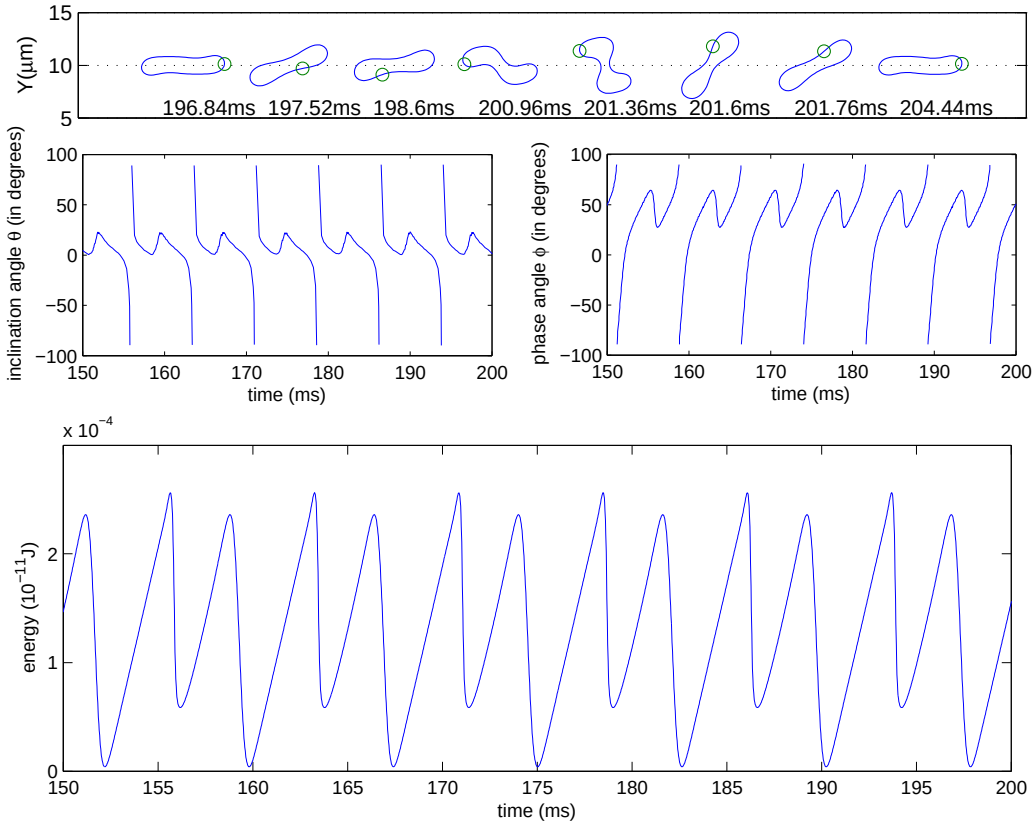

Figure 3.13: Snapshots of the cell shape and orientation in one cycle (top), histories of the inclination angle (middle left), the phase angle (middle right), and the energy over the unit thickness (bottom) of the cell at Ca= 4.410.

of cell motion at the intermittent state. When the capillary number is very close to and below the threshold for the transition to the swinging motion, the cell tumbles once after a series of swinging in one cycle. The number of swinging in each cycle decreases with respect to the decreasing of the capillary number, until the cell tumbles once and swings once alternatively. This should be a relatively stable mode in the intermittent regime since we observed it happens over a range of the capillary number. Then the cell performs more tumbling between each swinging when we keep reducing the capillary number, until the capillary number passes through the threshold for the transition between the tumbling and the intermittent behavior, and the cell just tumbles.

In a narrower channel of dimensions 80μm $\times 10\mu$m, the cell enters the intermittent state at a critical capillary number 3.237, and performs pure swinging for the capillary number $C_a > 3.242$, which gives a smaller range of the capillary number for the intermittency (see Figure 3.14b). The embedded sub–figure in Figure 3.14b also show the cell behaves similarly at the intermittent state in a narrower channel.

An interesting observation is that the period has a sharp raise when the cell motion is close to the intermittent state as in Figure 3.14c. For the capillary number right above the intermittent range, one of the explanations is that while the cell changes its shape, the membrane particle leaves its natural–state position during the tumbling motion. But the force caused by the bending energy is tending to pull the membrane back to its original natural state, which obviously is against the viscous force of flow which would like to push the membrane particles moving along the membrane. Hence when the capillary number is right above the intermittent range, the tank–treading motion is slower since the contrast between these two forces is not significant. For the capillary number right below the intermittent range, the cell just tumbles and has a shape of long body. In the non-Stokes

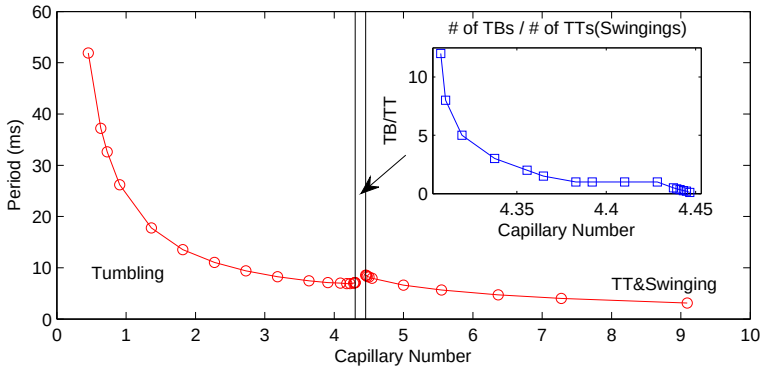

(a)

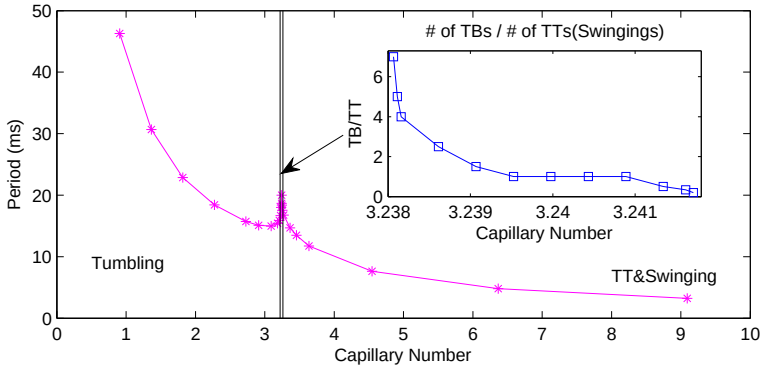

(b)

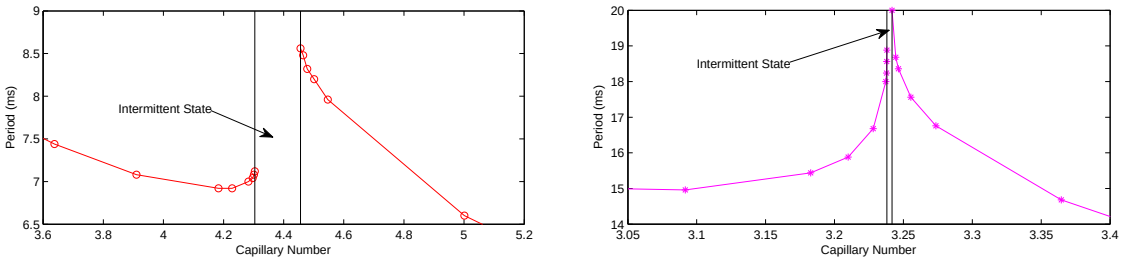

(c)

Figure 3.14: Histories of period of tumbling and tank–treading of the cell of $s^* = 0.481$ in (a) a wider channel, (b) a narrower channel and (c) the enlargement of the intermittent region of Fig. (a) (left) and Fig. (b) (right).

flow regime, a neutrally buoyant rigid particle of elliptic shape in shear flow has a transition from the tumbling motion to the state with a fixed inclination angle (i.e., no rotation at all). As the shear rate increases, the circulation before and after the long body becomes stronger and then can hold the long body with a fixed inclination angle (see, e.g., [15, 8]). But in Stokes flow regime, the long body just keeps rotating in shear flow. In this paper, the cell of a long body shape suspended in shear flow is actually a neutrally buoyant entity. Similarly the cell slows down its rotation when the capillary number is less than and closer to the threshold for the transition to the intermittent behavior. Figure 3.15 shows the circulation of the velocity filed before and after the cell and the history of the inclination angle of the cell in a wider channel at Ca= 4.274 in which the cell rotation slows down at the inclination angle around 5° degrees. Thus the period of tumbling increases as the capillary number increases since the strength of the flow field circulation before and after the cell is increased.

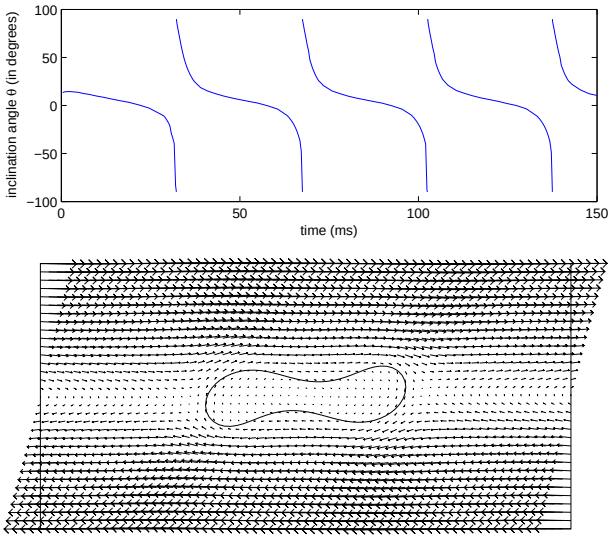

Figure 3.15: History of the inclination angle (top) and a velocity filed snapshot (bottom) of the cell in a wider channel at Ca= 4.274.

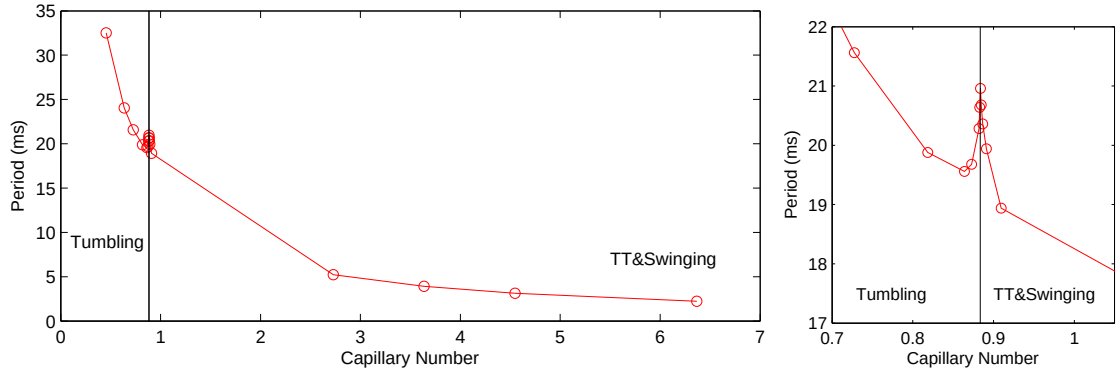

(a)

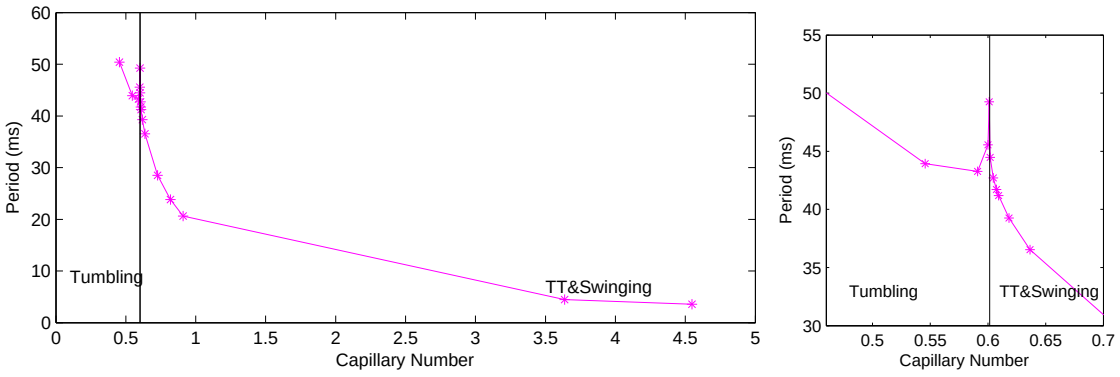

(b)

Figure 3.16: Histories of period of tumbling and tank–treading of the cell of $s^* = 0.9$ (left) and the enlargement of the intermittent region (right) in (a) a wider channel and (b) a narrower channel.

For the effect of the swelling ratio, we have tested the values of $s^* = 0.6$, 0.7, 0.8 and 0.9 and obtained that for the cell of swelling ratio greater than 0.6, it is almost impossible to capture the intermittent behavior since the range of the capillary number for such behavior is about zero if it exists. In Figure 3.16, results similar to those in Figure 3.14 are shown for the case of the cell of the swelling ratio $s^* = 0.9$, whose shape is about an elliptical

shape. The cell of the swelling ratio s^* can be characterized by its excess circumference $\triangle c = 2\pi(\frac{1}{\sqrt{s^*}} - 1)$. For the biconcave shape of $s^* = 0.481$, its $\triangle c$ is 2.77638; but the one for an elliptical shape of $s^* = 0.9$ is 0.33987. The excess circumference $\triangle c$ is similar to the excess area used in [66]. For the small values of $\triangle c$, we do not expect to obtain the intermittency. Our result is consistent with the results obtained by Tsubota *et al.* in [60] since the cell used in their simulations has the swelling ratio of 0.7.

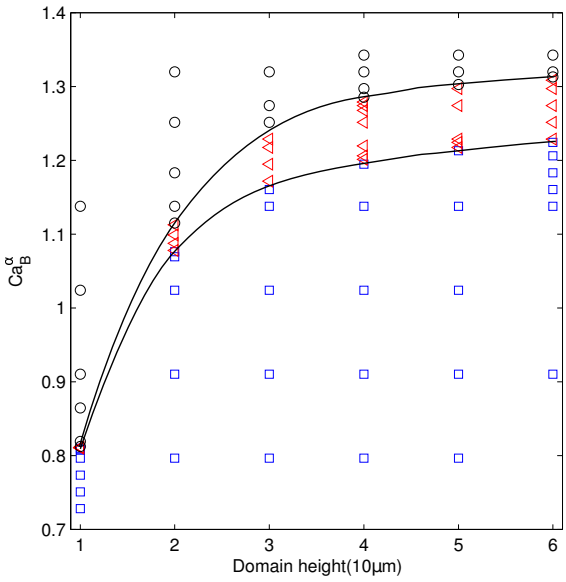

Figure 3.17: The effect of the confinement ratio to the motion transition and intermittent state.

Finally, the effect of confinement ratio is studied by fixing $\alpha = 1$, domain length $L = 80$ μm, and varying the height W between 10 μm and 60 μm. In Figure 3.17, blue squares stands for pure tumbling motion, black circle for pure tank–treading, and red triangle for intermittent states. It is not surprised that in a wider channel, the range of the bending capillary number Ca_B in which the cell performs pure tumbling is higher, and the range for having the intermittent state is wider. The intermittent state converges to a

fixed range of Ca_B as the wall effect converges to almost zero when increasing the channel width.

3.4.1 The effect of the shape memory coefficient

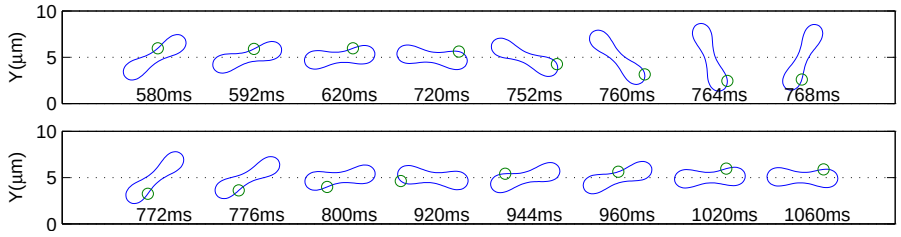

Figure 3.18: Snapshots of a tank–treading motion of a single cell with $\alpha = 0.05$ at the intermittent state in shear flow with the capillary number 0.163.

As mentioned in the previous subsection, with lower values of α, the cell does not tend to change shape as much as cell with $\alpha = 1$. Even in intermittent state, it prefers keeping the biconcave shape (see Figure 3.18 for an example). Figure 3.19 shows that the critical value of the capillary number for the transition from tumbling to intermittent state is proportional to the value of α, this can be explained by defining a weighted bending capillary number with respect to α: $\mathrm{Ca}_B^\alpha = \mu R_0^3 \dot{\gamma}/(\alpha k_B l_0)$ which is similar to the bending capillary number defined by Tsubota et al. in [60]. This number represents the relative effect of fluid viscous force versus surface tension which comes from the memory of the reference angles $\{\theta_i^0\}$, and therefore a scale of α should be added. The cell has tumbling motion when the viscous force from outer fluid is less than the force pulling it back to initial position, and swinging motion with tank–treading when the viscous force is larger. Intermittency occurs when $\mathrm{Ca}_B^\alpha \sim k$, where k depends on swelling ratio and degree of confinement, etc. This implies that $\dot{\gamma} \sim \alpha k_B l_0/(\mu R_0^3)$, i.e. the capillary number of the

intermittency is proportional to the value of α (because the capillary number is proportional to the shear rate). The range of the capillary number for the intermittent behavior is increasing as α increases. When α is small, the rate of increasing is almost linear. But as α raising up, this rate slows down as the cell becomes more deformable and can change shape accordingly to achieve periodic tumbling or swinging, which is more preferred because the energy change is more stable than in intermittent states.

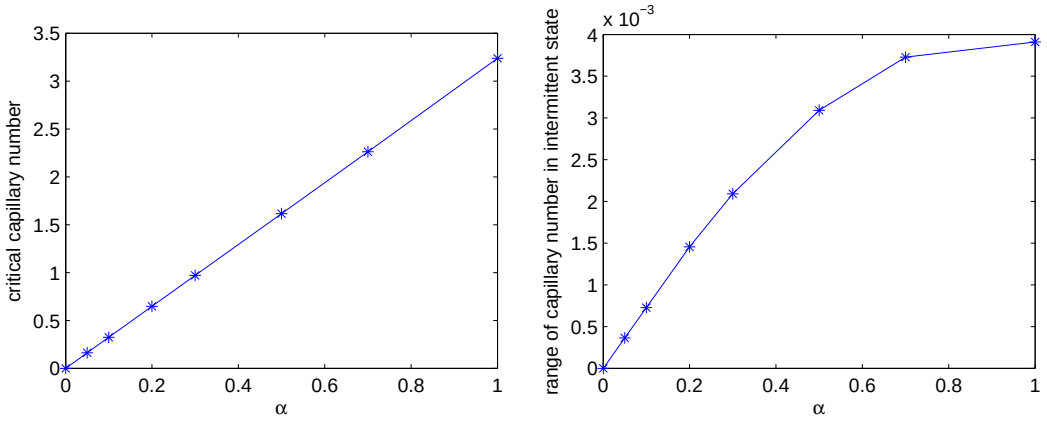

Figure 3.19: The intermittent state versus the shape memory coefficient α: the plot of the critical value of the capillary number for the transition from tumbling to intermittent state (left) and the range of the capillary number for having the intermittent state (right).

The behavior of the intermittent state in a narrow channel with respect to the weighted–bending–capillary number Ca_B^α is plotted in Figure 3.20, where the y-axis interprets the number of tank–treading over the number of tumbling in each cycle, and x-axis is the difference between $1/Ca_B^\alpha$ and its value at the boundary of pure tank–treading regime and intermittency. In the "more tank–treading than tumbling per cycle" regime, the tendency is almost linear with the slope of -0.45 until slope becomes a little sharper when close to the "one tank–treading and one tumbling alternatively" regime, which is consistent with

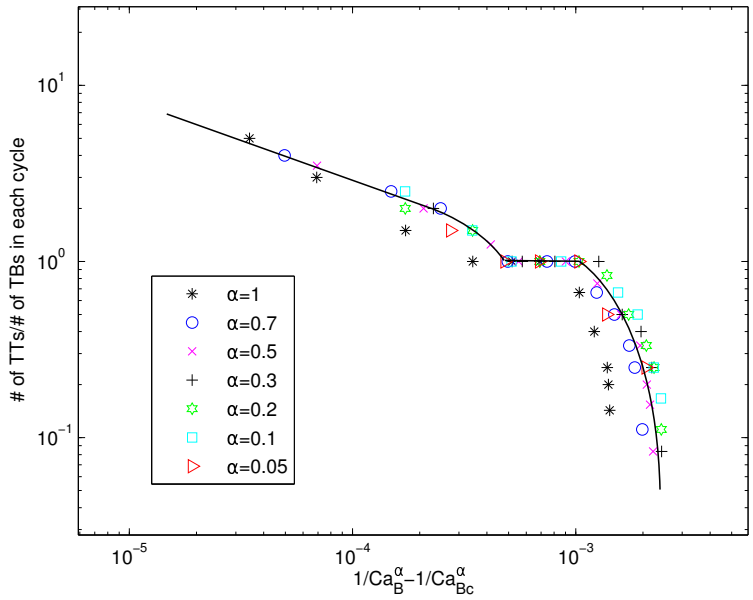

Figure 3.20: The intermittent state with effect of shape memory α varies from 0.05 to 1, in a narrower channel.

the results obtained by Skotheim and Secomb in [57].

One major observation through Figure 3.20 is that the "one tumbling and one tank–treading alternatively" regime is not eliminated when reducing the effect of shape memory, even with α values as small as 0.05, where the cell is only little deformable, this suggests this is a relative stable state in the intermittent regime. To understand this issue more, we have plotted in Figure 3.21 two examples of intermittent state with one tumbling and one tank–treading per cycle in a narrow channel with the weighted bending capillary numbers $Ca_B^\alpha = 0.8137$ and 0.8140 for $\alpha = 0.05$. With these given conditions, the shape of the cell can maintain almost a biconcave shape, which is for the convenience of the following discussion. In each cycle, after the tumbling (the middle one among the nine different

orientations shown in each subplot in Figure 3.21), the cell tends to return to its natural state (i.e., dimple back to dimple). But the flow viscous force prevents the cell from the

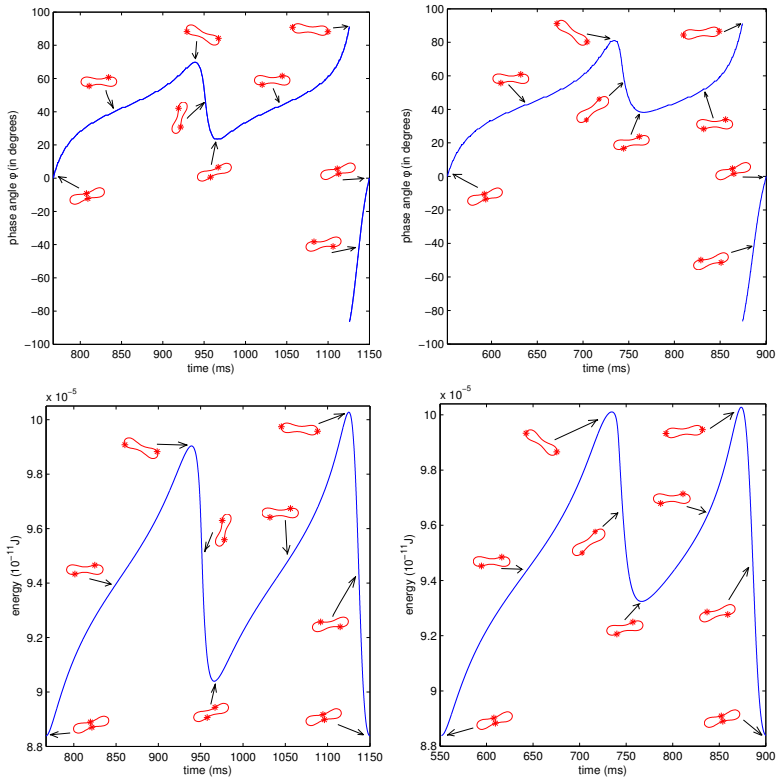

Figure 3.21: Two examples of intermittent state with one tumbling and one tank–treading per cycle: the histories of the phase angle (top) and the energy over the unit thickness (bottom) of the cases $Ca_B^{\alpha} = 0.8137$ (left) and $Ca_B^{\alpha} = 0.8140$ (right) in a narrower channel.

complete recovery, thus the phase angle is not back to zero degree after the tumbling. With the larger Ca_B^{α} value, the phase angle after the tumbling motion is larger and then the associated maximal energy is much closer to the needed energy for having tank–treading motion. When the cell starts to tank-tread with a higher starting phase angle, it needs less effort from the flow to complete a tank–treading. After having a tank–treading motion,

there will be an instant at which the cell shape almost has its natural state. But if the angular speed at this instance is not fast enough, the cell may not be able to achieve another tank–treading and a new "one tumbling one tank–treading" cycle shall start.

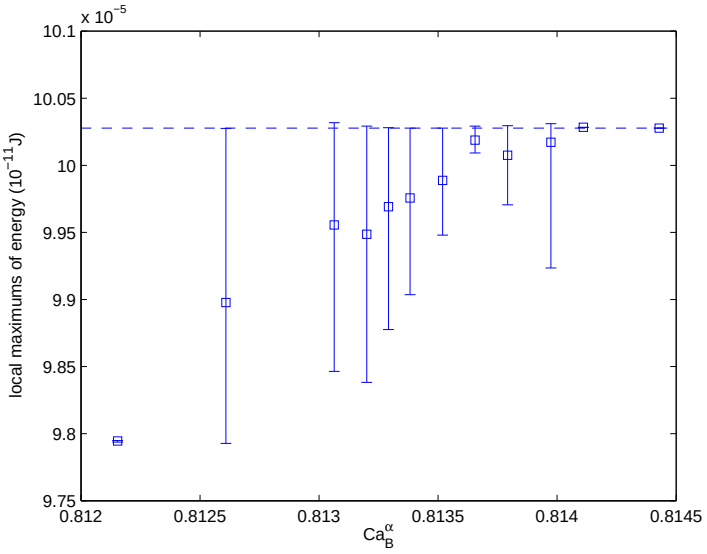

Figure 3.22: The peaks of energy over several periods around intermittent state with $\alpha = 0.05$, in a narrower channel. The erroe bars represent the range of the peak values.

Figure 3.22 shows an example of energy peaks around the intermittent state with respect to Ca_B^α, with $\alpha = 0.05$ in a narrow channel. The dash line is the energy barrier where the cell has the initial biconcave shape but its phase angle is shifted by 90 degrees since such conditions can be interpreted as the barrier about whether the cell can perform tank–treading motion. The very left one in the Figure 3.22 is associated with the pure tumbling case and the very right two are associated with the pure swinging cases, others are associated with the intermittent state. It is safe to assume these energy peaks occur when the phase angle is at its local maximum, which determines either the cell is performing tumbling motion (local maximum of the phase angle is less than 90 degrees) or

tank–treading motion (local maximum of the phase angle reaches 90 degrees) around that peak. We can see that during the transition from pure tumbling to pure tank–treading, the average of the peaks is almost increasing with respect to the increasing of Ca_B^{α}, and the maximum value of the peaks reaches the dash line if at least one tank–treading is performed in each cycle. On the other hand, the minimum value of the peaks will below the dash line if at least one tumbling is performed. There are two cases where the average energies are higher than expected compare to the other cases, one with several tumbling during each tank–treading and another with several tank–treading during each tumbling, this might also suggest that these two modes are relatively unstable than the "one tumbling and one tank–treading alternatively" mode.

3.5 Cell motions in Poiseuille flow

In Poiseuille flow, cells can also perform tumbling, swinging (also called breathing), and tank-treading, but the swinging is not necessarily coupled with tank-treading. Cell shape may be deformed into a slipper or a parachute, therefore, it makes no sense to look at the inclination angle which is determined by the long axis of cell shape as long axis is only defined when the shape is symmetric about its mass center. In this case, we focus on the orientation angle η (it shares the same symbol as inclination angle in shear flow) which is formed by the line connecting the mass center of cell and a some fixed position on the membrane. A series of smooth monotonic changing of η between -180° and 180° combined with a jump would indicate that cell has tumbling motion, otherwise swinging motion, with or without tank-treading. For example, (see Figure 3.23), in wider channel ($\Omega = 80\mu m \times 20\mu m$) where wall effect is very small, with fully non-uniform natural state ($\alpha = 1$) at which cell behaves similarly to a neutrally buoyant rigid particle. Cell performs

tumbling motion after a series of swingings for all values of capillary number, and does not stay in the middle of the channel.

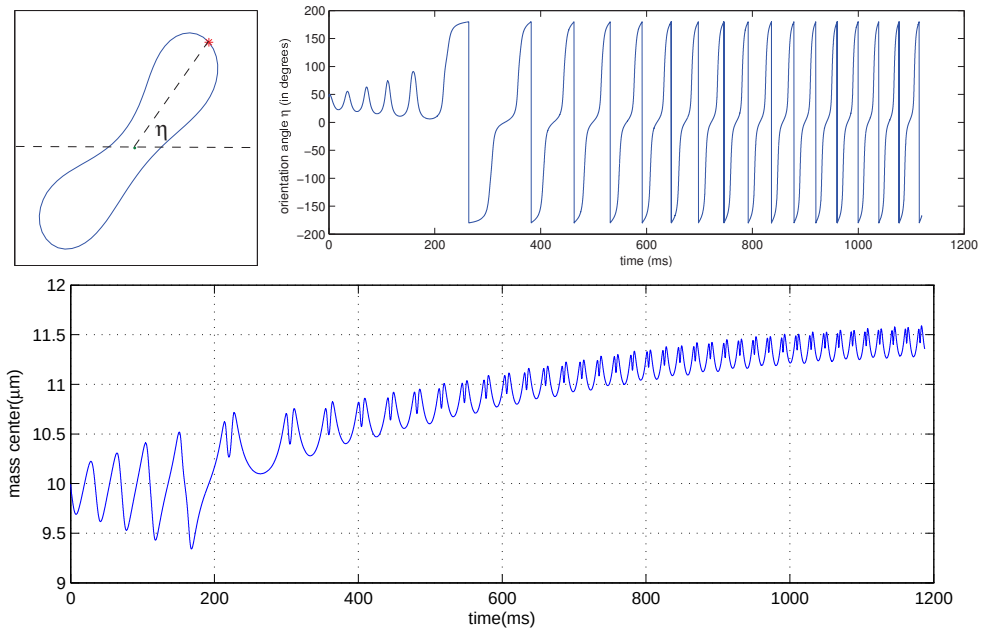

Figure 3.23: Schematic diagram of how to determine orientation angle η (top left), history of η (top right) and history of mass center (bottom) for cell in wider channel with $C_a = 9.093$, $\alpha = 1$.

First, to illustrate the effect of α, we have fixed the domain to be a narrow channel, $\Omega = 80\mu m \times 10\mu m$, the max velocity $u_{max} = 2.5$ cm/s, which yields $C_a = 9.093$. At α as low as 0.05, as shown in Figure 3.24, the equilibrium state of cell is a breathing slipper with tank-treading. The bottom two figures shows one cycle of breathing of the cell. Here the small circle denotes the same membrane particle, which indicates that the cell membrane is tank-treading clockwise in addition to breathing.

If α value is raised to 0.1, with the same flow speed, the cell exhibits more complicated motion than the one with lower α values. In Figure 3.25, the small circle in the

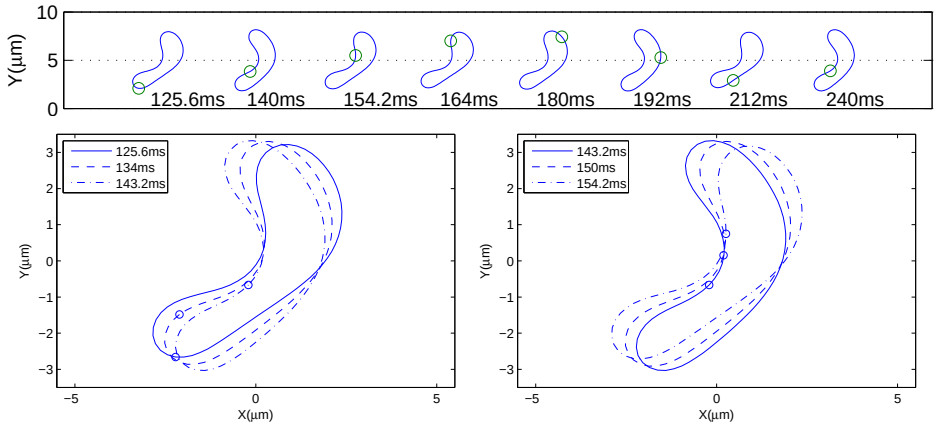

Figure 3.24: Snapshots tank-treading motion with breathing of a cell in Poiseuille flow at $C_a = 9.093$ and $\alpha = 0.05$.

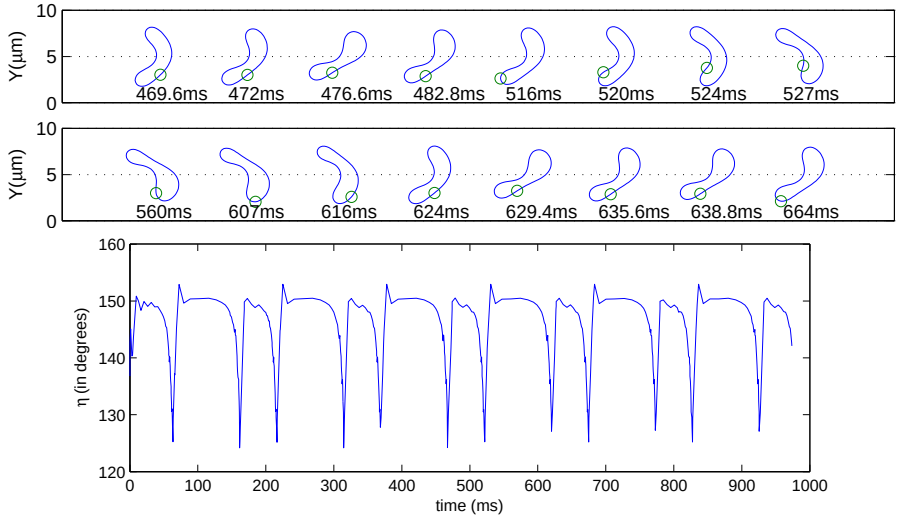

Figure 3.25: Snapshots (top and middle) and history of angle η (bottom) for the cell motion in Poiseuille flow at C_a=9.093 and $\alpha = 0.1$.

snapshots denotes a fixed membrane particle which was in the dimple at stress-free state, at t=469.6ms, as the dimple particle is travelling to the rim by flow viscous force, the cell is performing tank-treading motion in slippery shape. the cell is rotation clockwise, with orientation angle decreasing, until the dimple particle has passed the rim and start heading back to dimple, the orientation angle then starts to increase. The cell get to a parachute-like shape as tank-treading goes on. As η keeps increasing, the cell has achieved half tumbling, but could not continue because the fluid viscous force (which is greater than cell elastic force as dimple particle get closer dimple) is pushing cell to tank-tread in the other direction, then the reverse of the above half cycle happens. At this value of α, a cell can perform neither pure tumbling nor pure tank-treading motion.

Continue increase the value to $\alpha = 0.5$, with the same flow speed, the cell first swings several times and get to an equilibrium shape without tank–treading (see Figure 3.26).

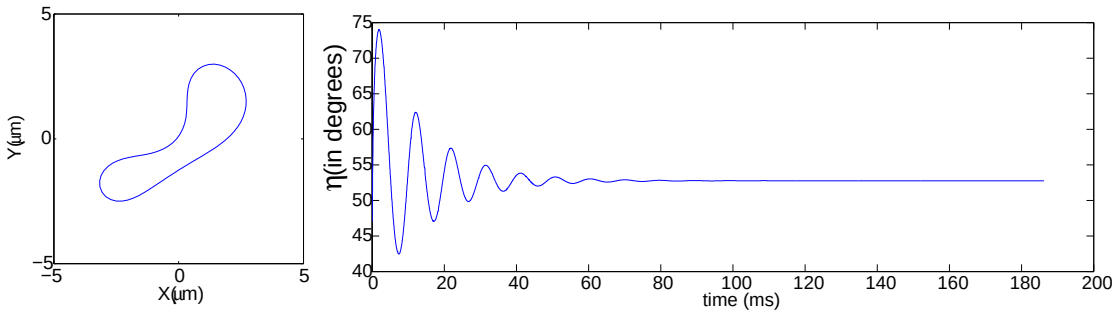

Figure 3.26: Equilibrium shape (left) and history of the orientation angle η (right) for the cell motion in Poiseuille flow at C_a=9.093 and $\alpha = 0.5$.

With fully non-uniform natural state ($\alpha = 1$), with the same flow speed, cell behave similarly as $\alpha = 0.5$, which will not be plotted here.

As mentioned at the beginning of this section, cell can exhibit different shapes in

Poiseuille flow depending on the Capillary number, and value of α. As shown in Figure 3.27, cell gets to a slippery shape with a smaller C_a number, and becomes more like a parachute when increasing the value of capillary number. For smaller α values, cell perform tank–treading motion while having slippery shape and breathing. The breathing and tank–treading behavior disappear when cell has a parachute equilibrium shape.

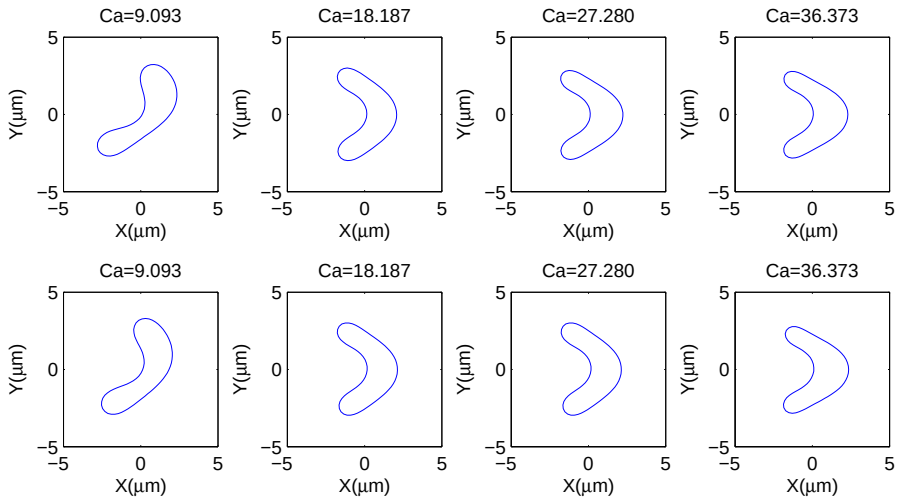

Figure 3.27: The equilibrium shape of cell in Poiseuille flow for $C_a = 9.093, 18.187, 27.280, 36.373$, from left to right, with $\alpha = 0$ and $\alpha = 0.05$. (for C_a=9.093, shape has small perturbations, see Figure 3.24)

If α value is larger (see Figure 3.28), cells do not tank–tread even with slippery shape, it gets to an equilibrium, unchanged shape in the Poiseuille flow at all tested Capillary numbers. And higher Capillary number is needed to give a parachute shape.

In Table 3.1 we have recorded the period of tank–treading in Poiseuille flow, varying the value of α and Capillary number C_a. Period increases when C_a number decreases or α value increases. In the special case $\alpha = 0.01$ and $C_a = 3.637$, cell keeps swinging without full tank-treading, this may cause from relatively week fluid viscous force comparing to the

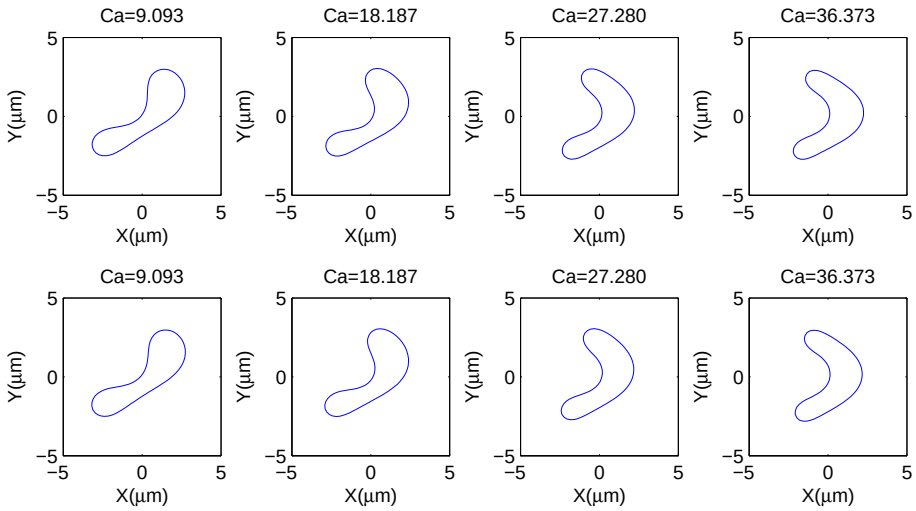

Figure 3.28: The equilibrium shapes for cells with $\alpha = 0.05$ (top) and $\alpha = 1$ (bottom) in Poiseuille flow.

elastic force to drive dimple membrane particle to the rim.

Table 3.1: Period of tank-treading in Poiseuille flow

	$\alpha = 0.05$	$\alpha = 0.01$	$\alpha = 0$
C_a=3.637	swinging without TT	187.82	170.81 ms
C_a=5.456	283.78 ms	81.98 ms	80.49 ms
C_a=7.275	62.16 ms	51.20 ms	50.84 ms
C_a=9.093	49.66 ms	41.50ms	41.30 ms

3.6 Conclusions

In this chapter, we have analysed the motion of a single cell with the shape memory suspended in two–dimensional shear flow and Poiseuille flow. We have studied the intermittency between tumbling and swinging in shear flow in a narrow range of the capillary number. When the capillary number is very close to and below the threshold for the swinging motion, the cell tumbles once after a series of swinging in each cycle. The number of swinging in one cycle decreases with respect to the decreasing of the capillary number, until cell tumbling once and swinging once alternatively. And then the cell performs more tumbling between each swinging when we keep reducing the capillary number, and finally shows pure tumbling. Surprisingly the "one tumbling and one tank–treading alternatively" mode is very persistent.

The critical value of the swelling ratio for having the intermittent behavior has been estimated. For those greater than 0.6 ($\triangle c$=1.82837), it is almost impossible to capture the intermittent behavior since the range of the capillary number for such behavior is about zero if it exists. For the small values of $\triangle c$ (associated with large swelling ratio s^*), we do not expect to obtain the intermittency.

An interesting observation is that the period has a sharp raise when the cell motion is close to the intermittent state. For the capillary number right above the intermittent range, the force caused by the bending energy is tending to pull the membrane back to its original natural state, which obviously is against the viscous force of flow which would like to push the membrane particles moving along the membrane. Hence when the capillary number is right above the intermittent range, the tank–treading motion is slower since the contrast between these two forces is not significant. For the capillary number right below the intermittent range, the cell is a neutrally buoyant entity and slows down its rotation

when the capillary number is less than and closer to the threshold for the transition to the intermittent behavior, which is closely related to the case of a neutrally buoyant particle in shear flow.

Another observation is that in the intermittent regime, the change of contrast between numbers of tumbling and tank–treading is not linear, especially when the weighted bending capillary number is close to or in the range of a relatively stable "one tumbling and one tank–treading per cycle" mode, we discussed this phenomenon may result from the deformability of RBC, even with shape memory coefficient α as small as 0.05, the cell may still have some invisible shape changes and is able to perform one tumbling one tank–treading in each cycle with a range of weighted bending capillary numbers.

On the other hand, we observe that as effect of shape memory increases, the cell becomes more rigid-body like, and show less fluidity of the membrane, i.e., the skeleton structure dominates cell behavior. If we keep reducing the shape memory coefficient α, membrane particles gets more freedom to travel around the membrane which indicates that the membrane becomes more fluid-like. Therefore, in our weighted bending energy, the first term corresponds to the uniform natural state and give the cell membrane fluidity, which, together with E_l and Γ_s, represents the property of the lipid bilayer, and the second term of the bending energy corresponds to the non-uniform natural state, i.e. give raise to a 2-dimensional simplified elastic energy, which may represent the shape memory property of the skeleton structure.

We have also simulated cell motions in Poiseuille flow with different capillary numbers, with lower α value, cell exhibit tank–treading motion with breathing in slower flow and get to a stationary parachute shape in faster flow; with higher α value, the tank–treading behavior in slower flow disappears, the cell shows more rigid-body like behavior, and needs

larger flow speed to become parachute.

Chapter 4

Three–dimensional cell motion in fluid flows

4.1 The initial shape

Getting the initial shape of RBC in the 3D case is more delicate compared to the 2D case, thus, we want to first summarize here how to get a biconcave disk as the initial shape.

First, we shall approximate the sphere surface by triangular elements. Our mesh generator on sphere is to divide each big triangle into four congruent smaller ones and adjust their positions then repeat until desired resolution. Meshes are identified by levels, higher level means finer mesh, one level higher results in four times the number of elements. The level 0 (see Figure 4.1) mesh is given by

$$\begin{cases} x = R\sin\phi\cos\psi, \quad y = R\sin\phi\sin\psi, \quad z = R\cos\phi, \\ \phi = 0, \frac{\pi}{3}, \frac{2\pi}{3}, \quad \psi = 0, \frac{\pi}{3}, \frac{2\pi}{3}, \pi, \frac{4\pi}{3}, \frac{5\pi}{3}, 2\pi. \end{cases} \tag{4.1}$$

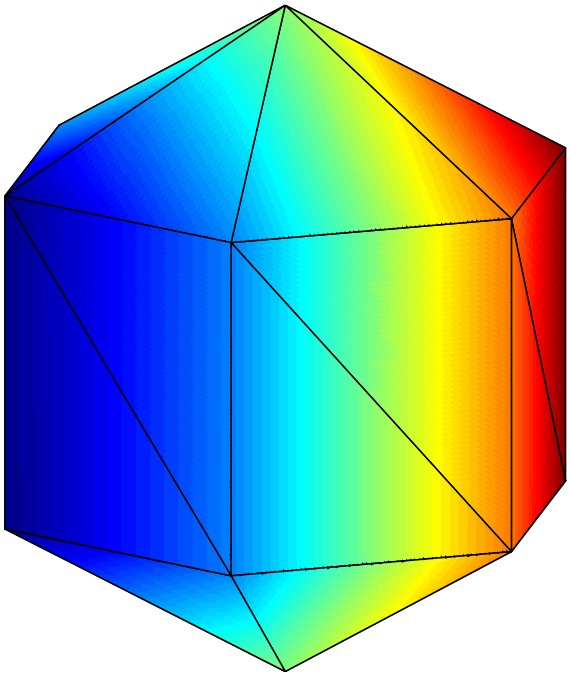

Figure 4.1: The level 0 mesh. Here R is the sphere radius.

Having level n mesh, the level $n+1$ mesh can be obtained by first adding the mid-points of all edges of each face which makes 4 small triangles within one big element, and then projecting the new points to the sphere and adjusting the nodes on the surface by the following minimization problem

$$\text{Minimize } \sum_{i=1}^{N_s} (l_i - l_{\text{mean}})^2 , \tag{4.2}$$

$$\text{Subject to } ||\mathbf{r}_j|| = R \text{ for all } j = 1, ..., N_p. \tag{4.3}$$

Here in (4.2)-(4.3) l_i represents the length of edge i, $\mathbf{r}_j$ is the jth node point, l_{mean} is the mean value of lengths of all edges.

Figure 4.2 shows levels 1-4 meshes. For each surface, N_p is the number of nodes, N_s is the number of edges, and N_e is number of elements.

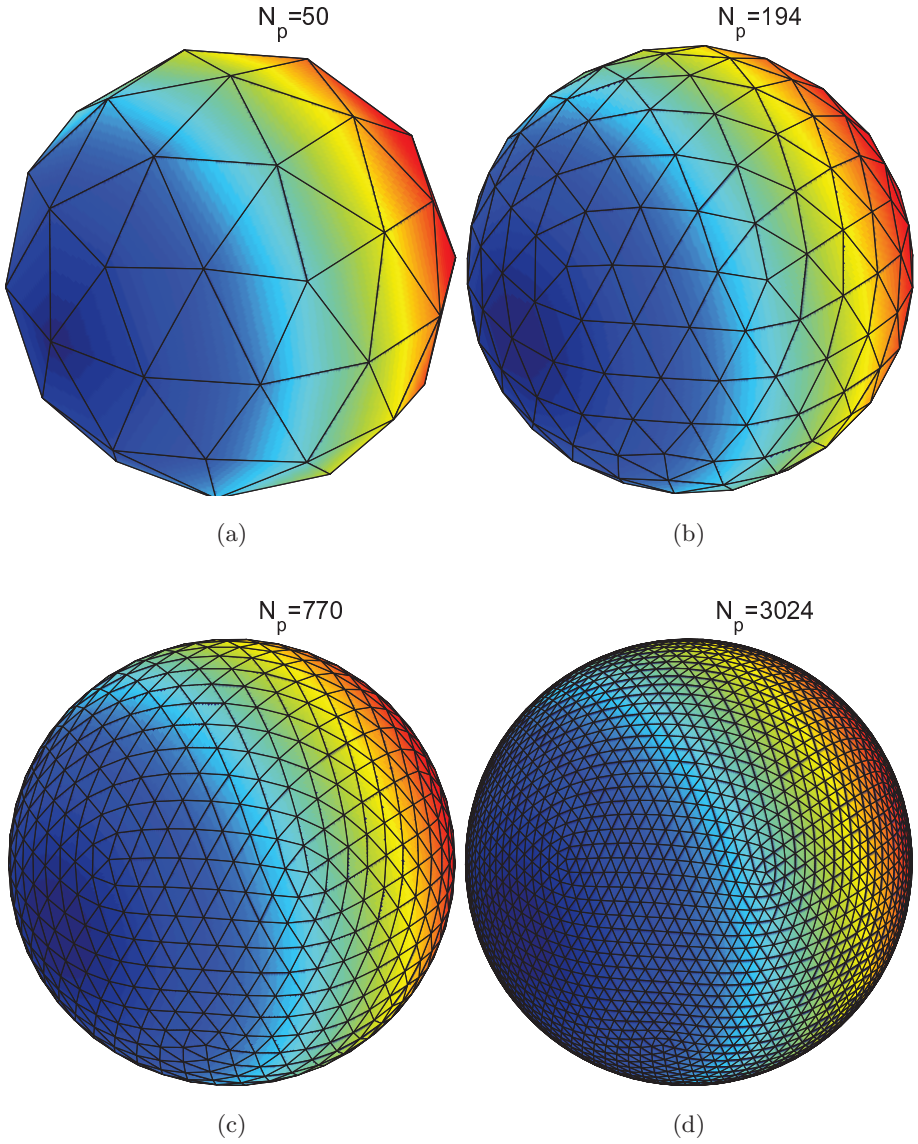

Figure 4.2: The generated mesh points and elements on the sphere surface with four different coarse levels: (a) level 1, N_p=50, N_s=144, N_e=96; (b) level 2, N_p=194, N_s=576, N_e=384; (c) level 3, N_p=770, N_s=2304, N_e=1536; (d) level 4, N_p=3074, N_s=9216, N_e=6144.

Once the mesh points are generated, one can use the model (2.17)-(2.21) to compute the initial shape of RBC by setting $\alpha = 0$. Figure 4.3 shows the initial shapes obtained for the level form one to four, using meshes presented in Figure 4.2. Although all levels can give a biconcave initial shape with the same parameters, we observe that the cell in level 1 appears to be much thicker than those in the other levels. The reason could be that level 1 mesh is too coarse, and may not be fine enough to represent cell dynamics. There are no visible differences in length and width among the cells in the other three higher levels, the level 2 cell is only slightly thicker than the ones of level 3 and level 4. The level 3 and level 4 cells have almost the identical shape.

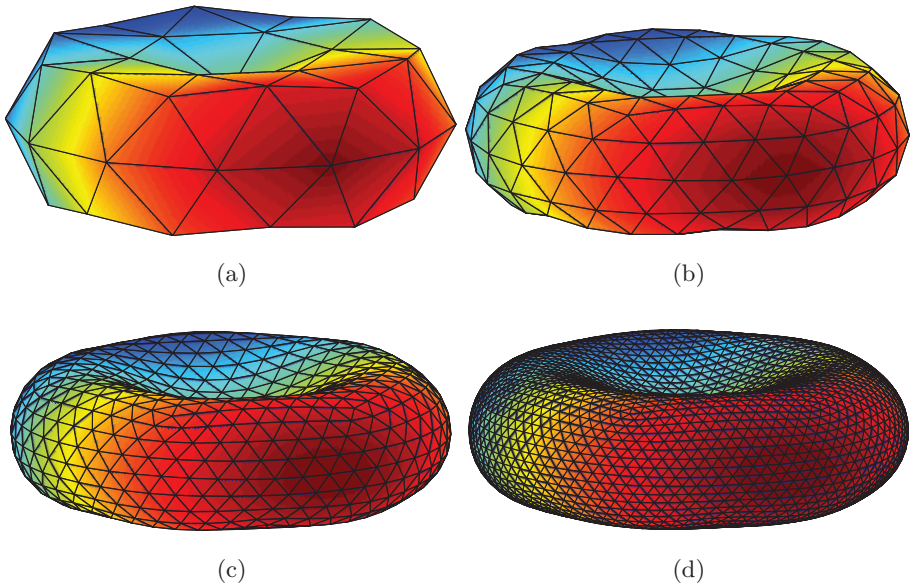

Figure 4.3: The initial shape of cell associated with four different coarse levels: (a) level 1, N_p=50, N_s=144, N_e=96; (b) level 2, N_p=194, N_s=576, N_e=384; (c) level 3, N_p=770, N_s=2304, N_e=1536; (d) level 4, N_p=3074, N_s=9216, N_e=6144.

4.2 Validation

4.2.1 The stretching test

We have performed the stretching test on the fine level ($N_p = 3074$) and two coarser levels ($N_p = 770$, $N_p = 194$) of cells at uniform natural state. The stretching force F is added evenly onto 5% of nodes around the two ends of the cell axial diameter with opposite directions, so that at each end there is a force $F/2$ acting on those nodes (see Figure 4.4, there is an example, in which the red asterisks denote the nodes having stretching forces). Here we denote D_A and D_T as the axial and transverse diameters. These two values are

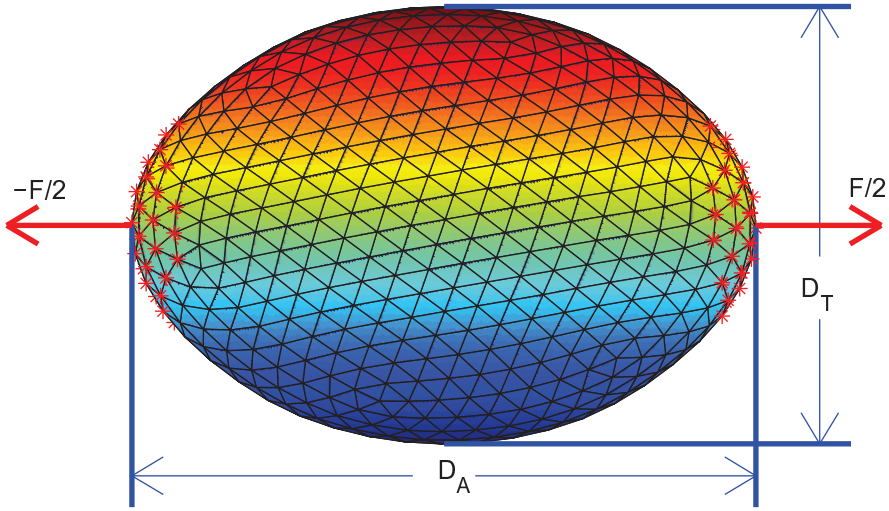

Figure 4.4: The scheme diagram of a RBC with stretching force F added onto the nodes with "$*$".

obtained, for each given force, after the cell reaches its equilibrium shape and the energy has become steady. They serve as an evaluation on how the cell is deformed to the stretching force.

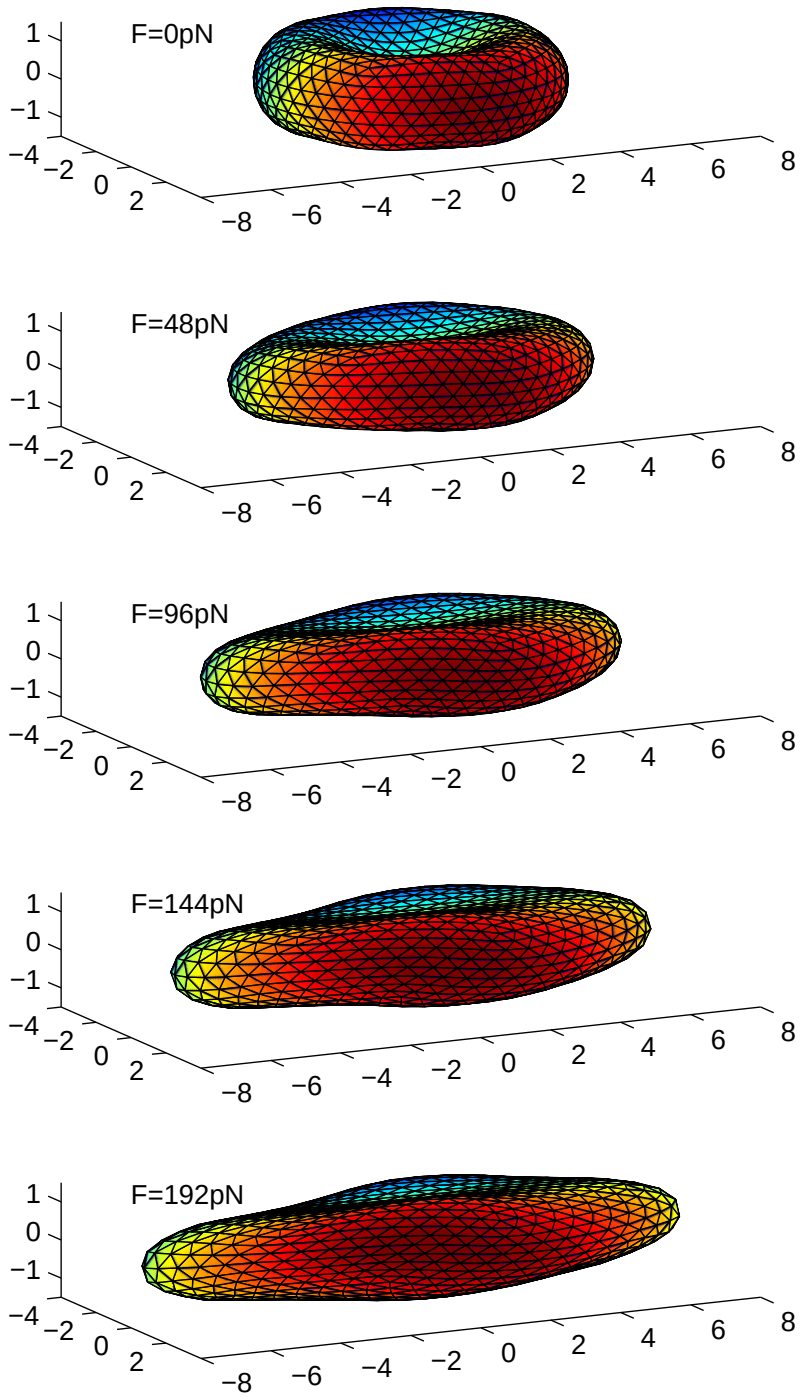

Figure 4.5: Deformated RBCs with level 3 mesh in the stretching test with different stretching forces F=0,...,192 pN.

In Figure 4.5, the cell shapes associated with different stretching forces are presented. When $F = 0$, the cell is at rest shape, with its biconcave initial shape. As stretching force raising, the cell shape is stretched to a more elongated biconcave shape with a longer axial diameter and shorter transverse diameter.

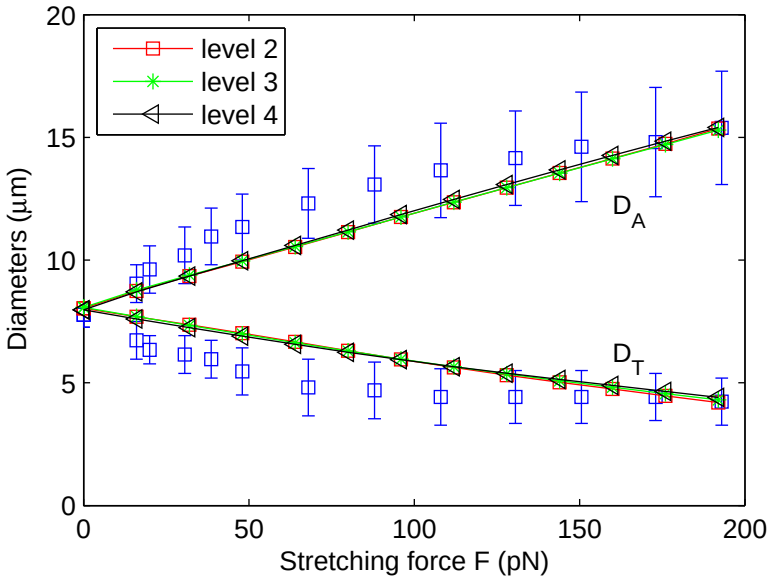

Figure 4.6: The stretching test, in our simulation, the stretching force F varies from 0pN to 192pN. Here we perform tests for the same set of parameters with different mesh levels.

As shown in Figure 4.6, the error bars correspond to the cell deformations obtained by optical tweezers [36], here red squares are for the coarse mesh (level 2, N_p=194), green asterisks correspond to the fine mesh (level 3, N_p=770), and black triangles are for the finer level (level 4, N_p=3074). The results from all three levels agree each other very well and also fit nicely into the experimental measurements. During the stretching test, with level 2 cell, the change of cell volume is within 0.1%, and the changes of local area and total surface area are within 0.5% and 0.006%, respectively; with level 3 cell, the change of cell volume is within 0.09%, and the changes of local area and total surface area are

within 0.8% and 0.005%, respectively; with level 4 cell, the change of cell volume is within 0.07%, and the changes of local area and total surface area are within 1% and 0.004%, respectively. The global errors of the surface area and cell volume do converge as mesh level becomes higher, and for the local surface area, the change only indicates the largest percentage change among all the elements, the local area preservation is much better on most of the other elements.

4.2.2 The tank–treading of RBC in shear flow

Now we suspend the cell with uniform natural state at the middle between two parallel walls. The top and bottom walls are set to move with the same speed in opposite directions (along z direction, see Figure 2.2). Periodic boundary conditions are adopted in the x and y directions. Initially the flow field is at rest. Following Sui et al. in [58], we choose scale $a = (3V_T/4\pi) = 2.8\mu m$, which is the effective radius of the RBC, and the flow is characterised by the Capillary number $C_a = \mu K a/G_s$, where μ is the viscosity of the surrounding fluid, K is the shear rate, and G_s is the shear elasticity modulus of the membrane. The Reynolds number $Re = \rho K a^2/\mu$ is fixed at 0.1 in [58], and varies between 0.014 and 0.072 in [65]. In our simulations, the range of Reynolds number is between 0.027 and 0.164. The computational domain is $\Omega = 6.4a \times 5a \times 5a$, with grid resolution $\Delta x = \Delta y = \Delta z = 1/4\mu m$ which is about $a/11$.

In our simulations, at the highest Capillary number $C_a = 2.8$, the change of cell volume with level 2 mesh is within 0.4% and the changes of cell membrane global area and local element area are within 0.7% and 1%, respectively; the change of cell volume with level 3 mesh is within 0.3% and the changes of cell membrane global area and local element area are within 0.5% and 2%, respectively; the change of cell volume with level 4 mesh is within

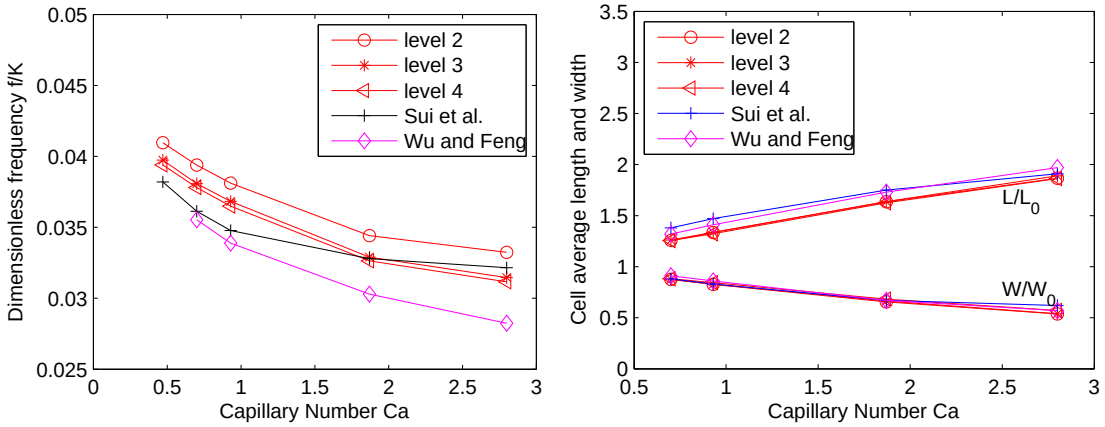

Figure 4.7: The RBC tank–treading in shear flow, the left figure shows the dimensionless frequency of tank–treading, and the right one shows the cell average length and width, with respect to different Capillary numbers.

0.2% and the changes of cell membrane global area and local element area are within 0.3% and 5%, respectively.

In Figure 4.7 we have compared our results with those in [58] and [65] (the case of fine resolution with bending). The left sub-figure corresponds to the cell dimensionless tank–treading frequency f/K versus the Capillary number. As we refine the membrane mesh, the dimensionless frequency are closer to the values from the other two works. The cell tank–treading frequency shows almost the same tendency as Wu and Feng in [65] but it is overall higher than theirs. The reason could be that even we have used a very similar model for cell membrane approximation, but our parameters are different from theirs. With their choices of k_l and k_s, the biconcave shape cannot be obtained by reducing volume from a sphere as ours. In their work, they obtain the cell initial shape by an empirical formula developed by Evans and Fung in [19]. The right sub-figure in Figure 4.7 plots the cell average length and width with respect to Capillary number, our results agree well with the

reported values obtained in [58] and [65].

4.2.3 The go-and-stop experiments in shear flow

From the results obtained in the previous two subsections, the level 2 cell can capture cell behaviors well, keep the same tendency and does not lose too much accuracy comparing to the level 3 and level 4 cells. In addition, it saves a huge amount of computational time when using level 2 mesh. Therefore, in this subsection, we perform the go-and-stop experiments on level 2 cells only, since we only care about the cell behavior after the outside force is removed.

In the go-and-stop experiments, all parameters or conditions are the same except the values of α. The computational domain is $\Omega = 20\mu m \times 20\mu m \times 20\mu m$. The mesh size is $\Delta x = \Delta y = \Delta z = 5/16\mu m$, and the time step is $\Delta t = 10^{-4}$ms. The parameters for the spring networks are chosen to be the same as in the previous subsections. At the beginning cell was suspended in shear flow with a fixed Capillary number $C_a = 1.1$, with the periodic boundary conditions in the x and z directions, the top and bottom of Ω has Dirichlet boundary condition which is determined by the Capillary number. With all the α values in $[0, 1]$, the cell behaves quite similar at the beginning. The cell exhibits tank–treading motion and gets to an (almost) elongated ellipsoidal shape. The tank–treading motion can be easily identified by following a marked membrane particle which was at the dimple initially with a blue dot. When the flow is stopped, the motion of the cell and the position of the marked particle have been checked for a long period of time to determine whether the shape memory effect is presented. In this subsection, figures are plotted with the same scale, so that one can easily identify if cell is elongated or not directly from comparing the cell lengths.

Figure 4.8 shows the case of uniform natural state ($\alpha = 0$). At time $t = 0$ms, the cell is suspended in the fluid with a flat inclination angle and the marked particle is at its initial position, the dimple. As the flow starts, the cell exhibits tank–treading motion in an elongated ellipsoidal shape, with the marked particle travelling along the cell membrane. After stopping the motion of the two walls at time $t = 16.7$ms, the cell quickly changes the shape back to a biconcave disk by shrinking the cell length and increasing the cell thickness. However, the marked particle does not go back to the dimple even after a long time (more than 40ms) of resting. Here the view in the plots is from the front of the channel, i.e. the observer is at position $(10\mu m, 0\mu m, 0\mu m)$.

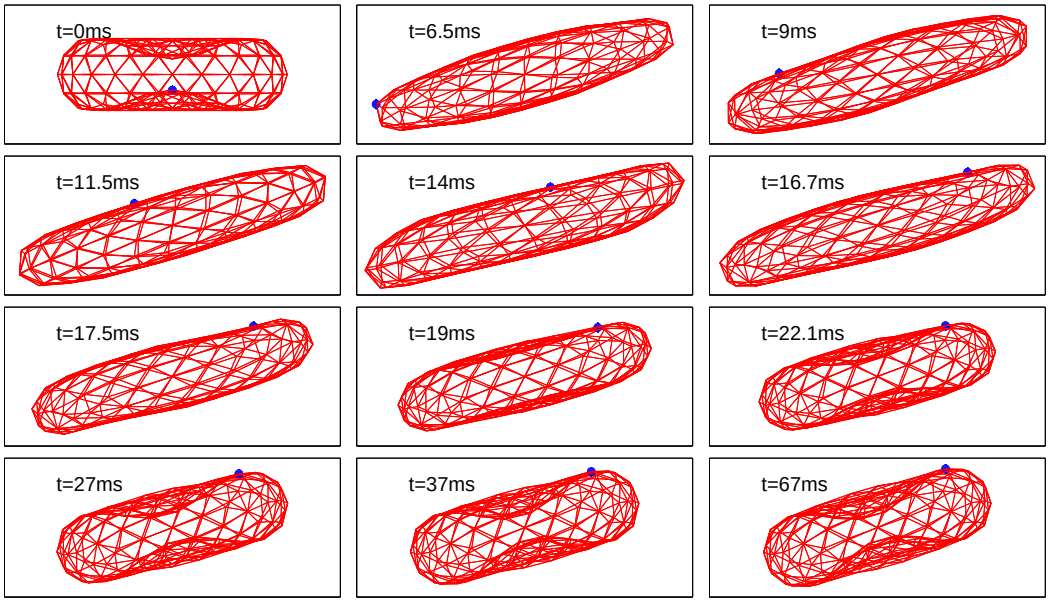

Figure 4.8: The go-and-stop experiment for the cell with uniform natural state ($\alpha = 0$), the cell is suspended in a shear flow with $C_a = 1.1$. The motion of the two walls is stopped at time $t = 16.7$ms.

When $\alpha = 1$ (i.e. the cell with a strong memory of the biconcave disk shape), as shown

in Figure 4.9, the cell also gets to an elongated ellipsoid, but its shape seems to be slightly shorter in length than the one with $\alpha = 0$. Similar to the previous case, the marked membrane particle also travels along the membrane when the cell is tank–treading in the shear flow. After stopping the motion of the two walls at time $t = 16.6$ms, the cell recovers its biconcave disk shape very quickly with little rotation. Right after that, the cell rotates, while the marked particle tank–treads back to the dimple of the biconcave shape, which is its initial position before deformation. For $t \leq 22$ms, the cell is viewed from the position $(10\mu m, 0\mu m, 0\mu m)$, as in Figure 4.9. But after $t = 27$ms, we have to view the cell from a

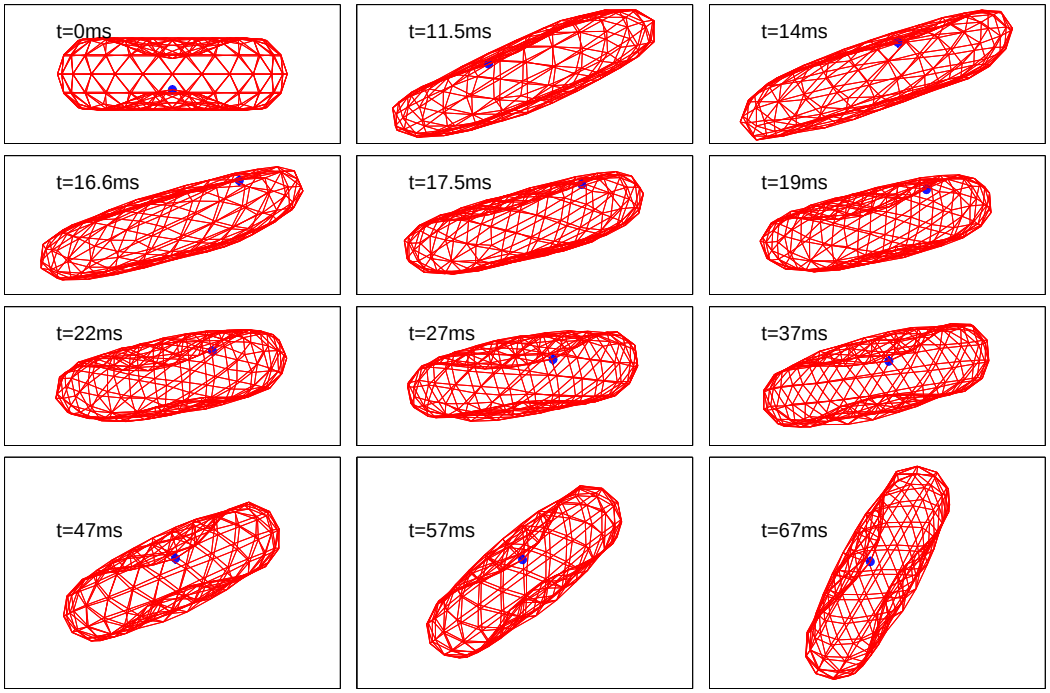

Figure 4.9: The go-and-stop experiment for the cell with nonuniform natural state ($\alpha = 1$), at first cell is suspended into shear flow with $C_a = 1.1$, and the flow is stopped at time $t = 16.6$ms.

carefully chosen position at each time to plot the longitude axis of the cell. One possible

explanation on why the cell rotates is about the forced acting on the cell and the surround fluid. When the motion of the two walls is stopped, the cell shape is still elongated at first. Then the force to pull the cell back to its biconcave shape is dominating, and this force is acting towards the center of the cell (see Figure 4.9, $t = 16.6$ms). But when the cell is almost back to its biconcave shape, the dominating force is one takes the dimple particle back to dimple. Since the membrane tank–treads about the mass center, and in return it gives a rotational force to the surrounding fluid.

We have also tested cases with some values of α between $(0, 1)$. For example, at $\alpha = 0.3$ (see Figure 4.10), the elongated ellipsoid formed in shear flow is quite similar to the previous two cases, the length of ellipsoid is longer than the one for the case $\alpha = 1$ and slightly shorter than the one for the case $\alpha = 0$. The cell behavior, after stopping the motion of the two walls, is the same as in the case $\alpha = 1$, since they both take into account the nonuniform natural state. The cell has some rotation about its mass center during the dimple back to dimple motion, but the rotational behavior is not as strong as the cases with larger values of α. Figure 4.11 shows the dimple to dimple motion after the two walls stop moving(viewed from top of the cell): (i) at $t = 16.6$ms, the two walls stop moving and the cell is still in an elongated ellipsoid shape, and the marked dimple membrane particle is at some position other than its initial position at the natural state; (ii) between $t = 16.6$ms and $t = 22$ms, the cell changes its shape from an elongated ellipsoid back to a biconcave disk. Hence the top view of the cell shows almost a round shape at $t = 22$ms. During this period, no visible tank–treading occurs and the marked dimple particle almost keeps the same position on the membrane; and (iii) after the cell returns to a biconcave disk, the membrane starts to tank–tread and the dimple particle is back to the dimple. Thus, we believe that the non-uniform cell surface mesh (i.e., every point on the membrane is not identical) at our so called "uniform natural state", cannot move the dimple back to

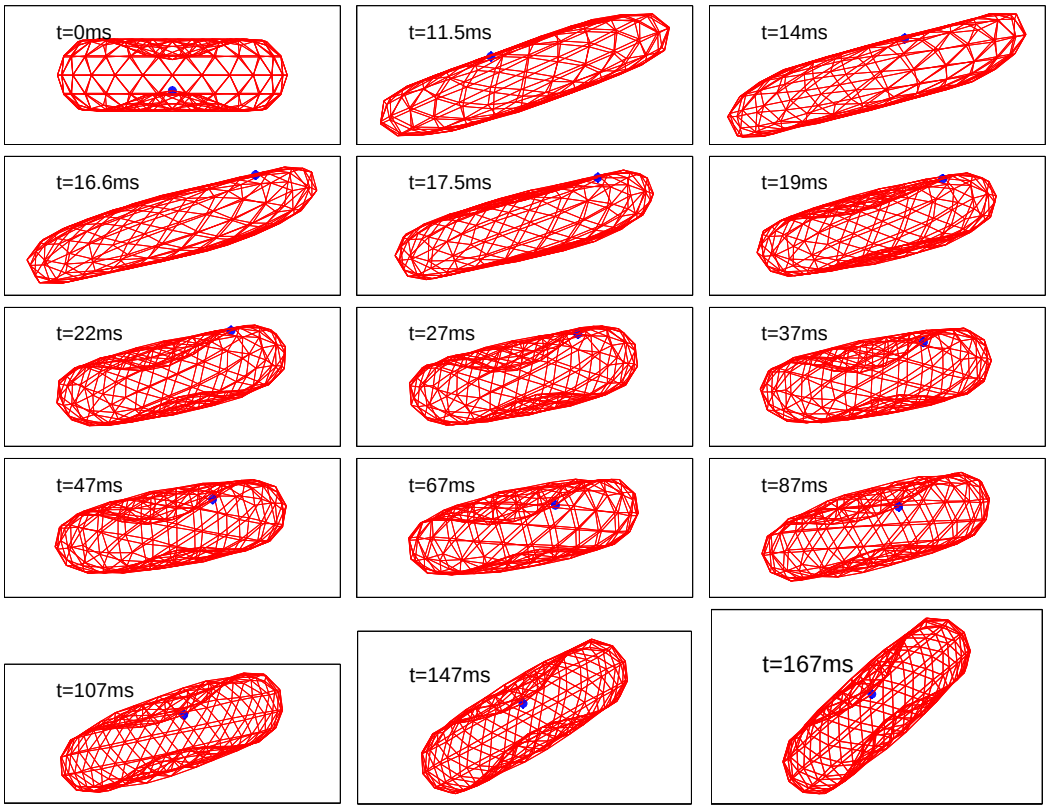

Figure 4.10: The go-and-stop experiment for the cell with $\alpha = 0.3$, the flow is stopped at time $t = 16.6$ms.

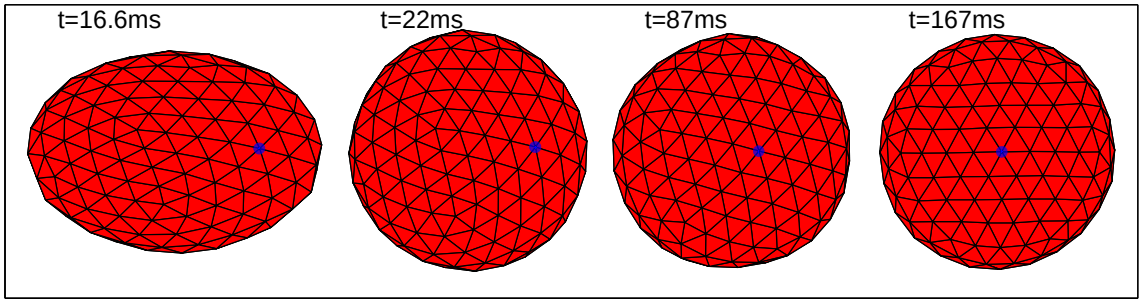

Figure 4.11: Cell bevior: dimple back to dimple after flow stopped at $t = 16.6$ms for the cell with $\alpha = 0.3$. The figures are viewed from the top of the RBC.

its initial position and rim back to rim (which is called the shape memory property) in shear flow once the motion of two walls is stopped. But such non-uniform surface mesh can cause the swinging mode during tank–treading motion with cells in such state (which will be discussed in the next subsection). To ensure the shape memory property, the cell does need some memory of the "nonuniform natural state" related to the biconcave disk (or an ellipsoid as adopted in [61, 62], for example) as proposed in this thesis.

4.3 RBC motion in shear flow

As in the 2D case, cell can exhibit different motions in shear flow at different shear rates (characterized by Capillary numbers). In this section, we want to consider the cell motion in 3D shear flow with periodic boundary condition along the x and z directions, and Dirichlet condition on the top and bottom of the channel, as described in equations (2.11) - (2.13) and Figure 2.3(top). The computational domain is $\Omega = 20\mu m \times 20\mu m \times 20\mu m$. The mesh size is $\Delta x = \Delta y = \Delta z = 5/16\mu m$. To find the transition between the tumbling and tank–treading motions, we have studied the cell behaviors in shear flow, with low shear rates $K = 15$, 20, 25, and $30s^{-1}$. The corresponding Reynolds numbers are 9.8×10^{-5}, 1.3066×10^{-4}, 1.6333×10^{-4}, and 1.96×10^{-4}, respectively, and the Capillary numbers are 0.0155, 0.0207, 0.0259, and 0.0310, respectively. In this section, we fix $\alpha = 0$ and vary the membrane mesh among level 2, level 3, and level 4.

At the shear rate $K = 25s^{-1}$, as shown in Figure 4.12, the cell with level 2 mesh performs tumbling motion. Here we only plot the skeleton structure via the coarse grained spring networks, and to follow the phase shift of the cell membrane we have marked the membrane particle which was originally at the dimple in reference shape with a blue dot. Figure 4.12 shows a typical half cycle of tumbling motion, during which cell keeps its

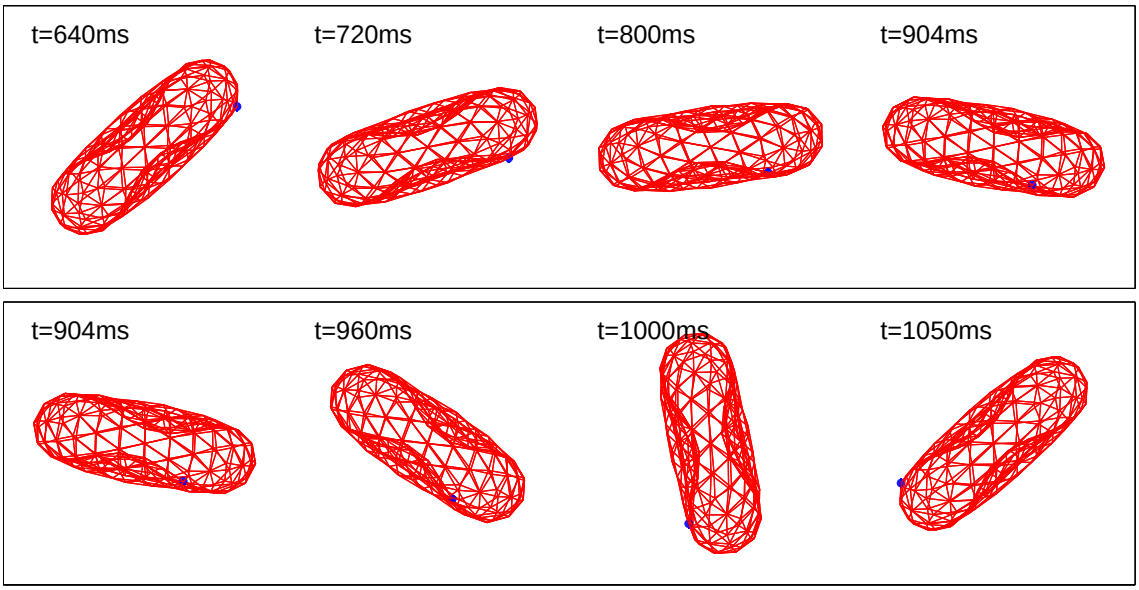

Figure 4.12: Snapshots of the level 2 cell tumbling in shear flow, which completes a half cycle from $t = 32ms$ to $t = 52.5ms$, with shear rate $K = 25s^{-1}$.

biconcave shape. At $t = 32$ms, the dimple particle is at a position which is the farthest during the tumbling, and at the instance the cell forms some angle with the xz-plane. As the cell slowly rotates clockwisely, the dimple particle starts to tank–tread closer to the dimple, until some time $t = 45.2$ms, it reaches a position that is closest to the dimple. And from then the cell rotates faster, with the dimple particle pushed away from the dimple and reaches the farthest position again at $t = 52.5$ms. This procedure makes a 180° orientation shift (look at the change of the axial axis), while the phase shift (look at the change of the marked particle position on the membrane) is 0°.

If the shear rate is raised to be $30s^{-1}$ or greater, the cell with level 2 mesh tank–treads instead of tumbling. Figure 4.13 shows a typical half cycle of tank–treading motion, during which the cell orientation is swinging upwards and downwards alternatively, with an almost

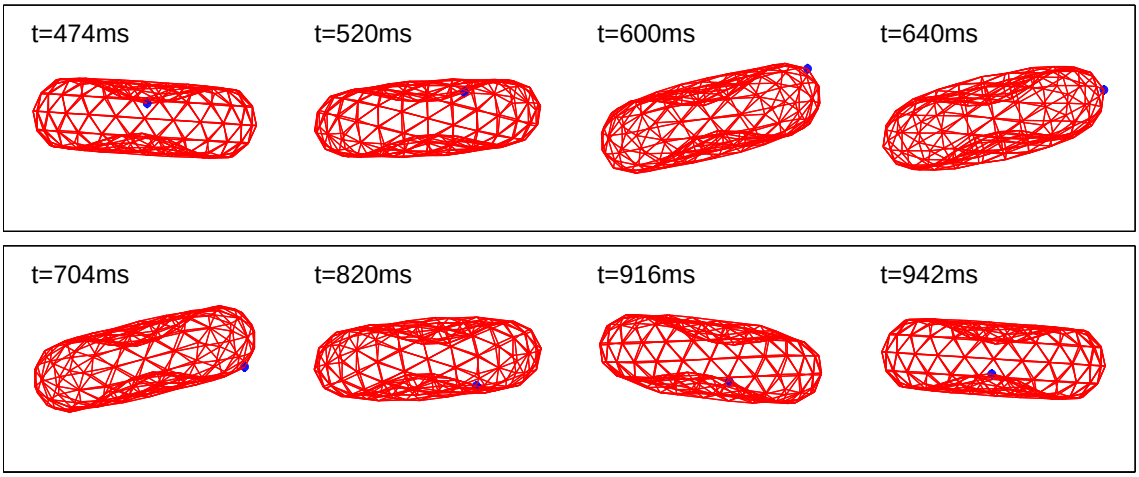

Figure 4.13: Snapshots of the level 2 cell tank–treading in shear flow, which completes a half cycle from $t = 23.7ms$ to $t = 47.1ms$, with shear rate $K = 30s^{-1}$.

biconcave disk shape. Following the marked membrane particle, we can see that the dimple particle is travelling along the cell membrane from a dimple to the one in the other side of the cell. Therefore the half cycle of cell tank–treading makes a 0° orientation shift and a 180° phase shift.

With the level 2 cell, the tumbling-to-tank–treading transition occurs between shear rates $25s^{-1}$ and $30s^{-1}$. For finer level cells, the transition occurs at lower shear rates. For example, the level 3 cell tumbles when $K = 20s^{-1}$, but tank–treads as we raise the shear rate to be $25s^{-1}$ (See Figures 4.14 and 4.15). For the level 4 cell, the transition happens when shear rate is within $[15, 20]s^{-1}$, and we can expect that by using finer and finer levels of membrane mesh, the transition between tumbling and tank–treading in shear flow would decrease and converge to the experimental measured value obtained in [17]. Next we have plotted in Figure 4.16 the histories of energy for the tumbling cells at levels 2 and 3, with different shear rates. At higher shear rates, both the local maxima and the local minima

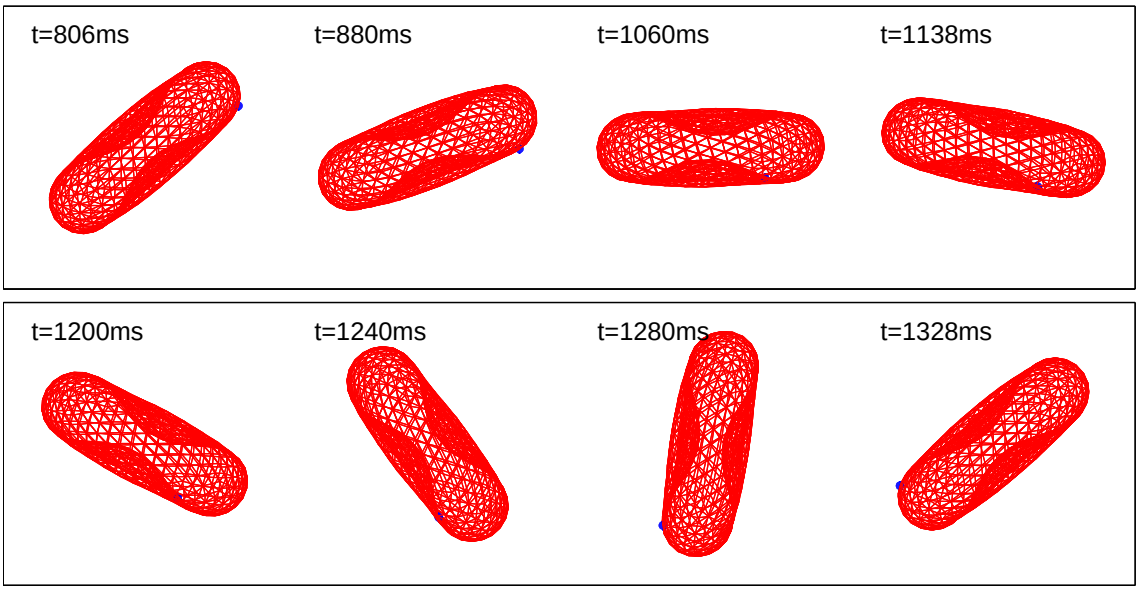

Figure 4.14: Snapshots of the level 3 cell tumbling in shear flow, which completes a half cycle from $t = 40.3ms$ to $t = 66.4ms$, with shear rate $K = 20s^{-1}$.

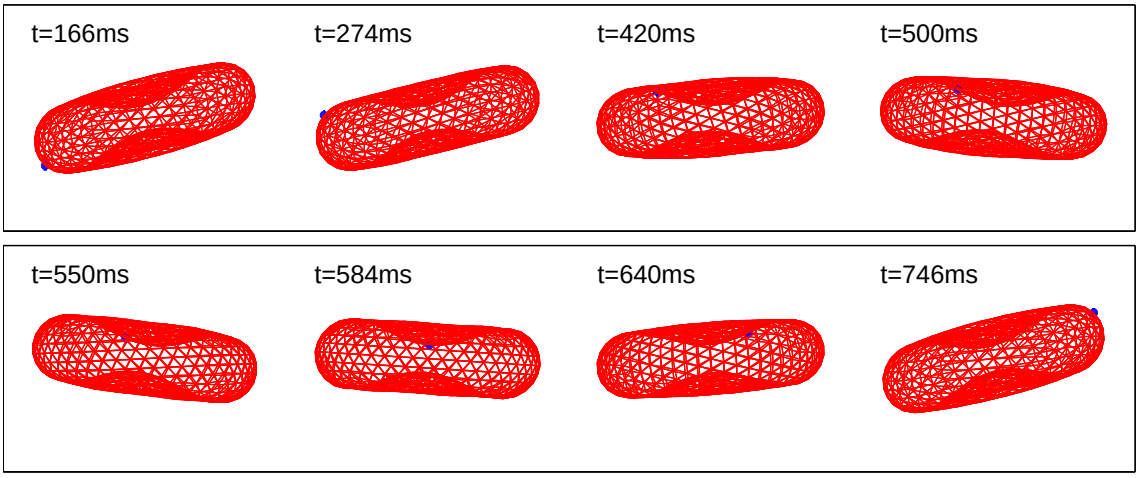

Figure 4.15: Snapshots of the level 3 cell tank–treading in shear flow, which completes a half cycle from $t = 8.3ms$ to $t = 37.3ms$, with shear rate $K = 25s^{-1}$.

are higher. It is because the cell energy is related to the membrane structure. At lower shear rates, the dimple particle does not move out very much and hence causes little energy change, also the maximal energy would be smaller; at higher shear rates, the dimple particle has moved farther, which gives more energy change to reach a higher maximal energy.

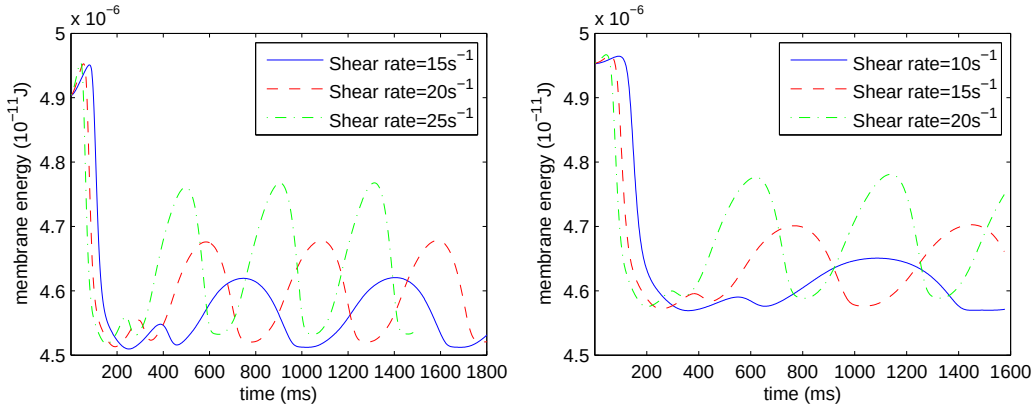

Figure 4.16: Histories of the energy of cell tumbling in shear flow: the energies of the cell with level 2 mesh at shear rates $K = 15,\ 20,\ 25s^{-1}$ (left); and the energies of the cell with level 3 mesh at shear rates $K = 10,\ 15,\ 20s^{-1}$ (right).

4.4 RBC motion in tube Poiseuille flow

Shi et al. has studied in [56] the cell behaviors in a narrow tube, as well as in a slit Poiseuille flow. They found that in the narrow tube with radius $5\mu m$ and channel length $50\mu m$, the cell equilibrium shapes are parachutes. And in slit Poiseuille flow where periodic boundary condition is adopted in two directions, except the the top and bottom of the channel, the equilibrium shapes appear to be dependent on the flow velocities (and hence dependent on Capillary numbers). The cell has a slippery shape in slowly moving fluid. In their paper, they have fixed the computational domain to be $28\mu m$ in channel length, $14\mu m$ in

height, and $28\mu m$ in width. The periodic boundary condition in the x and z directions in their work gives in some sense like a 2d profile while using 3d settings, this confirms the results of equilibrium shapes in 2D Poiseuille flow. However, we are interested here in some questions such as: (i) will the same equilibrium shapes appear in a tube Poiseuille flow with a rectangular cross section? (ii) Is there anything to do with the channel height?

Having these thoughts in mind, we now want to consider a computational domain with periodic boundary condition only in the z direction, and has Dirichlet boundary conditions elsewhere as illustrated in equations (2.14) - (2.16) and Figure 2.3(bottom). Here we first present the results regarding to the effect of channel height, as well as the pressure gradient in the z direction. In our study, we have chosen the channel with the length of $40\mu m$, the width of $20\mu m$, and the heights of either $20\mu m$, $15\mu m$, or $10\mu m$. And we have only used the cell with the level 2 mesh in this section. The Reynolds number is defined by $Re = \rho H U_{max}/\mu$, where H is the height of the channel, and U_{max} is the maximum velocity without cell for the same pressure gradient. The Capillary number is defined as $C_a = \mu U_{ave}/G_s$, where U_{ave} is the average velocity of the flow without cell, and $G_s = \frac{\sqrt{3}}{4}k_l$ is the shear modulus. The flow profiles are preset to be at rest initially, and a pressure gradient in the z direction is added onto the whole domain when $t > 0$ms. We have used here $\nabla p = 1 \times 10^{-7}N$, $2.5 \times 10^{-7}N$, $5 \times 10^{-7}N$, $7.5 \times 10^{-7}N$, and $1 \times 10^{-6}N$ (per unit volume) in our simulations. Due to the change of the channel heights, the maximum velocity will vary and hence the Reynolds numbers and Capillary numbers will also take different values even the pressure gradients are the same. For the case that $H = 20\mu m$, the corresponding Reynolds numbers are 0.0409, 0.1023, 0.2046, 0.3068, 0.4092, respectively, and the Capillary numbers are 0.4536, 1.1339, 2.2679, 3.4018, 4.5358, respectively; for the case $H = 15\mu m$, the corresponding Reynolds numbers are 0.0220, 0.0549, 0.1098, 0.1647, 0.2196, respectively, and the Capillary numbers are 0.3246, 0.8114, 1.6229, 2.4343, 3.2458,

respectively; for the case $H = 10\mu m$, the corresponding Reynolds numbers are 0.0079, 0.0198, 0.0395, 0.0593, 0.0791, respectively, and the Capillary numbers are 0.1753, 0.4382, 0.8764, 1.3146, 1.7527, respectively.

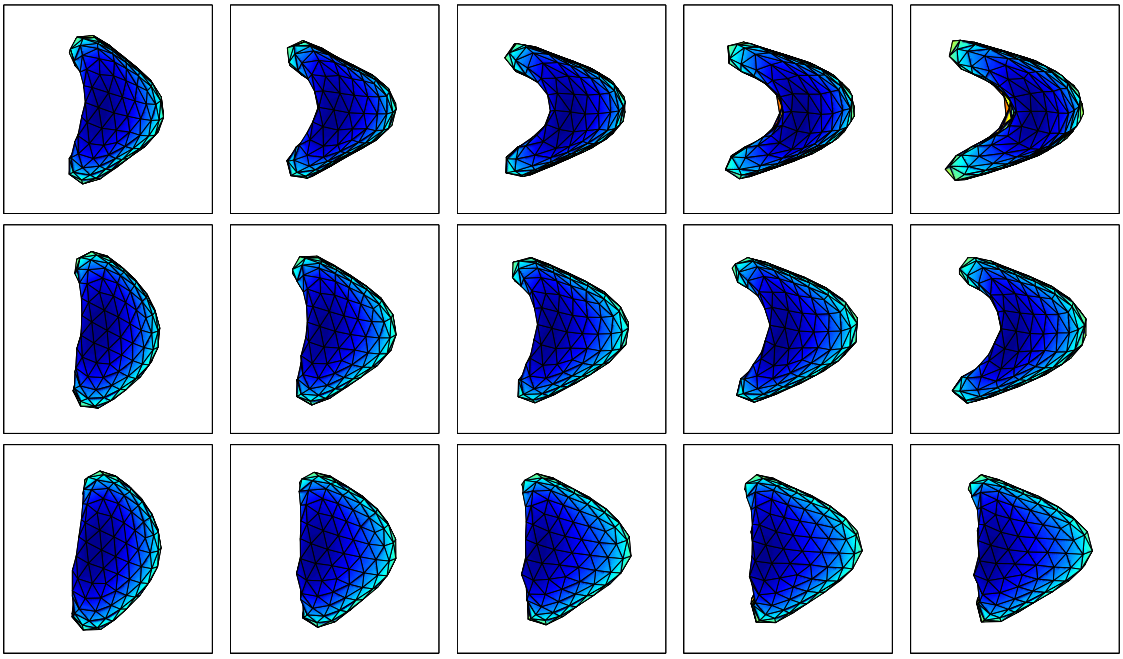

Figure 4.17: Equilibrium shapes of the cell in a narrow channel $\Omega = 20\mu m \times 10\mu m \times 40\mu m$ (top), a wider channel $20\mu m \times 15\mu m \times 40\mu m$ (middle), and the widest channel $\Omega = 20\mu m \times 20\mu m \times 40\mu m$ (bottom), with pressure gradients $1 \times 10^{-7}N$, $2.5 \times 10^{-7}N$, $5 \times 10^{-7}N$, $7.5 \times 10^{-7}N$, $1 \times 10^{-6}N$, from left to right, respectively. For all cases, we have $\alpha = 0$ (i.e., no effect of shape memory).

Figure 4.17 shows the equilibrium shapes for the cell with uniform natural state ($\alpha = 0$). The cell gets to a parachute shape for all choices of pressure gradients if the channel width is $20\mu m$. Because for such a channel, the flow profile is symmetric and that gives a parachute shaped cell for all choices of pressure gradients, similar to the cell shapes in a narrow tube

in [56]. As we narrow the width of the channel, the equilibrium shapes become more 2D like (the shapes look similar to the cell equilibrium shapes obtained in 2D Poiseuille flow as in Figure 3.27 and reffig.29), let us call such a shape "2D parachute". For higher pressure gradients, which corresponds to faster flows, the parachute shape is deeper, and the length of the cell (the distance from highest to lowest positions) is shorter. The cell equilibrium shapes do not depend on the initial inclination angles between cell orientation and the xz-plane (in our work the initial position of cell is always placed perpendicular to the yz-plane, only the angle between the cell and xz-plane may change). As shown in Figure 4.18, even if the initial inclination angle is not vertical, the cell with uniform natural state still changes to a symmetric shape as a (2D) parachute. In these cases, it is first driven to a slipper very quickly, and then changes slowly into the final equilibrium shape, while in our simulations, cells with a vertical inclination angle is driven into a parachute or 2D

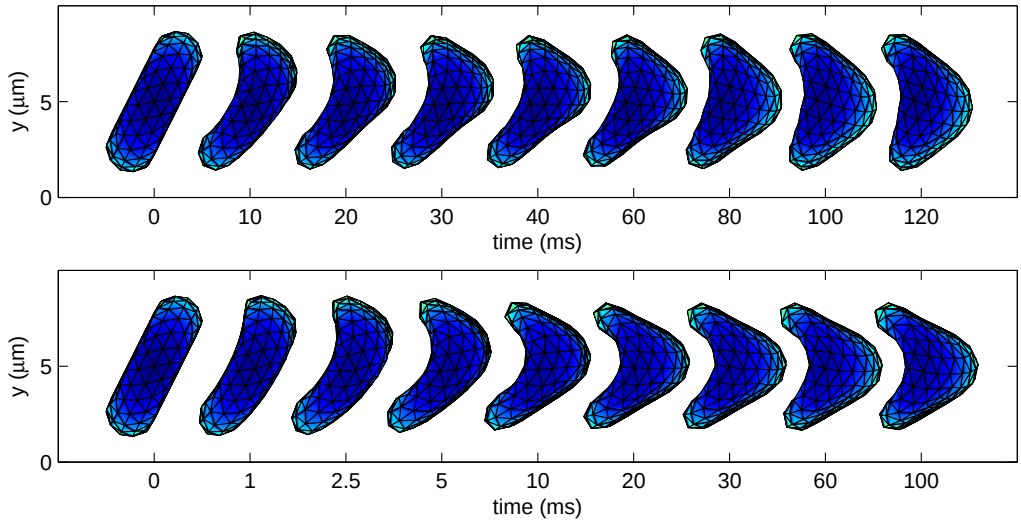

Figure 4.18: Snapshots of the cell in the narrow channel $\Omega = 20\mu m \times 10\mu m \times 40\mu m$, with pressure gradients $1 \times 10^{-7}N$ (top) and $2.5 \times 10^{-7}N$ (bottom), for the case $\alpha = 0$.

parachute shape for all choices of pressure gradients at the beginning (See Figure 4.19 for

the cells with nonuniform natural state. Not shown here for the cell with uniform natural state, because we observe that the behavior at the very beginning is almost the same for both $\alpha = 0$ and $\alpha > 0$).

When taking the nonuniform natural state into account, for example, in the case $\alpha = 0.1$ (see Figure 4.19), the cell gets to a slippery shape for lower pressure gradients in narrow channel. At higher pressure gradients, it changes to a 2D parachute. The cells is initially suspended vertically, everything was symmetric about the z-axis at $t = 0$ms, and therefore the cell is driven to a parachute shape which matches the Poiseuille flow profile the best. But since the cell is under the effect of shape memory, the 2D parachute shape needs higher energy to sustain its shape which slow fluids cannot provide, and thus the cell changes to a slippery shape afterwards.

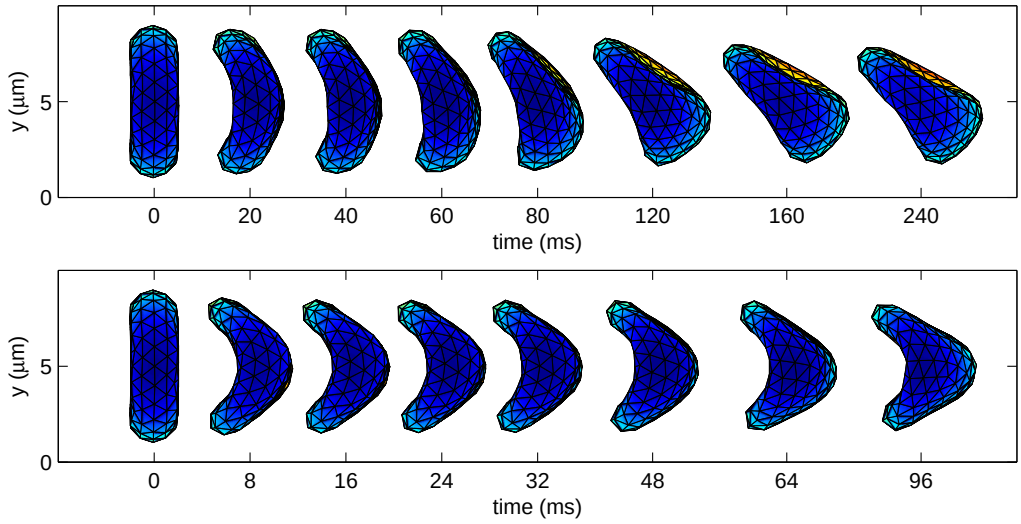

Figure 4.19: Snapshots of the cell in the narrow channel $\Omega = 20\mu m \times 10\mu m \times 40\mu m$, with pressure gradients $1 \times 10^{-7}N$ (top) and $2.5 \times 10^{-7}N$ (bottom), for the case $\alpha = 0.1$.

In Figure 4.20, we present the equilibrium shapes of the cell with the same channel

heights and pressure gradients as in Figure 4.17, for the case of $\alpha = 0.1$, the figures are

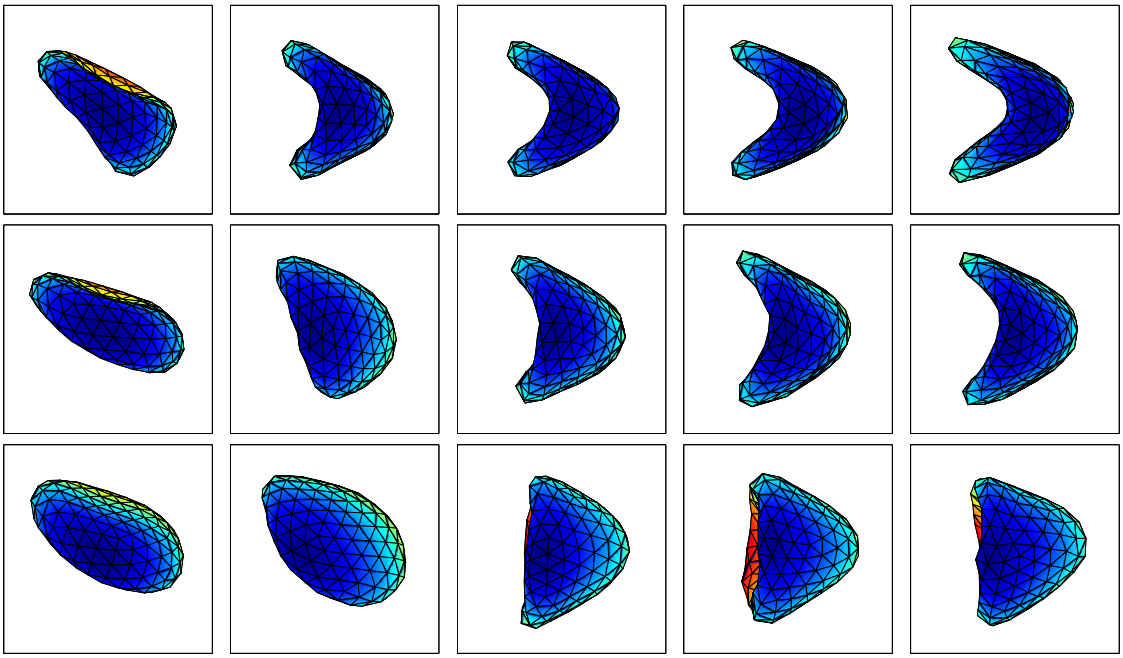

Figure 4.20: Equilibrium shapes of the cell in a narrow channel $\Omega = 20\mu m \times 10\mu m \times 40\mu m$ (top), a wider channel $20\mu m \times 15\mu m \times 40\mu m$ (middle), and the widest channel $\Omega = 20\mu m \times 20\mu m \times 40\mu m$ (bottom), with pressure gradients per unit volume $1 \times 10^{-7}N$, $2.5 \times 10^{-7}N$, $5 \times 10^{-7}N$, $7.5 \times 10^{-7}N$, $1 \times 10^{-6}N$, from left to right, respectively.

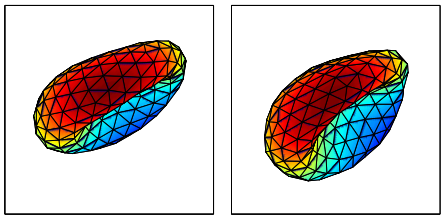

Figure 4.21: Replot of the two lower left subfigures in Figure 4.20, view from the opposite side of the channel.

plotted with a observer at $(10\mu m, 0, 0)$. For those plots with low pressure gradients in the

wide channels, i.e. the subfigures in the lower-left corners of Figure 4.20, the cell equilibrium shape is not symmetric with respect to the yz-plane. For example, for $H = 20\mu m$ and pressure gradients 1 and $2.5 \times 10^{-7} N$ per unit volume, the cell was viewed at (-10$\mu m, 0, 0$) as presented in Figure 4.21 and the cell equilibrium shape is not symmetric with respect to the yz-plane any more.

4.5 RBC going through a micro-channel with blockage

In [6], Braunmuller et al. found that after cell flowing through micro-channels with abrupt constrictions, two stage of relaxation processes were observed in experiments: in a short period of time, the cell first relaxes into a cup shape, and then the relaxation of cell from the cup shape into the well-known biconcave rest shape takes much more time and it is usually coupled with reorientation.

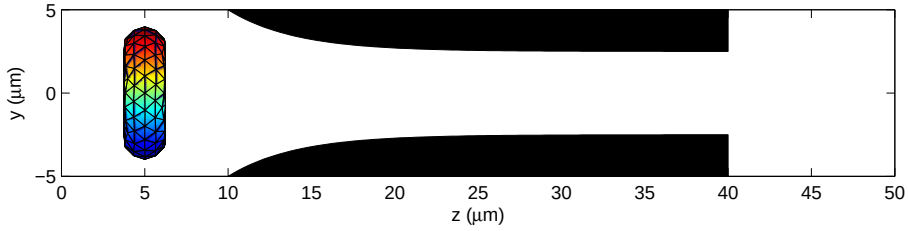

Figure 4.22: Schemetic diagram of a single red blood cell suspended in a micro-channel with blockage.

Here, as shown in Figure 4.22, we have designed a similar micro-channel as described in (2.74) - (2.78), where the computational domain $\Omega = (-5, 5) \times (-5, 5) \times (0, 50)$, and the blockage $\bar{\omega}$ is defined as $\bar{\omega} = ((-5, 5) \times (-5, Y_1(z)) \times (0, 50)) \cup ((-5, 5) \times (Y_2(z), 5) \times (0, 50))$,

with

$$Y_1(z) = \begin{cases} -\frac{5}{2}(1+\exp(\frac{5}{2}(1-\frac{z}{10}))) \text{ if } 10 \le z \le 40, \\ -5 \text{ elsewhere;} \end{cases} \tag{4.4}$$

and $Y_2(z) = -Y_1(z)$ for all $z \in (0, 50)$. A RBC is to pass through a narrowest part with height $5\mu m$, which is less than the diameter of the cell. A pressure gradient is added so that $U_{max} = 0.1cm/s$ in the wider part of the channel. As entering the narrower part of the micro-channel (see Figure 4.23 as an example when the cell is in uniform natural state), cell is compressed into a (2D) parachute shape and then keeps almost parachute during most of the time. When the cell is out from the narrower part, it quickly changes to a cup shape.

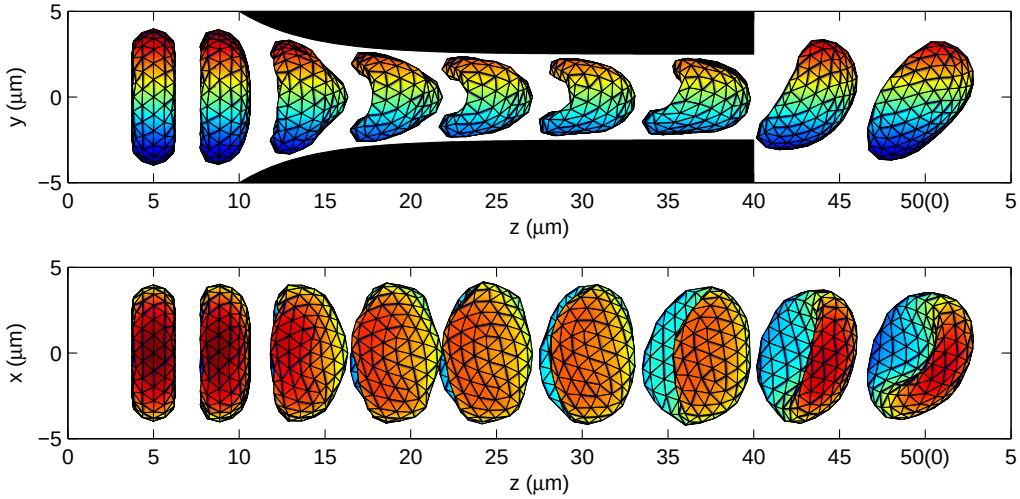

Figure 4.23: Shapes of the cell at different locations in the channel: (top), side view, observe from (10,0,0); (bottom), top view, observe from (0,10,0). Both figures are plotting exactly the same cell at same locations. The corresponding times are $t = 0$ms, 15ms, 30ms, 45ms, 60ms, 77ms, 95ms, 115ms, 137.2ms, respectively, for the case $\alpha = 0$.

Figure 4.24 shows the cell behavior after the flow maximum velocities is reduced into

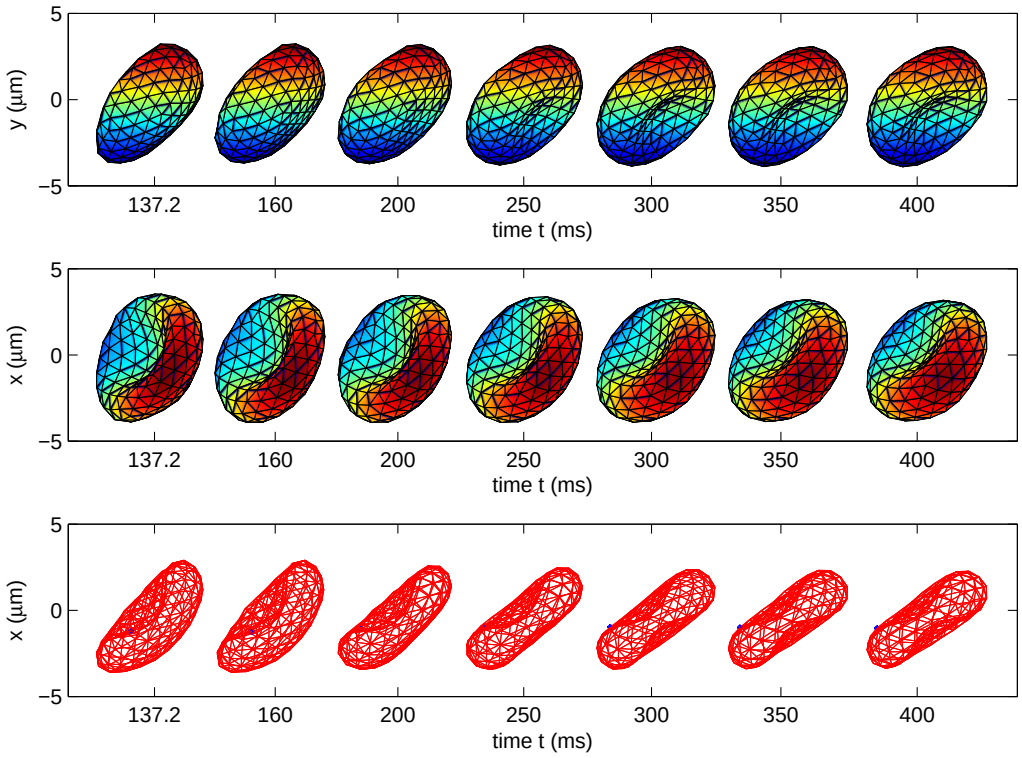

Figure 4.24: Shapes of the cell at different locations in the channel: (top), side view, observe from (10,0,0); (middle), top view, observe from (0,10,0); (bottom), view from the side of RBC such that longitude is presented in figure. All the three figures plots the same cell at same times, which are $t = 137.2$ms, 160ms, 200ms, 250ms, 300ms,350ms, 400ms, respectively, for the case $\alpha = 0$.

1% of the original. We chose this setting because, in the experiment, the wider part of the micro-channel is about 50 times the width of the narrow part; but, in practice, it requires very heavy computations. However, since the flow velocity in the very wide part of the channel is almost stationary, we can instead reduce the flow speed and adopt a channel with the wider part only twice the width of the narrower part to mimic this "narrow-to-wide" transition. We observe that after getting out from the narrow part of the micro-channel,

the cell becomes a cup shape very quickly and keeps in this state for about 200ms. Then it changes to a biconcave disk without tank–treading dimple back to dimple, and at the same period of time, the cell orientation keeps unchanged after the cell coming out from the narrower part of the channel. As we keep relaxing the cell for another 200ms, the dimple particle just stays at the same place and the cell does not show a tendency to rotate or tank–tread.

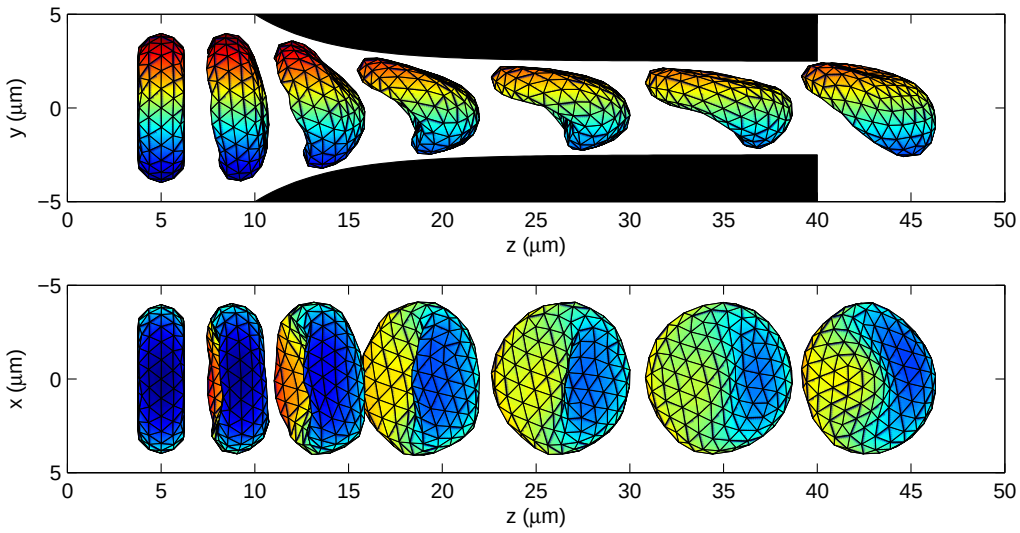

Figure 4.25: Shapes of the cell in different locations in the channel: (top), side view, observe from (10,0,0); (bottom), bottom view, observe from (0,-10,0). Both figures are plotting exactly the same cell at same locations. The corresponding times are $t = 0$ms, 15ms, 30ms, 46ms, 66ms, 86ms, 106ms, respectively, for the case $\alpha = 0.3$.

Next we show in Figure 4.25 the results of a RBC with nonuniform natural state going through the micro-channel. As discussed in the previous subsection, the cell with higher effect of shape memory tends to need more energy to keep a parachute shape. Hence, with the same maximum velocity, the cell is in a slipper shape (with tank–treading) while

passing through the narrower part.

Similarly to the cell with uniform natural state, the cell under effect of shape memory also gets to a cup shape very fast after coming out from the narrower part of the microchannel. After that, it changes back to a biconcave disk, as plotted in Figure 4.26. One

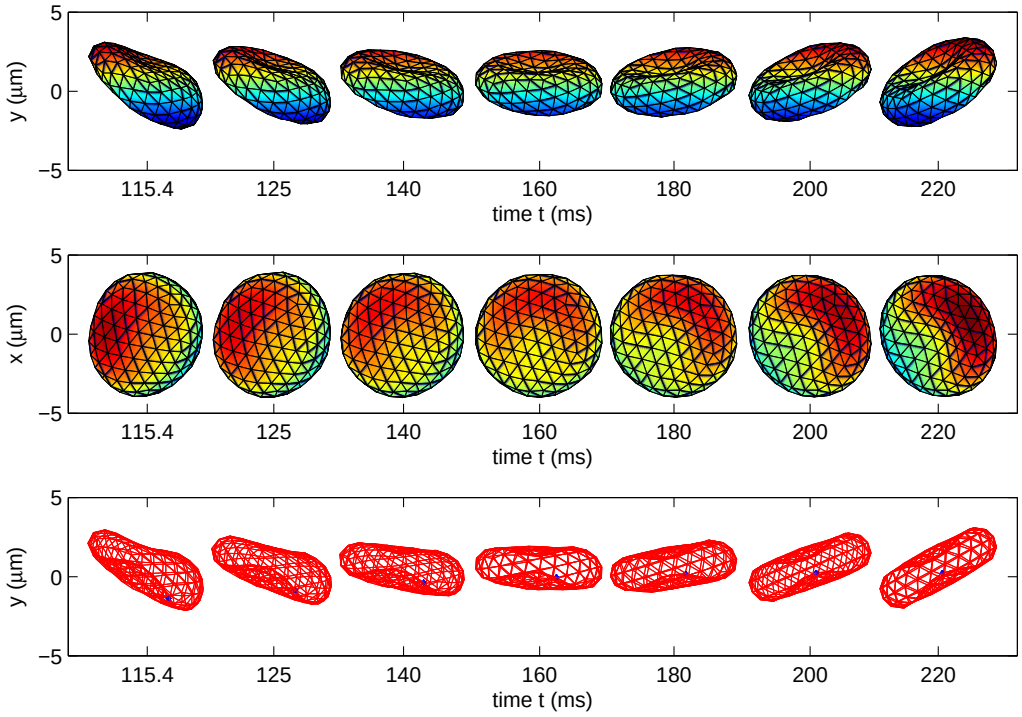

Figure 4.26: Shapes of the cell in different locations in the channel: (top), side view, observe from (10,0,0); (middle), top view, observe from (0,10,0); (bottom), view from the side of RBC such that longitude is presented in figure. All the three figures plots the same cell at same times, which are t = 115.4ms, 125ms, 140ms, 160ms, 180ms,200ms, 220ms, respectively. Here $\alpha = 0.3$.

observation is that, when the cell changes towards the biconcave shape, the marked membrane particle almost did not tank–tread, and after the cell obtains a biconcave shape (at

first the biconcave shape has one side deeper than the other), the cell membrane starts to tank–tread dimple back to dimple. Another observation is that during the process of the cell getting back to its nonuniform natural state (similar to the go-and-stop experiments), it keeps rotating as in Figure 4.26. This behavior was observed in experiments done in [6].

4.6 Conclusions

In this Chapter, we have proposed a modified RBC model with effect of shape memory to simulate cell dynamics in both shear flow and Poiseuille flow. Similar to the 2D case, we have first considered the cell model with uniform natural state, and obtain the cell's biconcave disk shape by shrinking the cell volume from a whole sphere into a volume about 64% of the original ball volume. After obtaining the initial shape, we have used it as the shape which the cell memorizes (the nonuniform natural state). Using the cell energy to store the cell shape has an advantage since the rest shape is always the reference shape for all choices of α.

With this model, we have done the validations with the published works in literature as follows: (i) we have performed the stretching test on the cell with uniform natural state and compared the cell length and width with the experimental results; (ii) we have suspended the cell with uniform natural state into shear flow with high shear rates, and compared the results with numerical simulation results in literature; (iii) we have carried the go-and-stop experiments for cells with both uniform and nonuniform natural states and obtained that with nonuniform natural states, the cell does have the dimple back to dimple behavior after outside force is removed.

When the cell with uniform natural state is suspended into shear flow with very low

shear rates, it performs tumbling motion, instead of tank–treading. The transitions of the cell with a coarser grained level and those with finer levels have been studied. The transition occurs at lower shear rate when using finer membrane mesh. The threshold is approaching to the value suggested by the experimental results.

When the cell with uniform natural state is suspended into Poiseuille flow, with periodic boundary condition only in the flow direction, the cell shape changes to an equilibrium shape, which depends on the channel height, the flow velocity, and the shape memory coefficient α. It is found that only with nonzero α value, cell can change to a slippery shape at very low flow rate. When the flow rate is higher, the cell has a parachute shape or 2D parachute shape, depending on the height of the channel. If the channel height from top to bottom is the same as the channel width from front to back, the cell equilibrium shape is parachute shape, if such symmetric domain does not exist, the cell will change to a 2D parachute shape.

It is reported that, in the experiments, a RBC going through a micro-channel with blockage will first rapidly change to a cup shape, and then recover the biconcave shape with cell orientation rotated, our simulations do suggest such behavior if the cell adopts nonuniform natural state, i.e., the cell has the shape memory property.

Bibliography

[1] M. Abkarian, M. Faivre and A. Viallat, Swinging of red blood cells under shear flow, *Phys. Rev. Lett.* **98**, 188302 (2007).

[2] J. Adams, P. Swarztrauber and R. Sweet, FISHPAK: A package of Fortran subprograms for the solution of separable elliptic partial differential equations, The National Center for Atmospheric Research, Boulder, CO, 1980.

[3] D. Barthes-Biesel, A. Diaz, and E. Dhenin, Effect of constitutive laws for two-dimensional membranes on flow-induced capsule deformation, *J. Fluid. Mech.* **460**, 211 (2002).

[4] J. Beaucourt, F. Rioual, T. Seń, T. Biben, and C. Misbah, Steady to unsteady dynamics of a vesicle in a flow, *Phys. Rev. E* **69**, 011906 (2004).

[5] M. Bercovier, O. Pironneau, Error estimates for finite element method solution of the Stokes problem in the primitive variables, *Numer. Math.* **33**, 211 (1979).

[6] S. Braunmuller, L. Schmid, E. Sackmann, and T. Franke Hydrodynamic deformation reveals two coupled modes/time scales of red blood cell relaxation, *Soft Matter* **8**, 11240 (2012).

[7] M. O. Bristeau, R. Glowinski, J. Periaux, Numerical methods for the Navier-Stokes equations. Applications to the simulation of compressible and incompressible viscous flow, *Computer Physics Reports* **6**, 73 (1987).

[8] S.-D. Chen, T.-W. Pan, C.-C. Chang, The motion of a single and multiple neutrally buoyant elliptical cylinders in plane Poiseuille flow, *Phys. Fluids* **24**, 103302 (2012).

[9] A. J. Chorin, A numerical method for solving incompressible viscous flow problems, *J. Comput. Phys.* **2**, 12 (1967).

[10] A. J. Chorin, Numerical solution of the Navier-Stokes equations, *Math. Comput.* **23**, 341 (1968).

[11] A. J. Chorin , T. J. R. Hughes, M. F. McCracken , J. E. Marsden, Product formulas and numerical algorithms, *Comm. Pure Appl. Math* **31**, 205 (1978).

[12] P. G. Ciarlet, *The Finite Element Method for Elliptic Problems*, North-Holland, Amsterdam, 1978.

[13] P. G. Ciarlet, Basic error estimates for elliptic problems. *Handbook of Numerical Analysis*, Vol. II, Ciarlet PG and Lions JL (Eds.), North-Holland, Amsterdam, 17 (1991).

[14] E. J. Dean , R. Glowinski, A wave equation approach to the numerical solution of the Navier-Stokes equations for incompressible viscous flow, *C.R. Acad. Sci. Paris*, Série I, **325**, 783 (1997).

[15] E. Ding, C.K. Aidun, The dynamics and scaling law for particles suspended in shear flow with inertia, *J. Fluid Mech* **423**. 317 (2000).

[16] S. K. Doddi and P. Bagchi, Lateral migration of a capsule in a plane Poiseuille flow in a channel, *International Journal of Multiphase Flow* **34**, 966 (2008).

[17] J. Dupire, M. Socol, and A. Viallat, Full dynamics of a red blood cell in shear flow, *Proc. Natl. Acad. Sci. U.S.A.*, **109**, 20808 (2012).

[18] C. D. Eggleton, and A. S. Popel, Large deformation of red blood cell ghosts in a simple shear flow, *Phys. Fluids* **10**, 1834 (1998).

[19] E. Evans and Y.-C. Fung, Improved measurements of the erythrocyte geometry, *Microvascular Research* **4**, 335-347 (1972).

[20] D.A. Fedosov, B. Caswell, and G. E. Karniadakis, A multiscale red blood cell model with accurate mechanics, rheology, and dynamics, *Biophys J.* **98**, 2215 (2010).

[21] T. M. Fischer, M. Stöhr-Liesen, and H. Schmid-Schönbein, The red cell as a fluid droplet: tank tread-like motion of the human erythrocyte membrane in shear flow, *Science* **202**, 894 (1978).

[22] T. M. Fischer, Shape Memory of Human Red Blood Cells, *Biophys. J*, **86**, 3304 (2004).

[23] R. Glowinski , O. Pironneau , Finite element methods for Navier-Stokes equations, *Annu. Rev. Fluid Mech.* **24**, 167 (1992).

[24] R. Glowinski, T.W. Pan, T. Hesla, D.D. Joseph, and J. Periaux, A fictitious domain approach to the direct numerical simulation of incompressible viscous flow past moving rigid bodies: Application to particulate flow, *J. Comput. Phys.* **169**, 363 (2001).

[25] R. Glowinski , Finite element methods for incompressible viscous flow, *Handbook of Numerical Analysis*, Vol. IX, Ciarlet PG and Lions JL (Eds.), North-Holland, Amsterdam, 3 (2003).

[26] http://www.protocol-online.org/forums/blog/42/entry-46-phase-1-cell-membrane/

[27] V. Kantsler and V. Steinberg, Orientation and dynamics of a vesicle in tank–treading motion in shear flow, *Phys. Rev. Lett.* **95**, 258101 (2005).

[28] V. Kantsler and V. Steinberg, Transition to tumbling and two regimes of tumbling motion of a vesicle in shear flow, *Phys. Rev. Lett.* **96**, 036001 (2006).

[29] B. Kaoui, J. Harting, and C. Misbah, Two-dimensional vesicle dynamics under shear flow: Effect of confinement, *Phys. Rev. E*, **83**, 066319 (2011).

[30] S. R. Keller and R. Skalak, Motion of a tank–treading ellipsoidal particle in a shear flow, *J. Fluid Mech.* **120**, 27 (1982).

[31] H. B. Li, H. H. Yi, X. M. Shan, and H. P. Fang, Shape changes and motion of a vesicle in a fluid using a lattice Boltzmann model, *Europhysics Letters*, **81**, 54002 (2008).

[32] W. K. Liu, Y. Liu, D. Farrell, L. Zhang, X. S. Wang, Y. Fukui, N. Patankar, Y. Zhang, C. Bajaj, J. Lee, J. Hong, X. Chen, and H. Hsu, Immersed finite element method and its applications to biological systems, *Comput. Methods Appl. Mech. Engrg.* **195**, 1722 (2006).

[33] G. I. Marchuk , Splitting and alternate direction methods, *Handbook of Numerical Analysis*, Vol. I, Ciarlet PG and Lions JL (Eds.), North-Holland, Amsterdam, 197 (1990).

[34] M. Marion , R. Temam, Navier-Stokes Equations, *Handbook of Numerical Analysis*, Vol. VI, Ciarlet PG and Lions JL (Eds.), North-Holland, Amsterdam, 503 (1998).

[35] J. L. McWhirter, H. Noguchi, and G. Gompper, Deformation and clustering of red blood cells in microcapillary flows, *Soft Matter* **7**, 10967 (2011).

[36] J. P. Mills, L. Qie, M. Dao, C. T. Lim, S. Suresh, Nonlinear elastic and viscoelastic deformation of the human red blood cell with optical tweezers, *Mech. Chem. Biosyst.* **1(3)**, 169 (2005).

[37] C. Misbah, Vacillating breathing and tumbling of vesicles under shear flow, *Phys. Rev. Lett.* **96**, 028104 (2006).

[38] C. Misbah, Vesicles, capsules and red blood cells under flow, *J. Phys. Conf. Ser.*, **392**, 012005 (2012).

[39] myVMC, http://www.myvmc.com/anatomy/blood-function-and-composition/

[40] H. Noguchi and G. Gompper, Fluid vesicles with viscous membranes in shear flow, *Phys. Rev. Lett.* **93**, 258102 (2004).

[41] H. Noguchi and G. Gompper, Dynamics of fluid vesicles in shear flow: Effect of membrane viscosity and thermal fluctuation, *Phys. Rev. E* **72**, 011901 (2005).

[42] H. Noguchi and G. Gompper, Swinging and tumbling of fluid vesicles in shear flow, *Phys. Rev. Lett.* **98**, 128103 (2007).

[43] T.W. Pan, D.D. Joseph, R. Bai, R. Glowinski, and V. Sarin, Fluidization of 1204 spheres: simulation and experiments, *J. Fluid. Mech.* **451**, 69 (2002).

[44] T. W. Pan , R. Glowinski, Direct simulation of the motion of neutrally buoyant balls in a three-dimensional Poiseuille flow, *C. R. Mecanique* **333**, 884 (2005).

[45] T. W. Pan, and T. Wang, Dynamical simulation of red blood cell rheology in microvessels, *International Journal of Numerical Analysis and Modeling*, **6**, 455 (2009).

[46] Z. Peng, and Q. Zhu, Deformation of the erythrocyte cytoskeleton in tank treading motions, *Soft Matter* **9**, 7617 (2013).

[47] C. S. Peskin, Numerical analysis of blood flow in the heart, *J. Comput. Phys.* **25**, 220 (1977).

[48] C. S. Peskin and D. M. McQueen, Modeling prosthetic heart valves for numerical analysis of blood flow in the heart, *J. Comput. Phys.* **37**, 11332 (1980).

[49] C. S. Peskin, The immersed boundary method, *Acta Numer.* **11**, 479 (2002).

[50] O. Pironneau , *Finite Element Methods for Fluids*, J. Wiley, Chichester, 1989.

[51] C. Pozrikidis, Effect of membrane bending stiffness on the deformation of capsules in simple shear flow, *J. Fluid. Mech.* **440**, 269 (2001).

[52] C. Pozrikidis, Numerical simulation of the flow-induced deformation of red blood cells, *Ann. Biomed. Eng.* **31**, 1194 (2003).

[53] L. Shi, T. W. Pan and R. Glowinski, Numerical simulation of lateral migration of red blood cells in Poiseuille flows, *Int. J. Numer. Methods Fluids* **68**, 1393 (2012).

[54] L. Shi, T. W. Pan, R. Glowinski, Deformation of a single blood cell in bounded Poiseuille flows, *Phys. Rev. E* **85**, 016307 (2012).

[55] L. Shi, T. W. Pan, R. Glowinski, Lateral migration and equilibrium shape and position of a single red blood cell in bounded Poiseuille flows, *Phys. Rev. E* **86**, 056308 (2012).

[56] L. Shi, T. W. Pan, R. Glowinski, Three-dimensional numerical simulation of red blood cell motion in Poiseuille flows, *Int. J. Numer. Meth. Fluids* **76**, 397 (2014).

[57] J.M. Skotheim and T.W. Secomb, Red blood cells and other nonspherical capsules in shear flow: oscillatory dynamics and the tank–treading-to-tumbling transition, *Phys. Rev. Lett.* **98**, 078301 (2007).

[58] Y. Sui, Y. T. Chew, P. Roy, Y. P. Cheng, and H. T. Low, Dynamic motion of red blood cells in simple shear flow, *Phys. Fluids* **20**, 112106 (2008).

[59] G. Tomaiuolo, L. Lanotte, G. Ghigliotti, C. Misbah, and S. Guido, Red blood cell clustering in Poiseuille microcapillary flow, *Phys. Fluids* **24**, 051903 (2012).

[60] K. Tsubota and S. Wada, Effect of the natural state of an elastic cellular membrane on tank-treading and tumbling motions of a single red blood cell, *Phys. Rev. E* **81**, 011910 (2010).

[61] K. Tsubota and S. Wada, Elastic force of red blood cell membrane during tank-treading motion: Consideration of the membrane's natural state, *Int. J. of Mech. Sci.* **52**, 356 (2010).

[62] K. Tsubota, S. Wada, and H. Liu, Elastic behavior of a red blood cell with the membranes nonuniform natural state: equilibrium shape, motion transition under shear flow, and elongation during tank–treading motion, *Biomech. Model Mechanobiol.* **13** 735 (2014).

[63] S. Turek , A comparative study of time-stepping techniques for the incompressible Navier-Stokes equations: from fully implicit non-linear schemes to semi-implicit projection methods, *Int. J. Num. Math. in Fluids* **22**, 987 (1996).

[64] S. K. Veerapaneni, Y.-N. Young, P. M. Vlahovska, and J. Blawzdziewicz, Dynamics of a compound vesicle in shear flow, *Phys. Rev. Lett.* **106**, 158103 (2011).

[65] T. Wu and J. Feng, Simulation of malaria-infected red blood cells in microfluidic channels: Passage and blockage, *Biomicrofluidics* **7**, 044115 (2013).

[66] P. M. Vlahovska, T.-N. Young , G. Danker and C. Misbah, Dynamics of a non-spherical microcapsule with incompressible interface in shear flow, *J. Fluid Mech.* **678**, 221 (2011).